Direct Particle-Fluid Simulations of Isothermal and Non-isothermal Turbulent Flows

Direkte Partikel-Fluid-Simulationen von isothermen und nicht-isothermen turbulenten Strömungen

Von der Fakultät für Maschinenwesen der Rheinisch-Westfälischen Technischen Hochschule Aachen zur Erlangung des akademischen Grades eines Doktors der Ingenieurwissenschaften genehmigte Dissertation

> vorgelegt von Thede Peter Kiwitt

Berichter: Univ.-Prof. Dr.-Ing. Wolfgang Schröder

Univ.-Prof. Dr.-Ing. Reinhold Kneer

Tag der mündlichen Prüfung: 07. Oktober 2025

Diese Dissertation ist auf den Internetseiten der Universitätsbibliothek online verfügbar.

Abstract

The interaction of particles with the carrier fluid in multiphase flow is of fundamental importance in various applications. This includes, for example, natural phenomena such as volcanic eruptions or technical systems such as industrial combustion plants. In the latter context, the particles serve as energy carriers releasing their chemically stored energy during the combustion process for further usage. Due to the negative environmental impact of fossil fuels, intensive efforts are being made to switch to sustainable alternatives such as biomass. In contrast to coal particles, which are predominantly spherical, biomass particles often have elliptical shapes. This anisotropic geometry leads to different aerodynamic interactions which influence the combustion process.

Despite the high level of detail of fully-resolved simulations, comprehensive studies regarding non-spherical particles are rare in the scientific literature. The complex dynamics and high computational costs pose significant computational challenges such that reduced models are often used in their place. The present work aims to fill this gap by investigating fully-resolved numerical simulations of particle-laden flows within pipe and free jet flow with non-spherical particles. The turbulence dynamics, the interaction between the particles and the flow field, and the influence of the particle properties on the flow geometry are investigated. The numerical analysis uses a finite volume method with a level-set/cut-cell method to ensure that all geometries are fully resolved and that mass, momentum, and energy are conserved. This allows precise quantification of the surface forces acting on the particles and their interaction with the surrounding fluid. In this work, spherical and ellipsoidal particles are investigated under turbulent flow conditions.

In addition, the temperature differences between particles in the aspect ratio range $1 \leq \beta \leq 8$ and the carrier fluid are analyzed in the context of combustion systems. A correlation equation for the calculation of the Nusselt number is presented. Subsequently, an efficient conjugate heat transfer model is presented which captures the thermodynamic processes within solid bodies. This model considers the thermal processes within particles as well as the local temperature gradients at the surfaces of the particles. Finally, the new methodology is used to evaluate the accuracy of Lagrange point-particle models which are often used to simulate complex particle-laden systems.

Zusammenfassung

Die Wechselwirkung zwischen Partikeln und dem Trägerfluid in Mehrphasenströmungen ist in verschiedenen Anwendungsfällen von elementarer Bedeutung. Dies umfasst beispielsweise natürliche Phänomene wie Vulkanausbrüche oder auch technische Systeme wie industrielle Verbrennungsanlagen. Im letzteren Kontext fungieren die Partikel als Energieträger die ihre gespeicherte Energie während des Verbrennungsprozesses zur weiteren Nutzung freisetzen. Angesichts des negativen Umwelteinflusses fossiler Brennstoffe wird intensiv daran gearbeitet, auf nachhaltige Alternativen wie Biomasse umzusteigen. Im Gegensatz zu Kohlepartikeln, die überwiegend sphärisch sind, weisen Biomassepartikel häufig elliptische Formen auf. Diese anisotropische Geometrie führt zu unterschiedlichen aerodynamischen Wechselwirkungen, die den Verbrennungsprozess beeinflussen.

Trotz der hohen Relevanz vollständig aufgelöster Simulationen sind umfassende Studien im Hinblick auf nicht-spärische Partikel in der wissenschaftlichen Literatur selten. Die komplexen Dynamiken und die hohen rechnerischen Ressourcen stellen signifikante Herausforderungen bei der Berechnung dar, sodass häufig Ersatzmodelle mit reduzierter Genauigkeit verwendet werden. Die vorliegende Arbeit zielt darauf ab, diese Lücke zu schließen, indem vollständig aufgelöste Simulationen elliptischer partikelbeladener Strömungen innerhalb einer Rohrströmung und einem Freistrahl untersucht werden. Es werden die Turbulenzdynamiken, die Wechselwirkungen zwischen Partikeln und Strömung, sowie der Einfluss der Partikeleigenschaften auf die Strömungsgeometrie untersucht.

Die numerische Analyse verwendet ein Finite-Volumen-Verfahren mit einer Level-Set/Cut-Cell-Methode, um sicherzustellen, dass alle Geometrien vollständig aufgelöst sind und der Erhalt von Masse, Impuls, und Energie gewährleistet ist. Dies ermöglicht die präzise Quantifizierung der Oberflächenkräfte, die auf die Partikel wirken, sowie deren Wechselwirkungen mit dem umgebenden Fluid. Sowohl sphärische als auch ellipsoide Partikel werden unter turbulenten Strömungsbedingungen untersucht.

Darüber hinaus werden im Kontext von Verbrennungssystemen die Temperaturunterschiede zwischen nicht-spärischen Partikeln im Seitenverhältnis $1 \le \beta \le 8$ und dem Trägerfluid analysiert. Eine Korrelationsgleichung zur Berechnung der Nusselt-Zahl wird vorgestellt. Anschließend wird ein effizientes Modell der konjugierten Wärmeübertragung präsentiert, welches die thermodynamischen Vorgänge innerhalb der Partikel erfasst. Dieses Modell berücksichtigt nicht nur das thermische Verhalten innerhalb fester Körper, sondern auch lokale Temperaturgradienten an den Oberflächen der Partikel.

Abschließend wird die neue Methodik zur Bewertung der Genauigkeit von Lagrange-Punkt-Partikelmodellen verwendet welche häufig zur Simulation komplexer Partikelbeladener Systeme eingesetzt werden.

Contents

	Abs	tract .		iii
	Zusa	ammenf	fassung	V
	Non	nenclati	re	χV
1	Intro	oductio	n	1
2	Mat	hematio	cal model	5
	2.1	Fluid	phase	5
	2.2		phase	6
	2.3		phase energy exchange	9
	2.4		solid interface line	11
3	Nun	nerical r	method	13
	3.1	Cartes	sian grid	13
		3.1.1	Domain decomposition	15
		3.1.2	Adaptive mesh refinement	17
		3.1.3	Dynamic load balancing	18
	3.2	Paralle	el particle tracking	19
		3.2.1	Parallelization	20
		3.2.2	Temporal integration of the particle dynamics	21
		3.2.3	Collision model	22
	3.3	Finite	volume solver	24
		3.3.1	Spatial discretization	24
		3.3.2	Temporal integration	26
		3.3.3	Immersed-boundary method	27
	3.4	Entha	lpy solver	32
	3.5	Coupl	ing	33
		3.5.1	Coupling mechanism	33
		3.5.2	Solver coupling	34
		3.5.3	Slicing technique	36
	3.6	Applie	cation of boundary conditions	38
4	Solv	er valid	ation	43
	4.1	Turbu	llent pipe-free jet flow	43
		4.1.1	Turbulent pipe flow	43
		4.1.2	Turbulent free jet flow	44
		419	Complexity	10

	4.2	Const	ant surface temperature	46
		4.2.1	Grid convergence study	46
		4.2.2	Numerical validation	47
		4.2.3	Conclusions	49
	4.3	Conju	gate heat transfer	50
		4.3.1	Grid convergence study	50
		4.3.2	Validation of the coupling formulation	51
		4.3.3	Energy conservation	57
		4.3.4	CHT for moving bodies	58
		4.3.5	Freely falling bodies	62
		4.3.6	Parallel performance on HPC systems	63
		4.3.7	Conclusions	65
5	Part	icle-lad	en free jet flow	67
	5.1	Curre	nt research	68
	5.2	Doma	in of integration	69
	5.3	Flow	and particle parameters	70
	5.4	Partic	cle-laden turbulent pipe flow	71
		5.4.1	Particle distribution	71
		5.4.2	Linear velocity statistics	73
		5.4.3	Rotational statistics	75
		5.4.4	Multiphase energy exchange	76
	5.5	Partic	ele-laden turbulent free jet flow	78
		5.5.1	Particle statistics	79
		5.5.2	Jet structure	82
		5.5.3	Fluid kinetic energy	83
		5.5.4	Fluid turbulence intensity	84
	5.6	Concl	usions	84
6			fer dynamics	87
	6.1		lation equation for the Nusselt number of ellipsoidal particles $% \left(1\right) =\left(1\right) \left($	87
		6.1.1	Current research	89
		6.1.2	Computational setup	90
		6.1.3	Fluid dynamics	91
		6.1.4	Flow and temperature field	92
		6.1.5	Correlation equation	98
		6.1.6	Conclusions	109
	6.2		e accuracy of Lagrangian point-particle models	110
		6.2.1	Description of interphase dynamics	110
		6.2.2	Application of boundary conditions	111
		6.2.3	Computational setup	112
		6.2.4	Results and discussion	113
		6.2.5	Conclusions	119
7	Con	clusions	s and Outlook	121

	Contents
References	125
A Appendix	135

Nomenclature

All variables presented in this nomenclature are expressed in non-dimensional form unless stated otherwise. The procedure and reference quantities employed for the non-dimensionalization are detailed in the Appendix.

Latin symbols

a Vector of acceleration

A Surface areaa Speed of sound

 $a,\ b,\ c$ Ellipsoidal semi-axes

 ${\cal C}$ Reconstruction constants

 c_p Heat capacity D Pipe diameter d Diameter

 d_{eq} Volume-equivalent diameter

E Total Energy

e Specific internal energy

 E_k Kinetic Energy e_i Unit vector F Flux vector

 \boldsymbol{F} Force

 $egin{array}{ll} g & & \operatorname{Gravity\ vector} \ R & & \operatorname{Rotation\ matrix} \ H & & \operatorname{Flux\ tensor} \ \end{array}$

h Specific enthalpy, convective heat transfer coefficient

h Width of Cartesian cell k Thermal conductivity

m Mass

 N_n Number of reconstruction neighbors

P	Primitive variables
p	Pressure
PDF	Probability density function
Q	Conservative variables
q	Specific heat flux
Q	Total heat flux
R	Orthogonal matrix, rotation matrix
$\mathcal R$	Residual operator
r	Radius
R	Ideal gas constant
SD	Standard deviation
sf	Cartesian surface
S_{λ}	Sutherland constant heat conductivity
S_{μ}	Sutherland constant viscosity
\mathcal{T}	Torque
T	Temperature
t	Time
ts	Time step
\boldsymbol{u}	Velocity vector
u, v, w	Velocity in Cartesian $x,y,{\rm and}z{\rm -direction}$
V	Volume
\underline{W}	Diagonal weight matrix
$oldsymbol{x}$	Coordinate vector
x, y, z	Cartesian directions
x_i	Cartesian direction
Greek symbo	
α	Runge-Kutta coefficients, step size
β	Particle aspect ratio
ϕ	Angle [°]
2 /	I I married as afficient

β	Particle aspect ratio
ϕ	Angle $[^{\circ}]$
χ	Upwind coefficient
Γ	Surface of embedded bodies
γ	Ratio of specific heats
ϵ	Vector of quaternions
ϵ	Rate of particle-induced fluid dissipation
ϵ_i	Quaternion

ζ	Volume loading
μ	Dynamic viscosit

 ψ Rate of kinetic energy transferred

 $\begin{array}{lll} \Psi & & \text{Level-set} \\ \rho & & \text{Density} \\ \tau & & \text{Time shift} \\ \underline{\tau} & & \text{Stress tensor} \\ \Delta t & & \text{Time step size} \\ \Delta x & & \text{Mesh spacing} \\ \omega & & \text{Angular velocity} \\ \tau & & \text{Relaxation time} \end{array}$

Dimensionless numbers

Fo	Fourier number
Ma	Mach number
Nu	Nusselt number
Pr	Prandtl number
Re	Reynolds number
St	Stokes number

Subscripts

$(\cdot)_0$	State of rest			
$(\cdot)_{abs}$	Absolute value			
$(\cdot)_{\mathrm{avg}}$	Averaged value			

 $(\cdot)_{\mathrm{body}}$ Value of embedded body

 $\begin{array}{lll} (\cdot)_p & & \text{Particle } p \\ (\cdot)_C & & \text{In cell center} \\ (\cdot)_{cl} & & \text{Centerline} \\ (\cdot)_f & & \text{Fluid domain} \\ (\cdot)_G & & \text{Ghost cell} \\ (\cdot)_I & & \text{Image variable} \\ (\cdot)_{\infty} & & \text{Freestream value} \end{array}$

 $\begin{array}{ll} (\cdot)_{\max} & & \text{Maximum} \\ (\cdot)_{\min} & & \text{Minimum} \end{array}$

 $(\cdot)_{n_i}$ i-th neighbor cell $(\cdot)_{ref}$ Reference value

$(\cdot)_s$	Solid domain		
$(\cdot)_{\Gamma}$	At cell surface		
$(\cdot)_{\mathrm{sub}}$	Sub step		
$(\cdot)_{ au}$	Friction value		
(.)	Matrix		

Superscripts

 $\partial \qquad \qquad \text{Partial differential operator}$

 $\tilde{(\cdot)}$ Dimensional variable

 $\begin{array}{ll} (\cdot)^{inv} & \quad \text{Inviscid} \\ (\cdot)^{L} & \quad \text{Left} \end{array}$

(*) Time average ∇ Nabla operator $(\cdot)^+$ Pseudo-inverse $(\cdot)'$ Fluctuation $(\cdot)^R$ Right $(\cdot)^{vis}$ Viscous

(•) Particle-aligned reference frame

Abbreviations

AIA Aerodynamisches Institut Aachen

 $\begin{array}{ll} {\rm AME} & {\rm Adaptive \ mesh \ extension} \\ {\rm AMR} & {\rm Adaptive \ mesh \ refinement} \end{array}$

AUSM Advection upstream splitting method CFD Computational Fluid Dynamics

CFL Courant-Friedrichs-Lewy
CHT Conjugate heat transfer
DLB Dynamic Load Balancing
DNS Direct Numerical Simulation
DPFS Direct Particle-Fluid Simulation

FV Finite Volume

FVMB Finite Volume for Moving Boundaries

HPC High Performance Computing IBM Immersed-Boundary Method

LES Large-eddy simulation

 ${\bf MILES} \qquad \qquad {\bf Monotone~integrated~large-eddy~simulation}$

MPI Message Passing Interface

MUSCL Monotone upstream-centered scheme for conservation laws

RK Runge-Kutta

RMS Root-mean-square

RWTH Rheinisch-Westfälische Technische Hochschule Aachen

1 Introduction

In the context of daily live, particle-laden flows are encountered in numerous situations. Volcanic eruptions, sandblasting, and particle-laden flows in industrial combustion plants are only a few examples. In the latter, the particles function as energy carriers releasing their stored energy during the combustion process and thereby facilitate the conversion to usable energy, heat, or locomotion.

As of today, coal is the most used raw material for energy conversion [92]. Being used for centuries, coal has been a key driver of industrialization. However, this comes at great disadvantage. Approximately one-third of all global CO_2 emissions can be attributed to the energy processes derived from coal [92]. The growing demand for environmentally friendly and sustainable energy conversion necessitates the substitution of fossil fuels with alternative energy sources.

Biomass, which consists of wood chips, tree bark, or wheat, among many others, is a raw material that is largely independent of geographical conditions due to its broad availability. The utilization of this raw material is predominantly climate-neutral as only the previously bound CO_2 is released [34, 54]. Hence, biomass has emerged as an environmentally friendly alternative to coal in recent years. Another significant advantage of using biomass for industrial energy processes is the manner in which it is stored. Similar to coal, biomass is utilized in particle form. Consequently, this renewable raw material is effectively a drop-in replacement for particle-based fossil fuels such as coal in industrial combustion plants.

However, biomass is a natural product and as such, its particles retain a fibrous structure. Despite pre-processing, the particle shape can be described as ellipsoidal rather than spherical [34]. Consequently, biomass particles possess significantly different aerodynamic properties compared to spherical particles. These particles have orientation-dependent dynamics due to their anisotropic shape inducing additional rotational forces. While the behavior of spherical particles in freestream conditions and in the context of combustion engines is well understood [7, 24, 75, 119], the available literature shows that there are hardly an detailed results on non-spherical particles.

In the combustion of fine-scale fuels in industrial combustion plants, solid coal or biomass particles are blown into a combustion chamber where they burn off with the addition of air. Part of the combustion air is blown in together with the fuel in the primary flow which forms a turbulent, two-phase free jet when it enters the combustion chamber. The jet flow determines the flame geometry because the mixing behavior of air and fuel affects the dwell times of dust particles in the combustion chamber, their heating rates, the chemical reactions on their surfaces and thus, the overall combustion process. These configurations often involve high Reynolds number environments and are associated with substantial turbulence. The presence of particles, irrespective of their shape, exerts a modulation on the behavior of the carrier flow [75]. As demonstrated by Einstein, the viscosity of the fluid is subject to alteration by the particles [22]. Additionally, the particle motion is not only governed by the fluid motion, but also by the particle inertia, thereby increasing the complexity of the multiphase interactions even further [66, 67]. Due to the relative movement between the particles and the fluid, the different phases continuously exchange kinetic energy, impact the turbulent structures, and modulate the dissipation rate of the fluid [100]. This leads to an imbalance in the distribution of kinetic energy in the individual scales and a reorganization of the energy cascade [97, 100]. For example, research has shown that the turbulence intensity of the carrier fluid can either be increased or decreased by the presence of spherical particles depending on various parameters [31, 83, 102, 109, 111]. To this day, very little investigation has been conducted on the impact of ellipsoidal particles.

In the context of industrial combustion plants, the influence of particles in carrier flows extends to the domain of the thermal dynamics. The exchange of thermal energy occurs via radiation, conduction, and convection [72, 96, 106]. Given the pivotal role of temperature on the properties of the fluid, it is imperative to undertake a thorough examination of this parameter. It is therefore paramount to include the temperature as an explicit parameter in the investigation of fully-resolved particles.

The anisotropic particle shape results in different particle behavior in comparison to spherical particles [34]. Therefore, models employed to simulate particle-laden flows must account for the anisotropic particle shape. Fully-resolved simulations are computationally expensive and thus, investigations are frequently based on Lagrangian point-particle models [7]. These models include significant simplifications to reduce the computational complexity and thus, the overall load [25]. Therefore, such models can only be approximations of the actual behavior. The simplifications often include, among others, that the particle shape is spherical. Although steps have been taken to further develop models for point-particle models, these investigations are still incomplete [26].

In this thesis, simulations of fully-resolved particles of spherical and ellipsoidal shape in isothermal and non-isothermal flow conditions are conducted to further advance these investigations. To this end, a series of modifications to the in-house simulation framework m-AIA are made and novel models are introduced. The results are documented in [58–60] upon which this thesis is based on.

In Kiwitt et al. [59], the interaction of spherical and ellipsoidal particles in turbulent pipe-jet flow in isothermal conditions is investigated. Preferential particle statistics inside the pipe are analyzed and the subsequent impact on free jet flow is discussed. Results of the kinetic energy budget of the multiphase configuration are shown and the impact on the jet geometry is discussed. The varying effect of the different particle aspect ratios on the fluid is highlighted and discussed.

Subsequently, the focal point of the investigations changes from isothermal to non-isothermal, i.e., the impact of temperature gradients is considered.

Kiwitt et al. [58] presents a novel correlation equation for the prediction of the Nusselt number of ellipsoidal particles in uniform flow in non-isothermal setups.

More than 6 600 fully-resolved simulations are computed to cover a wide range of Reynolds numbers Re, particle angles ϕ , particle aspect ratios β , and temperature ratios T_R between the particle and the fluid. The resulting flow and temperature fields are analyzed and used to derive a correlation equation for use in Lagrangian point-particle models, thereby enhancing the accuracy of these models.

In Kiwitt et al. [60], an efficient method for the computation of heat exchanges between a carrier fluid and the embedded moving bodies is derived. The conjugate heat transfer (CHT) method utilizes an iterative algorithm to minimize the differences of the heat fluxes at the interface line, thereby guaranteeing accurate results and ensuring an energy-conserving method. Several test problems are shown to provide a thorough validation of the method for static, shape-transforming, and moving bodies of complex arbitrary geometries. Benchmark results show the high performance in parallel computing systems. The method is used to discuss the accuracy of the heat transfer dynamics in Lagrangian point-particle models.

The thesis is organized as follows. Ch. 2 presents the mathematical models used for description of the fluid and particle dynamics. The governing equations of the fluid and solid phases are highlighted and the quantification of the interphase energy exchange is outlined. Ch. 3 presents the numerical methods. The finite volume method and the cut-cell method are outlined and modifications and enhancements necessary for the computation of the aforementioned problems are described. The chapter finishes by presenting the parallelization and coupling strategies. In Ch. 4 the numerical setup is validated for the different configurations involving particle-laden pipe and free jet flow, as well as non-isothermal setups. Ch. 5 shows the results for the investigation of the isothermal particle-laden pipe-jet flow. The pipe and the free jet domain are discussed separately and the particle distribution inside the pipe is related to the free jet fluid flow. Ch. 6 discusses non-isothermal setups. A novel correlation equation for the Nusselt number is presented and an efficient approach to conjugate heat transfer investigates the accuracy of assumptions commonly made in Lagrangian point-particle models. The results of the numerical investigations are summarized in Ch. 7 where conclusions are drawn and an outlook for further research objectives is presented.

2 Mathematical model

The mathematical formulations governing the fluid and the solid phases are presented, and the formulations used to describe the particle motions are outlined. The equations to compute the energy transfer between the different phases are described and the methodology of the fluid-solid interface is highlighted.

2.1 Fluid phase

The flow of a viscous, compressible fluid is determined by the conservation of mass, momentum, and energy in a control volume V(t) with surface A(t) in non-dimensional form by

$$\frac{d}{dt} \int_{V(t)} \mathbf{Q} dV + \oint_{\partial V(t)} \left(\underline{\mathbf{H}}^{inv} - \underline{\mathbf{H}}^{vis} \right) \cdot \mathbf{n} dA = \mathbf{0}$$
 (2.1)

with $\mathbf{Q} = [\rho, \rho \mathbf{u}, \rho E]^T$ being the vector of conservative variables and \mathbf{n} being the outwards-facing normal vector. The conservative variables \mathbf{Q} are the density ρ , the velocity vector \mathbf{u} , and the total energy $\rho E = \rho e + \frac{1}{2}\rho \mathbf{u}^2$ with the specific internal energy e.

The flux tensors $\underline{\mathbf{H}}^{inv}$ and $\underline{\mathbf{H}}^{vis}$ denote the inviscid and viscous flux tensors and are given by

$$\underline{\mathbf{H}}^{inv} - \underline{\mathbf{H}}^{vis} = \begin{pmatrix} \rho(\mathbf{u} - \mathbf{u}_{\partial V}) \\ \rho\mathbf{u}(\mathbf{u} - \mathbf{u}_{\partial V}) + p\underline{\mathbf{I}} \\ \rho E(\mathbf{u} - \mathbf{u}_{\partial V}) + p\mathbf{u} \end{pmatrix} - \frac{1}{Re_0} \begin{pmatrix} \mathbf{0} \\ \underline{\tau} \\ \underline{\tau}\mathbf{u} - \mathbf{q} \end{pmatrix}$$
(2.2)

in arbitrary Lagrangian-Eulerian formulation (ALE) [41]. The flux tensors are computed using the pressure p, the control volume surface velocity $\mathbf{u}_{\partial V}$, and the unit tensor \mathbf{I} .

The stress tensor in a Newtonian fluid at zero bulk velocity is given by

$$\underline{\tau} = \mu(T)(\nabla \mathbf{u} + (\nabla \mathbf{u})^T) - \frac{2}{3}\mu(T)(\nabla \cdot \mathbf{u}) \underline{\mathbf{I}}$$
 (2.3)

with the viscosity $\mu(T)$ [2]. The dynamic viscosity $\mu(T)$ is computed by Sutherland's Law [107, 117] which reads

$$\mu(T) = T^{3/2} \frac{1 + \overline{S_{\mu}}/\overline{T_0}}{T + \overline{S_{\mu}}/\overline{T_0}}$$
 (2.4)

with the Sutherland constant S_{μ} , the reference temperature T_0 , and the fluid temperature T derived from the equation of state Eq. 2.8. The reference temperature in all configurations is $T_0 = 273.15~K$ unless noted otherwise.

The heat flux is based on Fourier's law

$$\mathbf{q} = -\frac{1}{Pr_0(\gamma - 1)}k(T)\nabla T \tag{2.5}$$

which derives the thermal conductivity k(T) from the Sutherland law [107, 117]

$$k(T) = T^{3/2} \frac{1 + S_k / T_0}{T + S_k / T_0}$$
(2.6)

using the Sutherland constant S_k .

In order to efficiently solve the equations, all variables are given in their non-dimensional form. The non-dimensionalization of the variables is described in Appendix A.

The Reynolds number and the Prandtl number are given by

$$Re_0 = \frac{\rho_0 a_0 L_{ref}}{\mu_0}$$
 and $Pr = \frac{c_p \mu_0}{k_0}$ (2.7)

with the reference length L_{ref} , the speed of sound $a_0 = \sqrt{\gamma p_0/\rho_0}$ computed using the heat capacity ratio $\gamma = 1.4$ for air, and the specific heat c_p at constant pressure.

The set of equations is closed by the ideal gas law in non-dimensional form which reads

$$\gamma p = \rho T. \tag{2.8}$$

2.2 Solid phase

An arbitrarily shaped, rigid, or deformable body of volume $\{v|v \in V(t)\}$ with the surface $\Gamma(t) = \delta V(t)$, propagating through a fluid of volume V at time t is considered.

Thermal conduction in such solid phase is described by the conservation of enthalpy without heat sources

$$\frac{d}{dt} \int_{V(t)} \rho h dV + \oint_{\partial V(t)} [\rho h \mathbf{u} - F o_{ref} k_p(T) \nabla T] \cdot \mathbf{n} dA = 0,$$
 (2.9)

with the specific enthalpy h and the Fourier number Fo_{ref}

$$Fo_{ref} = \frac{k_{s,ref}t_s}{\rho_{ref}L_{ref}^2c_p} \tag{2.10}$$

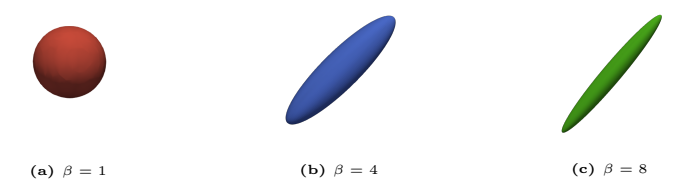


Fig. 2.1: Investigated are spherical and ellipsoidal particles in the aspect ratio range $1 \le \beta \le 8$.

where the time scale can be chosen as, e.g., $t_s = L_{ref}/u_{ref}$.

The quantity $k_{s,ref}$ represents the reference thermal conductivity of the solid body.

In the fluid domain, Fourier's law Eq. 2.5 is used to determine the heat flux, where the thermal conductivity is formulated as a function of the local temperature Eq. 2.4. In the case of phase changes, relevant in solidification or evaporation systems, the thermal conductivity possesses a strongly non-linear distribution as a function of the temperature.

The non-linear thermal conductivity in the solid phase can be accounted for by using piecewise analytical functions or look-up tables for the determination of $k_p(T)$. An example of such an analytical function is given in Mason et al. [69] for biomass particles. However, a detailed discussion of phase changes in the solid phase is beyond the scope of this thesis.

In the present thesis, the focus is on particles of spherical or ellipsoidal shape. These are characterized by the aspect ratio

$$\beta = \frac{c}{a} \tag{2.11}$$

with the condition

$$\frac{x^2}{a^2} + \frac{y^2}{b^2} + \frac{z^2}{c^2} = 1, (2.12)$$

where a, b, and c are half the length of the principal axes. Spherical particles are described by uniform axis length, i.e., a=b=c resulting in $\beta=1$. In this thesis only prolate ellipsoidal particles are investigated where the two minor axes are equal, i.e., a=b and c>a ($\beta>1$). Examples are given in Fig. 2.1

To ensure that all particles, irrespective of their aspect ratio, have the same mass, the individual axis lengths a,b, and c are scaled such that all particles have the same volume, i.e., $V_{eq} = \frac{4\pi}{3} \cdot a \cdot b \cdot c = \frac{4\pi}{3} \cdot \left(\frac{d_{eq}}{2}\right)^3$, which is based on the volume-equivalent diameter d_{eq} describing the diameter of a sphere with the same volume.

The particle motion in this thesis is unrestricted and non-forced, i.e., free motion of arbitrarily shaped geometries is considered. The motion is determined by the mechanical loads on the surfaces of the bodies, resulting in translational and rotational movement.

The linear movement of the particle center of mass is expressed by Newton's second law which describes the linear acceleration

$$m\frac{d\mathbf{u_p}}{dt} - m\mathbf{g} = \mathbf{F}_p \tag{2.13}$$

using the particle mass m, the derivative of the particle velocity $\frac{d\mathbf{u}_{\mathbf{p}}}{dt}$, and the vector of gravitational forces \mathbf{g} . The subscript $(\cdot)_p$ denotes the particle quantities.

The torque exerted by the fluid on the particle is given by

$$\hat{\mathcal{I}}\frac{d\hat{\omega}}{dt} + \hat{\omega} \times (\hat{\mathcal{I}}\hat{\omega}) = \hat{\mathcal{T}}_{p}$$
(2.14)

with the angular velocity $\hat{\omega}$ and is considered in a particle-aligned reference frame indicated by the superscript $\hat{(\cdot)}$.

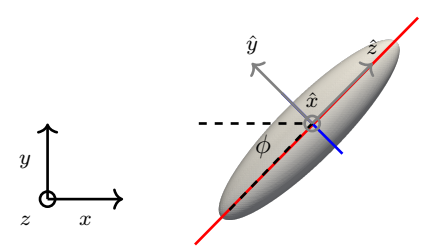


Fig. 2.2: Global coordinate system (x, y, z), particle fixed coordinate system $(\hat{x}, \hat{y}, \hat{z})$, and inclination angle ϕ . The aspect ratio β is the ratio of the major axis c in red and the minor axis a in blue limited by the particle dimensions. The angle ϕ is in relation to the streamwise flow direction.

The global coordinate system (x, y, z) is fixed at the global fluid center of mass, whereas the particle frame of reference $(\hat{x}, \hat{y}, \hat{z})$ is fixed at the particle center of mass of each particle as illustrated in Fig. 2.2. The relative rotation between the two coordinate systems is given by a quaternion-based notation [103].

The force \mathbf{F}_p acting on the surfaces of the bodies $\Gamma(t)$ is described by the pressure and shear-stress distributions which are integrated over all surfaces. The force

$$\mathbf{F}_{p} = \oint_{\Gamma_{p}} (-p\mathbf{n} + \underline{\tau} \cdot \mathbf{n}) \ dA, \tag{2.15}$$

and the torque

$$\mathcal{T}_{p} = \oint_{\Gamma_{p}} (\mathbf{x} - \mathbf{x}_{p}) \times (-p\mathbf{n} + \underline{\tau} \cdot \mathbf{n}) \ dA$$
 (2.16)

with the distance between the particle center of mass and the surface position $x-x_p$, are related to the bodies center of mass and are used to determine the mechanical loads on the bodies.

2.3 Multiphase energy exchange

The conservative exchange of mass, momentum, and energy is ensured by the interface line between the fluid and the solid phase. In the case of solids, there is no transfer of mass, i.e., the mass of the particles is constant and mass transfers, such as those that occur during combustion or phase changes, are not considered. This is expressed by the fluid velocity at the surface

$$\mathbf{u}(\mathbf{x}, \mathbf{t}) = \mathbf{u}_{\mathbf{p}} + \omega_{\mathbf{p}} \times (\mathbf{x} - \mathbf{r}_{p}) \tag{2.17}$$

such that the mass flux vanishes.

The transfer of momentum is calculated by considering the shear stresses and the pressure forces on the individual particle surfaces. Considering the identity

$$(\mathbf{a} \times \mathbf{b}) \cdot \mathbf{c} = (\mathbf{b} \times \mathbf{c}) \cdot \mathbf{a} \tag{2.18}$$

with Eq. 2.15 for the linear forces and Eq. 2.16 for the rotational forces, the transfer rate of kinetic energy transferred from the particle to the fluid is given by

$$\psi(t) = \sum_{p=1}^{N_p} \psi_p = -\sum_{p=1}^{N_p} (\mathbf{F_p} \cdot \mathbf{u_p} + \mathcal{T}_{\mathbf{p}} \cdot \omega_{\mathbf{p}}). \tag{2.19}$$

The dissipation rate of the fluid kinetic energy is described by the inner tensor product $A: B = A_{ij}B_{ji}$, i.e.,

$$\epsilon(t) = \int_{V_f} \epsilon(t)dV = \int_{V_f} \left[\underline{\tau} : (\nabla \mathbf{u}) - (\nabla \cdot \mathbf{u})p\right]dV, \tag{2.20}$$

in the fluid control volume V_f . The control volume $V_f = \sum_p \backslash \Gamma_p$ with the volume surrounding the particle \sum_p and the particle volume Γ_p encapsulates the particles and the fluid within a certain volume of the particle surfaces. The control volume is attached to the moving surface of the particle. For more detail the reader is referred to Schneiders et al. [100].

The energy exchange at the particle surfaces can be positive or negative, i.e., energy can be transferred from the particle to the fluid and vice versa. On the other hand, the particle-induced dissipation rate on the fluid is always considered positive. In this thesis, the notation that a positive sign of $\psi(t)$ results in energy transferred from the particle to the fluid is considered.

The temporal change of total kinetic energy $E_k = \int_{\gamma} \frac{1}{2} \rho \mathbf{u}^2 dV$ inside the fluid domain is governed by the exchange of kinetic energy $\psi(t)$ between the particle and the fluid, and the fluid dissipation $\epsilon(t)$. The rate of energy change inside the fluid is therefore described by the equation

$$\frac{\partial E_k}{\partial t} = \psi(t) - \epsilon(t). \tag{2.21}$$

The transfer of thermal energy differs significantly from the transport of kinetic energy. As expressed in Eq. 2.19 and Eq. 2.20, the transport of kinetic energy E_k is mainly caused by pressure and shear forces at the surfaces due to relative motion between the particle and the local carrier fluid. In contrast, the exchange of thermal energy across material interface boundaries is driven by the temperature gradient ∇T as evidenced in Ch. 3.6 and Eq. 2.5. The coupling of the viscosity and the temperature within the fluid is described by the Sutherland law Eq. 2.4.

The transfer of thermal energy occurs by three primary mechanisms: conduction, convection, and radiation.

Inside the fluid domain, convection is the main driver of thermal energy exchange as visible in Eq. 2.1. In the solid phase, conduction is the predominant mechanism (Eq. 2.9). On the interface line, i.e., the coupling of the different phases, convection and radiation are responsible for the bulk of the exchange. However, radiation has been neglected in all cases.

In the isothermal setup, the particle surfaces are considered adiabatic or isothermal

adiabatic
$$k(T) \frac{\partial T}{\partial n} = 0, \mathbf{x} \in \Gamma(t),$$
 (2.22)

isothermal
$$T(\mathbf{x}) = T_{\Gamma}, \mathbf{x} \in \Gamma(t).$$
 (2.23)

Due to the non-linearity and the high complexity of the interaction in non-isothermal setups, the exchange of thermal energy cannot be described directly. For this reason, a new coupling method was developed and will be described in more detail in Ch. 3.6.

The particle Stokes number based on the time scale $\tau_0 = D/u$ of the turbulent flow in the exit cross section of the pipe at x/D = 0 used in Ch. 5 is

$$St_0 = \frac{Re}{18} \cdot \frac{\rho_p}{\rho_f} \cdot \left(\frac{d_{eq}}{D}\right)^2 \tag{2.24}$$

as commonly seen in the analysis of interaction between particle and free jet flow [62]. The quantity d_{eq} is the volume-equivalent particle diameter and $\frac{\rho_p}{\rho_f}$ is the ratio of particle and fluid densities.

The heat transfer between a solid boundary and the surrounding fluid is quantified by the dimensionless Nusselt number

$$Nu = \frac{h L_{ref}}{k} = \frac{Q L_{ref}}{k A \Lambda T}, \tag{2.25}$$

with the convective heat transfer coefficient h, the temperature difference between the surface and the fluid ΔT , and the total heat flux $Q = \oint_A \mathbf{q}(\mathbf{x}) \cdot \mathbf{n} \, dA$ integrated over the surface area A in the normal direction \mathbf{n} .

2.4 Fluid-solid interface line

The individual surfaces of all bodies are described by a signed-distance level-set function $\Psi(\mathbf{x},t)$. The distance of each cell to the nearest surface is calculated following the convention that values $\Psi(\mathbf{x},t)>0$ are outside of a body and values $\Psi(\mathbf{x},t)<0$ are inside of a body. The position of the surfaces is represented by the zero contour, i.e., $\Psi(\mathbf{x},t)=0$. The bodies and the corresponding surfaces are advanced in time by the transport equation

$$\frac{\partial \Psi_i}{\partial t} + \mathbf{u}_{\Gamma,i}(t) \cdot \nabla \Psi_t = 0 \tag{2.26}$$

with $\mathbf{u}_{\Gamma,i}(t)$ being the respective surface velocity.

For solid simple geometries, an analytical level-set approach can be used. This makes the reconstruction of the level-set field trivial and allows for optimizations in how the field advances in time. The reconstruction of the field at each time step is based on the following steps:

- 1. The relative position, i.e., the position in x, y, and z direction, the particle orientation, and the radii of the particles are given in vector notation. With this, the particle surface contour and the corresponding surface locations are well defined.
- 2. The particle surface contour is computed and the distance of each cell to the nearest surface is obtained by minimizing the distance of the cell center coordinate

to the closest bodies nearby

$$\Psi(\mathbf{x}, t) = \min \mathbf{x} - \mathbf{x}_{\Gamma} \begin{cases}
> 0 & x \in V_f(t), \\
= 0 & x \in \Gamma(t), \\
< 0 & x \in V_p(t),
\end{cases}$$
(2.27)

with the cell position \mathbf{x} and the surface position \mathbf{x}_{Γ} .

In the present work, a multi level-set approach is used for all applications. This means that each cell calculates and stores N level-set values. The individual level-set values refer to different bodies, so that the reconstruction of the bodies in densely populated areas and in complex geometries remains sharp and accurate [32]. A combined level-set field, the zero level-set field $\Psi_0(\mathbf{x},t)$, is constructed from all interface elements

$$\Psi_0(\mathbf{x}, t) = \min\left(\sum_{i=1}^N \Psi_i(\mathbf{x}, t)\right), \tag{2.28}$$

and

$$\Psi_0(\mathbf{x},t) = -\sqrt{\sum_{i=1}^N \Psi_i(\mathbf{x},t)}$$
 (2.29)

if all level-set fields $\Psi_i(\mathbf{x},t) < 0$, to simplify the prescription of the interface line.

For the consideration of several particles in narrow areas or the calculation of complex geometries, the information of all level-set fields is used to ensure a sharp resolution. The analytical approach to the level-set field allows simplifications in how the field is advanced in time. The method and the changes are described in more detail in Ch. 3.3.3.1.

To advance each particle in time and space, all acting forces on the particle surfaces are integrated and reduced to its center of mass (cf. Ch. 2.2). The new particle position and orientation are used for the derivation of $\Psi(\mathbf{x}, t+1)$ in the next timestep.

3 Numerical method

The numerical realization of the isothermal and non-isothermal setups is conducted by coupled multiphysics solvers in an immersed-boundary framework.

The solvers utilize various numerical methods to compute distinct aspects of multiphase flows. A finite volume formulation is employed to compute the fluid phase. Two novel solvers are developed for modeling the particle dynamics: a parallel particle solver and an enthalpy solver. The particle solver tracks the particle movement while the enthalpy solver models heat dynamics within fully-resolved bodies of arbitrary shape. All computations are conducted on a joint Cartesian grid.

More details are given in the following. First, the underlying joint grid approach is presented, and the adaptive mesh refinement and the mechanism used to offset the varying workload of each subdomain, i.e., the load balancing algorithm, are described. Afterwards, the different numerical methods are discussed and the corresponding formulations are presented. In closing, the coupling approach of the multiphysics problems is outlined and the approach to the application of boundary conditions is presented.

3.1 Cartesian grid

The investigations in this work are conducted within the open-source simulation framework m-AIA (multiphysics-Aerodynamisches Institut Aachen, https://git.rwth-aachen.de/aia/m-AIA/m-AIA) that uses a joint Cartesian grid [63]. This joint grid encompasses the entire domain of interest and is adapted by the various solvers and parallelized by the message passing interface (MPI) standard. The joint grid can be adapted in full or in parts by the individual solvers as exemplarily shown in Fig. 3.1 where the domain of interest discussed in Ch. 5 is split into two distinct subdomains.

A hierarchical Cartesian mesh structure is used which features an octree data structure [36]. To be more precise, in three-dimensional configurations an octree data structure is used which reduces to a quadtree structure in two-dimensional space and to a binary tree in one-dimensional space. The hierarchical structure is such that information, as, e.g., parent-child relationships, cell levels, and more, are readily available. All mesh cells can be refined or coarsened. A two-dimensional visualization of a quadtree is illustrated in Fig. 3.2, where 2^n child cells are added or removed to or from a cell for an n-dimensional case. The extension to a three-dimensional

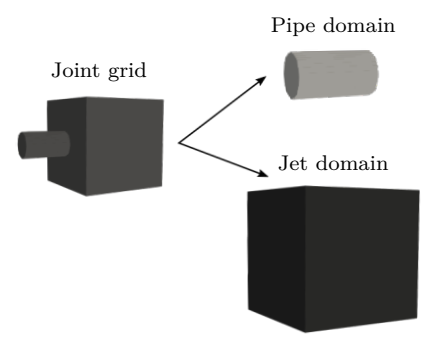


Fig. 3.1: Multi-solver approach. A joint grid is split up into distinct domains which are subsequently adapted by different solvers. A mapping from each solver subdomain to the joint grid is kept which simplifies the linking of cells within different solvers.

octree is analogous. Additionally, neighboring relations are stored to derive spatial relationships in n-dimensional space.

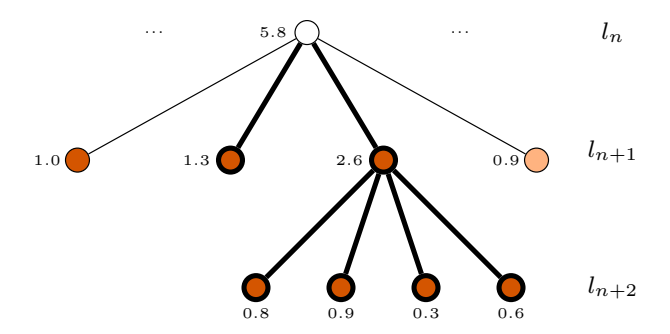


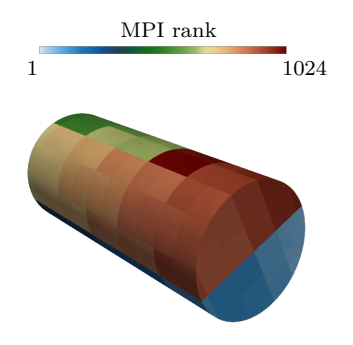
Fig. 3.2: Quadtree structure of the hierarchical Cartesian mesh. The numbers next to each node in the quadtree indicate cell weights, which approximate the total computational workload of a cell and are accumulated up the tree. The partition level l_{n+1} is used for the grid decomposition as indicated by the different node colors. The bold lines indicate that the cell branch is assigned to multiple solvers. The varying workload of the leaf cells is caused by the varying amount of computational work for each cell. For example, boundary cells show increased weights in comparison to regular grid cells due to additional computations.

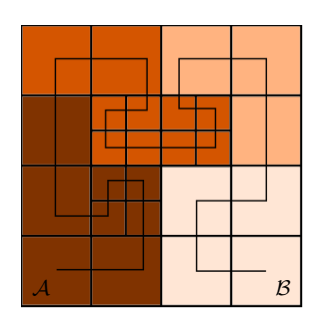
The flexibility of the octree structure facilitates the expansion of individual branches, thereby generating varying levels of branch depths and cell refinement levels. This process is referred to as adaptive mesh refinement and is further explained in Ch. 3.1.2.

With the aforementioned structure, the grid allows easy decomposition for massively parallel systems while maintaining good flexibility.

3.1.1 Domain decomposition

The size of the simulations examined in this thesis exceeds $\mathcal{O}(10^9)$ cells, necessitating the implementation on high-performance computing systems. To this end, the domain of investigation must be parallelized to maintain optimal performance and to efficiently address the integration tasks. The decomposition of the grid into multiple subdomains, as exemplarily depicted in Fig. 3.3a, facilitates the efficient execution of the integration tasks by allocating distinct MPI computing cores to each subdomain. The Message Passing Interface (MPI) is a standardized communication protocol that enables parallel processes running on distributed computing systems to exchange data efficiently. It provides a framework for developing high-performance applications by supporting point-to-point and collective communication between multiple processes.





(a) Resulting distribution of the pipe domain from (b) Space-filling Hilbert curve through a two-the Hilbert curve for 1024 computing cores. dimensional locally refined grid. The different colors result in distinct subdomains assigned to individual MPI ranks.

Fig. 3.3: General approach and exemplary result of the domain decomposition of the joint Cartesian grid. A space-filling Hilbert curve reduces the decomposition of the threedimensional grid into a one-dimensional problem. All cells along the curve are weighted and used for the decomposition to divide the domain into approximately evenly weighted chunks.

The decomposition of the joint grid is conducted by marking the grid cells by a space-filling one-dimensional curve on a pre-defined partition level, the Hilbert curve (see Fig. 3.3b). The space-filling curve reduces the three-dimensional physical space to a one-dimensional curve which preserves locality such that compact domains are achieved [73]. Each cell is assigned a weight that represents its respective workload which is accumulated up the tree branches to the partition level. The cells at the partition level are assigned a unique Hilbert id and subsequently split into approximately even lengths. These chunks are assigned to all available MPI

ranks based on the accumulated weights along the curve. This results in balanced workloads across all MPI ranks, thereby ensuring symmetrical computation times across the subdomains. This approach minimizes the exchanges between neighboring domains and enhances the overall efficiency.

The mechanism facilitates compact subdomains throughout all solvers which allows the direct in-memory exchange of data. Due to the partitioning of the joint mesh, cells assigned to multiple solvers will be allocated to the same MPI rank. Especially, the cells cut by body surfaces which belong to multiple domains are guaranteed to be located on the same MPI rank. Therefore, the data exchange between the fluid and solid domain, which is necessary for the formulation of the boundary conditions shown in Ch. 3.6, does not involve any communication between parallel partitions and can be performed by local memory transfer.

Unlike other coupling approaches for conjugate heat transfer, such as segregated solvers or overset meshes, no communication or other computationally expensive procedures such as frequent determination of grid connections or global communication are required. This significantly improves the performance of the coupling methodology for massively parallel HPC systems.

For simulations with high local refinement levels, a large number of leaf cells can be associated with a single partition level cell, for which the computational work may become larger than the average work load. In such cases, a partition level shift is used for the domain decomposition to achieve a better load distribution. In this approach, the Hilbert curve traverses down the octree of the mesh such that a cell of a higher refinement level than the partition level is used for the decomposition as shown in Fig. 3.4.

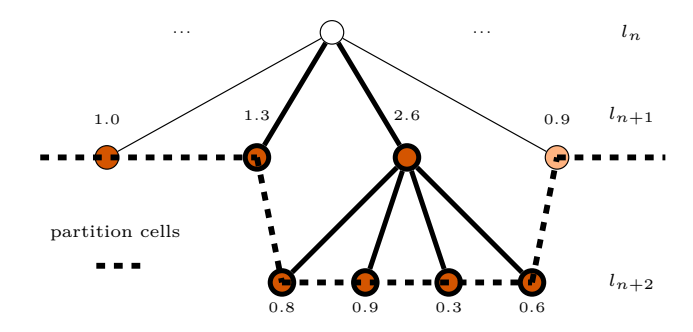


Fig. 3.4: Hierarchical quadtree structure of the hierarchical Cartesian mesh, the partition cells are indicated by the dashed line. The partition level shifts the local level of partition cells such that a finer granular decomposition is ensured.

This shift is performed locally, for which an example is shown in Fig. 3.4, where the cells at the higher level are traversed by the Hilbert curve used for the decomposition.

A finer granular decomposition can then be performed such that a better workload balance is achieved.

3.1.2 Adaptive mesh refinement

The octree structure of the grid stores the domain in a hierarchical tree, thereby facilitating the derivation of parent-child relationships. The structure is exploited with individual branches of the tree deviating from an isotropic grid refinement, i.e., undergoing further refinement or coarsening. An example of the resulting domain is given in Fig. 3.5. The local alteration of the grid is referred to as adaptive mesh refinement (AMR).

Cells can be refined or coarsened as shown in Fig. 3.3. In the case of, e.g., refinement, a cell is split into halves in each spatial direction, i.e., 2^n child cells are added to a cell in n-dimensional space. This process ensures the maintenance of the grid's structural integrity, leading to a well-defined and fully operational grid.

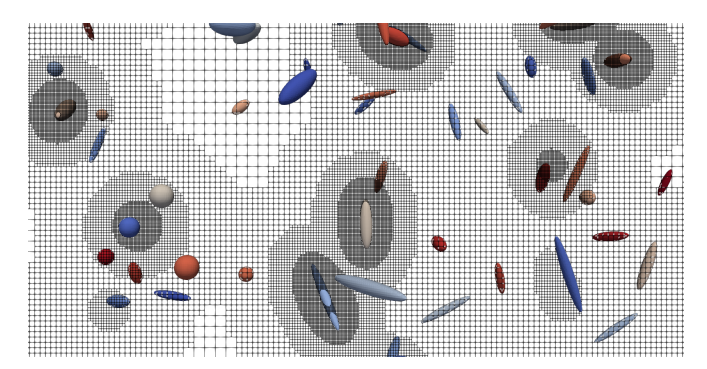


Fig. 3.5: Locally adapted mesh. The immediate area around the particle interface lines is refined to the highest level to ensure the proper resolution of all boundary layer phenomena. During the simulation run, additional refinement based on statistical sensors adapts the flow field.

The mesh is locally refined or coarsened based on runtime statistics defined by each cell, so called sensors. This allows the adaptation of the grid based on the instantaneous flow solution. To elaborate, a cell is further refined if its cell value exceeds the multiple of the root mean square (RMS) of all cells for the given property. To illustrate an example, a cell is further refined if its temperature derivative exceeds a pre-defined multiple of the statistical RMS value of all cells. A common approach involves further refining the grid where the solution exhibits increased complex dynamics and steep derivatives while simultaneously coarsening less dynamic areas. This approach reduces the overall workload in comparison to an isotropic grid at the highest refinement level while maintaining high accuracy in complex parts of the grid.

Additionally, static refinement sensors refine the cells independent of the RMS values. This is, for example, employed in the refinement of moving bodies as found in this thesis. The area surrounding the moving particles is always refined to the highest refinement level to ensure the proper resolution of all boundary layer phenomena and the stark gradients therein, see Fig. 3.5.

However, due to the varying work loads imposed by the additional computations, such as boundary cells or varying grid tree depths, the computational time of the individual MPI subdomains may increase over time. MPI synchronization then results in large idle times and wasted computational resources. To address this, an advanced load-balancing algorithm is employed which will be outlined next.

3.1.3 Dynamic load balancing

Due to the varying complexity of the computational tasks within the different subdomains, the runtime of the individual subdomains will eventually differ. For example, the boundary cell generation and the ensuing cut face intersection increase the computational complexity and thus, the local work load. Additionally, memory constraints of HPC systems will lead the simulation to run out of memory and crash.

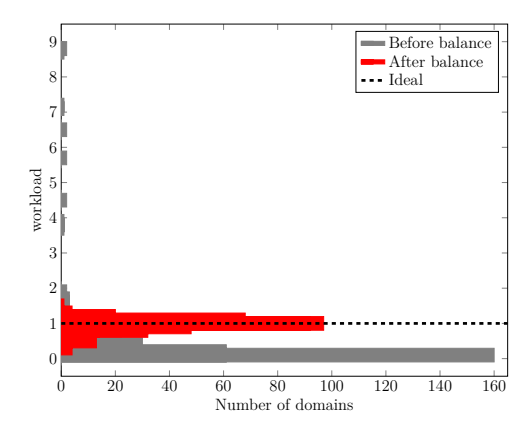


Fig. 3.6: Load distribution of 512 MPI ranks before and after balancing. The ideal workload is w=1.0 for all ranks. The occasional high workloads result in large idle times throughout all domains slowing down the overall computation.

This phenomenon is particularly evident in the context of the free movement of particles, where the trajectory of the particles is not known in advance. An example load distribution is given in Fig. 3.6. The computationally most expensive performance and memory operations in this thesis are the generation of the cut cells, the varying workload due to adaptive mesh refinement, and the overlap of cells assigned to multiple solvers (see Ch. 3.5). To counteract the time-dependent

change of workload, an algorithm to periodically redistribute the grid throughout all available MPI ranks is supported, termed dynamic load balancing [77, 114].

The redistribution of cells between the different MPI subdomains is analogous to the initial grid decomposition. The partition cells are traversed by a Hilbert curve and subsequently evaluated for their accumulated workload [77, 114]. Two different approaches for the evaluation of the total workload are considered:

- Static cell weights [114]. Cell properties are associated with a static weight value. For instance, a cell that functions as a boundary cell exhibits elevated levels of complexity and computational demands, consequently resulting in a greater weight value.
- Dynamic cell weighting [77]. Timers to track the effective computing times
 for each subdomain are utilized. The effective computational runtime of each
 MPI rank is evaluated in relation to the different cells, and a more reliable
 representation of the computational workload is achieved.

Subsequent to the computation of all cell weights, the weights are accumulated up the grid tree such that each partition cell is given an accurate representation of its downstream branch workloads. The Hilbert curve along the partition cells is split into approximately equivalent workloads and distributed among all available MPI ranks. This process is analogous to the initial grid decomposition.

Effectively, the three-dimensional problem is reduced to a one-dimensional problem which simplifies the assignment of the grid to the individual MPI ranks. Due to the spatial relationship depicted by the continuous curve, neighboring exchanges between window and halo cells in the distinct MPI domains are minimized, thus ensuring workload equalization across all available hardware. Here, window cells refer to the active boundary regions of each subdomain where data exchange with adjacent domains occurs, while halo cells (also known as ghost cells) are copies of neighboring cell values stored locally to enable consistent computations across domain boundaries. However, due to the dynamic nature of the particles, frequent repetition of the balancing process is necessary to maintain high performance and balanced memory usage.

3.2 Parallel particle tracking

To meet the requirements of large-scale simulations of several thousand fully-resolved particles of varying shape, a new parallel particle class is presented. The main task of the particle solver is to track the particle dynamics in time, compute the particle rotation due to the mechanical forces, and account for collisions between the particles. The focus lies on high efficiency in distributed computing, low memory usage, and on minimizing the exchange of the individual MPI subdomains.

3.2.1 Parallelization

The distribution of particles is based on a local/global id approach in which individual particles are present only in subdomains which they intersect with. In this context, the relative position of particles within the grid determines their allocation with particles assigned to the cell that their center of mass intersects. This cell then owns the respective particle. As the particle moves, ownership of the particle is transferred to the new cell. In the case of ownership of an internal cell, i.e., not a halo cell, the particle is designated as local. In the event that a particle surface intersects a halo cell within a certain distance, the particle is transferred to the corresponding neighboring domain and labeled there as a halo body. The additional distance ensures the proper synchronization of the individual domains during the adaptive mesh refinement and the seamless transition of bodies at the boundaries of two subdomains.

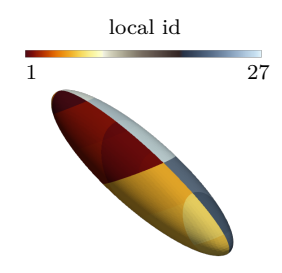


Fig. 3.7: Local ids of a single particle in different domains. The local id is assisted by a global id which is consistent in all domains.

This principle is extended to the concept of periodic boundaries which can be prescribed anywhere in the flow field. Consequently, a given particle may be designated as either local, halo, or periodic. The ownership and status of halo and periodic bodies change to local when the respective cell center intersects with an internal cell. Updates of local, halo, and periodic bodies are performed only when changes in the particle distribution necessitate communication.

Within each subdomain, particles are accounted for and referenced by their body id which ranges from 0-N in each subdomain, with N denoting the number of particles intersecting with the respective subdomain. The continuous movement of particles can result in different ids between individual subdomains. To ensure the proper exchange of particle data, an additional unique identifier, the global id, is assigned. This id remains constant across all domains and is assigned to each particle individually. In the event of a new particle being added, a new global id is assigned. If a particle leaves the full domain its global id is deleted and marked for reassignment. Halo and periodic bodies have the same global id as their respective window bodies. The usage of a common global id simplifies the tracking of particle

statistics and allows the efficient linking of particles in varying subdomains, including the linking of local and periodic particles.

3.2.2 Temporal integration of the particle dynamics

The particle dynamics are advanced in time by the acting forces at the boundary surfaces (see Eq. 2.15 and Eq. 2.16). The coupling of the particles with the flow field dynamics allows the temporal integration of the particle positions based on the local flow conditions. This achieves a physically correct free movement of the particles in the fluid flow. The predictor-corrector scheme presented by Schneiders et al. [99] is used for time integration.

3.2.2.1 Linear movement

In the predictor step, the acceleration of the previous time step is used to determine the new position. An implicit Newmark scheme

$$\mathbf{a}_{n} = \mathbf{a}_{n-1},$$

$$\mathbf{u}_{n} = \mathbf{u}_{n-1} + \Delta t \cdot 0.5 \cdot (\mathbf{a}_{n-1} + \mathbf{a}_{n}),$$

$$\mathbf{x}_{n} = \mathbf{x}_{n-1} + \Delta t \cdot \mathbf{u}_{n-1} + 0.25 \cdot \Delta t^{2} \cdot (\mathbf{a}_{n-1} + \mathbf{a}_{n}),$$
(3.1)

is used to integrate the acceleration at timestep n in time.

In the corrector step, the hydrodynamic loads of the flow field on the particle surfaces are known and can be determined. The resulting mechanical loads in Eq. 2.15 are integrated and reduced to the particle center of mass. Newton's law is subsequently used to compute the linear acceleration in Eq. 2.13. An implicit Newmark scheme

$$\mathbf{a}_{n} = \frac{\mathbf{F}}{m} + \mathbf{g},$$

$$\mathbf{u}_{n} = \mathbf{u}_{n-1} + \Delta t \cdot 0.5 \cdot (\mathbf{a}_{n-1} + \mathbf{a}_{n}),$$

$$\mathbf{x}_{n} = \mathbf{x}_{n-1} + \Delta t \cdot \mathbf{u}_{n-1} + 0.25 \cdot \Delta t^{2} \cdot (\mathbf{a}_{n-1} + \mathbf{a}_{n}),$$
(3.2)

is used again to integrate the acceleration in the corrector step in time.

3.2.2.2 Rotational movement

The respective particle rotations are updated according to the acting torque \mathcal{T}_p at the particle surfaces by a Crank-Nicolson scheme

$$\hat{I}\hat{\omega}^{n+1} + \frac{\Delta t}{2} \left[\hat{\omega}^{n+1} \times \left(\hat{I}\hat{\omega}^{n+1} \right) \right] = \hat{I}\hat{\omega}^{n} + \frac{\Delta t}{2} \left[\hat{\mathcal{T}}_{p}^{n} + \hat{\mathcal{T}}_{p}^{n+1} - \hat{\omega}^{n} \times \left(\hat{I}\hat{\omega}^{n} \right) \right]$$

(3.3)

$$\epsilon^{n+1} - \frac{\Delta t}{2} \underline{\Omega}(\hat{\omega}^{n+1}) \epsilon^{n+1} = \epsilon^n + \frac{\Delta t}{2} \underline{\Omega}(\hat{\omega}^n) \epsilon^n, \tag{3.4}$$

with the torque in body-frame coordinates $\hat{\mathcal{T}}_{\mathbf{p}}^{\mathbf{j}} = \underline{\mathbf{R}} \left(\epsilon^{\mathbf{j}} \right) \mathcal{T}_{\mathbf{p}}^{\mathbf{j}}$ and the angular velocity in inertial frame $\omega^{j} = \underline{\mathbf{R}} \left(\epsilon^{j} \right)^{-1} \hat{\omega}^{j}$, in a Newton-Raphson iteration scheme. The orthogonal matrix is

$$\underline{\underline{R}}(\epsilon) = \begin{bmatrix}
\epsilon_0^2 + \epsilon_1^2 - \epsilon_2^2 - \epsilon_3^2 & 2(\epsilon_1 \epsilon_2 + \epsilon_0 \epsilon_3) & 2(\epsilon_1 \epsilon_3 - \epsilon_0 \epsilon_2) \\
2(\epsilon_1 \epsilon_2 - \epsilon_0 \epsilon_3) & \epsilon_0^2 - \epsilon_1^2 + \epsilon_2^2 - \epsilon_3^2 & 2(\epsilon_2 \epsilon_3 + \epsilon_0 \epsilon_1) \\
2(\epsilon_1 \epsilon_3 + \epsilon_0 \epsilon_2) & 2(\epsilon_2 \epsilon_3 - \epsilon_0 \epsilon_1) & \epsilon_0^2 - \epsilon_1^2 - \epsilon_2^2 + \epsilon_3^2
\end{bmatrix}$$
(3.5)

and the vector of quaternions is defined by $\epsilon = [\epsilon_0, \epsilon_1, \epsilon_2, \epsilon_3]$.

The new particle positions is used for the next iteration step. Once the iteration within an iteration step j of timestep n is converged, i.e., $\Delta \mathbf{x_{n,j}} - \Delta \mathbf{x_{n,j-1}} \leq \mathcal{R}$, the iteration is concluded and the next timestep is initiated.

3.2.3 Collision model

Collisions are modeled using a modified version of the collision model proposed by Glowinski et al. [29]. In this hard-sphere model, a repulsive force is applied to the respective colliding bodies. This repulsive force acts in opposite normal direction of the colliding bodies to prevent the overlap of the bodies' surfaces. The overlap of solid bodies is ambiguous in the utilized cut-cell method and thus, not feasible. Due to the multi-cut cell method, this means that particle collisions are resolved on a sub-cell length level. Distances of $1/10\,l$ of an uncut cell length l between two colliding surfaces are commonly observed.

The detection of a potential collision for the spherical particles is trivial due to the equidistant body radii. Due to the anisotropic shape of some of the particles and the curvature of the pipe walls in Ch. 5, the collision model is extended to operate on generic non-spherical body shapes. It also includes the point-of-attack in relation to the center of mass such that the rotational momentum is correctly applied.

The collisions of fully-resolved arbitrary shaped solid bodies $(\cdot)_p$ and $(\cdot)_q$ are computed for the contact point which is equivalent to the nearest surfaces of the bodies. No collision is considered if $(\mathbf{x_p} - \mathbf{x_q}) - (r_{max,p} + r_{max,q}) > S$, where the quantities x_p , x_q and $r_{max,p}$, $r_{max,q}$ are the center of mass of the particles and the

maximum radius of the non-spherical, ellipsoidal particles and S defines a minimum gap between the particles.

If a collision occurs, the repulsive force

$$f_{\mathbf{p}} = C_0 \cdot \left(\frac{S - l_d}{S}\right)^2 \cdot \frac{x_{\mathbf{p}} - x_{\mathbf{q}}}{l_d} \tag{3.6}$$

with the coefficient

$$C_0 = f_r \cdot \frac{\frac{1}{2} \cdot (m_p + m_q) \cdot u_{ref}^2}{l_{max}}$$
 (3.7)

is calculated by the repulsive force factor f_r , the particle masses m_p and m_q , the reference velocity u_{ref} , the cell length of an uncut cell l_{max} at the max level, the distance between the surfaces l_d , and the distance between the center of mass $x_p - x_q$ of the body $(\cdot)_p$. The loss of kinetic energy due to collisions and particle deposition at the wall is not considered.

In the present study, the collision model is expanded to include collisions between particles and static bodies. The collision model will be used in Ch. 5 for the calculation of particle-pipe collisions. The collision between static bodies and particles is analogous to collisions between particles. The collision is initiated as exemplarily shown for a particle-pipe wall collision:

- 1. A preliminary estimation $r_{pipe} (\mathbf{x}_p + r_{p,max}) < S$ based on the particle coordinate and the pipe diameter, including the maximum particle radius, yields a numerically cheap prediction if a collision is to be considered.
- 2. In the event that the particle is deemed to be in potential collision with the wall, the distance l_d of the potential collision point is calculated.
- 3. The effective distance is summarized on the basis of all surfaces involved and weighted according to the respective distances. To be more exact, the impact of multiple surface contact points is considered by distance-based weighting. The resulting repulsive force is then related to the center of mass of the particle equivalent to the methodology previously outlined.
- 4. The mass of the particle is used to calculate the force. Given the ambiguous mass of the pipe wall, the mass of the particle is also utilized for this purpose, i.e., $m_p = m_q$. Rotational forces are applied based on the point-of-attack in relation to the center of mass of the particle.

With this approach, collisions between particles and solid static bodies are captured and properly computed. As shown by Yan et al. [119], particle-wall collisions are important in the configuration of particle-laden pipe flow.

3.3 Finite volume solver

A finite volume method is used to discretize the conservation equations in Eq. 2.1 and Eq. 2.9 [36, 98]. This method is adapted for the calculation of moving bodies of arbitrary shape. A monotonically integrated LES (MILES) approach is used where the large-scale turbulent motions are fully resolved and the dissipation of the numerical scheme is used as a sub-grid scale (SGS) for the small-scale motions [71]. The advantage is that no further SGS model has to be explicitly prescribed and no additional terms have to be considered in the Navier-Stokes equations.

3.3.1 Spatial discretization

The inviscid fluxes are approximated by a low-dissipative method of the advection upstream splitting method (AUSM) [70]. The inviscid flux vector in the Cartesian direction i is calculated by

$$\mathbf{H}_{i}^{inv} = \frac{1}{2} \left[M_{i}^{LR} \left(\mathbf{f}^{L} + \mathbf{f}^{R} \right) + \left| M_{i}^{LR} \right| \left(\mathbf{f}^{L} - \mathbf{f}^{R} \right) \right] + \mathbf{p}_{i}$$
 (3.8)

with the local Mach number at the surface

$$M_i^{LR} = \frac{1}{2} \left[(u_i/a)^L + (u_i/a)^R \right]$$
 (3.9)

and under the consideration of

$$\mathbf{f} = [\rho a, \rho a \mathbf{u}, \rho a (E + p/\rho)]^T \tag{3.10}$$

and

$$\mathbf{p}_{i} = \left[p^{L} \left(\frac{1}{2} + \chi \left(u_{i}/a \right)^{L} \right) + p^{R} \left(\frac{1}{2} - \chi \left(u_{i}/a \right)^{R} \right) \right] \begin{pmatrix} 0 \\ \mathbf{e}_{i} \\ 0 \end{pmatrix}. \tag{3.11}$$

Here, the superscripts L and R denote the left- and right-handed states of the surface. The respective cell surface variables are obtained by interpolation using a monotone upstream-centered scheme for conservation laws (MUSCL). The centered variables

$$\mathbf{P} = [u, v, w, \rho, P]^T \tag{3.12}$$

are in their primitive state and are computed by

$$\mathbf{P}_{sf}^{L/R} = \mathbf{P}_{c}^{L/R} + \nabla \mathbf{P}|_{c}^{L/R} \cdot \left(\mathbf{x_{s}} - \mathbf{x}^{L/R}\right)$$
(3.13)

at the surface.

The cell-centered gradients $\nabla \mathbf{P}|_c$ of all primitive variables are resolved by a weighted least-squares reconstruction method

$$\mathbf{P}|_{c} = \sum_{n_{j} \in \mathcal{N}_{|}} \mathbf{C}_{\mathbf{j}} \left(\mathbf{P}_{\mathbf{j}} - \mathbf{P}_{\mathbf{c}} \right)$$
 (3.14)

with the direct neighbors \mathcal{N}_{\rfloor} in each spatial direction. The reconstruction constants $\mathbf{C}_{\mathbf{i}}$ are obtained from solving the least-squares problem of the linear equation

$$\underline{\mathbf{W}} \cdot \underline{\mathbf{A}} \nabla \mathbf{P}|_{c}^{L/R} = \underline{\mathbf{W}} \begin{bmatrix} \mathbf{P}_{\mathbf{n}_{1}} - \mathbf{P}_{\mathbf{c}} \\ \mathbf{P}_{\mathbf{n}_{2}} - \mathbf{P}_{\mathbf{c}} \\ \vdots \end{bmatrix}$$
(3.15)

with

$$\mathbf{A} = \begin{bmatrix} \Delta x_{n_1} & \Delta y_{n_1} & \Delta z_{n_1} \\ \Delta x_{n_2} & \Delta y_{n_2} & \Delta z_{n_2} \\ \vdots & \vdots & \vdots \end{bmatrix}$$
(3.16)

where $\mathbf{x}_{n_j} = \mathbf{x}_j - \mathbf{x}_c$ is the distance between the neighbor $(\cdot)_j$ and the cell center $(\cdot)_c$. This results in the equation system

$$\mathbf{C}_{j} = \underline{\mathbf{A}}^{+}\underline{\mathbf{W}}^{2} \cdot \frac{1}{l} \tag{3.17}$$

where $(\cdot)^+$ remarks the pseudo-inverse of the respective quantity and l the width of the respective uncut cell. The diagonal matrix $\underline{\mathbf{W}} = diag(w_{n_1}, w_{n_2}, ...)$ weights the impact of each cell in the least-squares reconstruction with

$$w_{n_j} = \zeta(V_j) \left[1 + \left(\frac{\Delta \mathbf{x_{n_j}}^2}{l^2} \right) \right]^{-1/2}, \tag{3.18}$$

which includes the volume weighting $\zeta(V_j)$ to handle gradually vanishing small cells from the reconstruction stencil.

The viscid fluxes are solved by a central differences scheme where the surface variables are averaged in their primitive state, i.e.,

$$\mathbf{P}_{sf}^{L/R} = \frac{1}{2} \left(\mathbf{P}_{sf}^{L} + \mathbf{P}_{sf}^{R} \right) \tag{3.19}$$

with the surfaces states left and right of the surface obtained as described in Eq. 3.13. The surface gradients $\nabla \mathbf{P}_{sf}$ with respect to the cell variables \mathbf{P} are obtained from the recentering approach proposed by Berger & Aftosmis [11]. Further details on the described numerical methods can be found in Hartmann et al. [38], Günther et al. [32], and Schneiders et al. [99].

3.3.2 Temporal integration

The solution of the flow field is advanced in time by an explicit five-step Runge-Kutta scheme. Being second-order accurate, the Runge-Kutta scheme is specifically optimized for setups with moving bodies as presented in Schneiders et al. [98, 99].

The scheme reads

$$\begin{aligned} (\mathbf{Q}V)^{(0)} &= (\mathbf{Q}V)^{n}, \\ (\mathbf{Q}V)^{(1)} &= (\mathbf{Q}V)^{(0)} - \Delta t \mathbf{R}(t^{n}; \mathbf{Q}^{(0)}), \\ (\mathbf{Q}V)^{(k)} &= (\mathbf{Q}V)^{(0)} - \Delta t [(1 - \alpha_{k-1})\mathbf{R}(t^{n}; \mathbf{Q}^{(0)}) + \dots \\ & \dots + \alpha_{k-1}\mathbf{R}(t^{n+1}; \mathbf{Q}^{(k-1)})], \text{ for } k = 2, \dots, 5, \\ (\mathbf{Q}V)^{n+1} &= (\mathbf{Q}V)^{(5)}, \end{aligned}$$
 (3.20)

where t^n and t^{n+1} refer to the current and the following timestep and k marks the current Runge-Kutta sub-step. The cell surface flux $R(t; \mathbf{Q}^k)$ is approximated by

$$\mathbf{R}(t; \mathbf{Q}^k) = \oint_{\partial V(t)} \left(\underline{\mathbf{H}}^{inv}(\mathbf{Q}^k) - \underline{\mathbf{H}}^{vis}(\mathbf{Q}^k) \right) \cdot \mathbf{n} dA + \mathcal{O}(h^2)$$
 (3.21)

with the Runge-Kutta coefficients $\alpha_k = [1/4, 1/6, 3/8, 1/2, 1]^T$ for a five-step scheme. For low Reynolds number flows, the vector of coefficients $\alpha_k = [0.02514, 0.0718, 0.1757, 0.5, 1]^T$ is used instead.

The original multi-step Runge-Kutta formulation by [45, 48, 110] requires the reconstruction of the residual operator $\mathbf{R}(t; \mathbf{Q}^k)$ at each Runge-Kutta sub-step k. This is necessary to sustain a time-consistent formulation which requires the recomputation of the particle surfaces and the regeneration of the cut-cell geometries. This consequently increases the workload multifold.

In contrast, Eq. 3.20 only reconstructs the residual operator \mathbf{R} and the cut-cell geometries at time levels t_n and t_{n+1} . Within a time step, only the conservative variables \mathbf{Q}^k are updated alongside the geometric conservation law (explained in Ch. 3.3.3.4). This renders the scheme well-suited for the computation of moving particles in fluid flow as a speed-up of 2.5x is achieved [98].

The Courant-Friedrichs-Lewy (CFL) stability constraint dictates the timestep Δt by

$$\Delta t = min\left(C\frac{l_{max}}{|u_i| + a}, \quad C^{vis}\frac{\rho l_{max}^2}{\mu}\right)$$
(3.22)

where l_{max} is the grid length of an uncut cell at the highest refinement level and C and C^{vis} denote the CFL number for the regular and the viscous stability limit.

During the movement of the particles, the diminishing volume of small cut-cells can force instability issues. To avoid stability issues and an infinitesimally small timestep, a small-cell correction is used with a flux redistribution method which is described in Ch. 3.3.3.5.

3.3.3 Immersed-boundary method

An immersed-boundary method (IBM) is used to render the fluid-structure interactions. The surfaces of arbitrary shaped moving bodies are discretized by a sharp cut-cell method. As the surface contours of the particles intersect the Cartesian cells, the cells are recut to accommodate for the penetrating boundary. In other words, the volume of the cell is divided into fluid and solid volume, see Fig. 3.8.

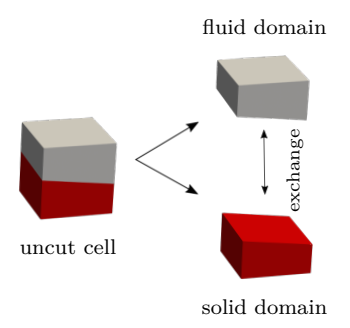


Fig. 3.8: A cut cell containing the body surface is split into its fluid and solid part. The data between the two phases can be exchanged as it is observed in thermal equalization processes.

This ensures that the geometries of the individual bodies are accurately represented while maintaining the conservatism of the Navier-Stokes equations. In particular, a multi-cut cell method is used which allows individual cells to be cut multiple times to ensure the accurate presentation of cells that are penetrated by multiple bodies or complex geometries.

The multi-cut cell method incorporates a higher-order surface approximation [99] which significantly reduces the truncation error near the embedded interface achieving an order of magnitude improvement compared to less accurate methods [1]. However, the increased level of accuracy of the higher-order surface approximation results in larger memory allocations and an increase of the computational complexity. Therefore, the utilized algorithm differentiates between a single-cut cell method and a multi-cut cell method, i.e., the multi-cut cell method is only used for the resolution of the sharp boundary surfaces if necessary. To be more precise, boundary cells which are intersected by a single interface line use a single-cut cell method which is based on a Marching cube algorithm [65] using look-up tables to cover all 256 possible plane intersections. For multiple intersections of a single cell, the intersection problem is split into multiple single intersection problems. The individual intersection problems are then covered by a Marching cube algorithm and the resulting multi-cut cell is derived by polygonal intersection of the fluid domain portion of all individual intersections.

During the intersection process, the fluid volume of the cut cells can become exceedingly small. Then, explicit time-integration schemes require vanishingly small time steps due to the CFL stability constraint. Since this is not feasible, additional process steps are applied to ensure a robust and accurate cut-cell method. An additional geometric volume constraint, the geometric conservation law, and a flux-redistribution technique are used to stabilize such small cut cells while simultaneously ensuring a conservative method. The small cell correction is explained in Ch. 3.3.3.5.

For further information the reader is referred to publications by Hartmann et al. [38], Schneiders et al. [99], and Günther et al. [32].

Small adjustments to the method were necessary to properly compute the intersection of bodies at the domain boundaries. An overview is given in the following where the changes will be discussed.

3.3.3.1 Particle surface contour

As previously outlined, an analytical level-set function is used to derive the level-set values of the flow field. The particles move within the CFL constraint and as such, the temporal change of the particle surface positions is only small. To increase the performance of the solver, a region update algorithm is introduced which exploits the numerical properties of the analytical level-set. Since the full level-set field is known at timestep t_n , the level-set values at timestep t_{n+1} are only updated in a small band surrounding the particles.

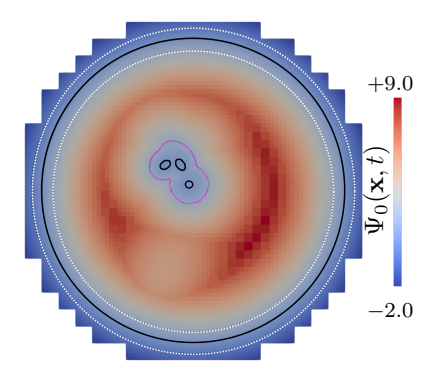


Fig. 3.9: Zero level-set $\Psi_0(\mathbf{x},t)$ of a particle-laden pipe. The black bold line indicates the body surfaces, i.e., the pipe domain (large circle) and the anisotropic particles. The cells outside of the dotted purple and white lines are kept constant during the simulation run unless new bodies penetrate the area.

The combined zero level-set field $\Psi_0(\mathbf{x},t)$ is shown in Fig. 3.9. All values are analytically prescribed as the pipe radius and the particle positions are known along the radii and orientations. In subsequent steps, only the cells in the moving band

(purple dotted line) are updated. The level-set band moves and changes with each particle. Additionally, the level-set values at static non-moving bodies, e.g., the pipe wall, are only updated if other bodies penetrate the respective area, i.e., the white dotted lines in Fig. 3.9.

3.3.3.2 Cut-cell method

The level-set values $\Psi(\mathbf{x},t)$ are cell-based, i.e., they are related to the respective cell center. In the course of the intersection, they are interpolated to the corner points of the cells. All eight neighboring cells of a vertex are used for the interpolation. In the case of level jumps, the corresponding distance is taken into account. The level-set values of the corner points are used for cell intersection. Sign changes are used to determine the position of the surfaces. To be more precise, sign changes between two adjacent nodal level-set values are used to determine cut points along the connecting border where a linear interpolation determines the exact location of the cut.

After that, all cut points are connected by boundary surfaces using a modified Marching Cube triangulation algorithm. Split cells, that is, cells that have two disconnected fluid parts in a single cell, are processed separately as the conservative treatment of these cells needs special consideration. For a more detailed description of the cut-cell methodology, see Schneiders et al. [98].

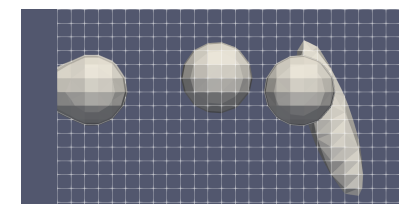
For cells at the domain boundaries, i.e., where less than eight neighboring cells are available and the interpolation is therefore skewed, cells are added outside of the domain by a new algorithm for the adaptive generation of grid cells. The description of the algorithm can be found in Ch. 3.3.3.3.

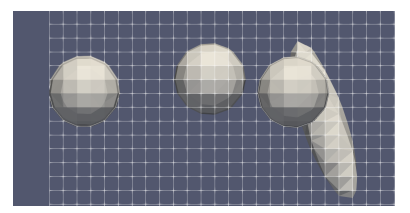
3.3.3.3 Adaptive mesh extension

The cell-based level-set values are interpolated to nodal-based values during cell intersection which can lead to significant distortions at the domain boundaries due to sparse information caused by missing neighboring cells. A visual example is shown in Fig. 3.10. An algorithm termed adaptive mesh extension (AME) is introduced as a solution to this problem. Cells are added to the grid based on runtime information of the solution. That is, the grid is locally extended by the generation of new cells at each individual timestep to ensure the accurate resolution of the particle surfaces while minimizing the computational load. The mesh enhancement is visually shown in Fig. 3.11 where the added cells consist of multiple layers and can be intersected by the moving boundaries.

These cells are a mixture of halo and ghost cells which are regularly taken into account in the flow field and accordingly contribute to the flow field development.

The addition of such cells can be conducted based on different data. In the stabilization of the particles, the level-set information is used for determination if new cells are to be added. If a cell-centered level-set $\Psi(\mathbf{x},t)$ value is below a certain threshold at the domain boundary, i.e., an interface line is nearby, cells are added





the particle entering the domain is clearly distorted

(a) No adaptive mesh extension. The surfaces of (b) Adaptive mesh extension enabled. The particle entering the domain is properly resolved.

Fig. 3.10: Adaptive mesh extension. The adaptive enhancement of the grid at the domain boundaries ensures the proper resolution of the level-set field by locally extending the flow field. Resulting are proper body surfaces which ensures the correct conservatism of the approach.

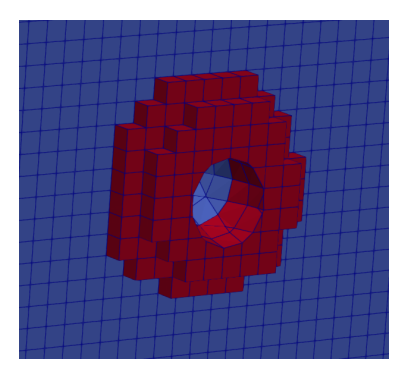


Fig. 3.11: Adaptive mesh extension visualized. The blue cells are regular grid cells and the red cells are the adaptively added cells added during the simulation run, i.e., at each timestep. Note the smooth transition of the particle intersection of the regular grid cells and the added cells.

outside of the regular domain. This ensures the proper resolution of all particle surfaces at the domain boundaries.

However, since these cells are added based on flow field information, the initial value prescription is to be thought of. From this perspective, these cells are similar to ghost cells in that initial values are extracted from the flow field. In Ch. 5, periodicity is applied to the added cells in the pipe domain.

Two main problems of the immersed-boundary method as implemented in the used code are targeted:

1. The intersection of the respective cells is ensured beyond the domain limits and surface smearing is avoided. Due to the cell extension, nodal information is ensured to be accurate through the boundaries and no distortions of the

moving body are risked. As a result, the conservatism of the cut cell method is maintained. By avoiding geometry changes due to numerical irregularities, the correct redistribution of the flux due to pressure, momentum, and thermal gradients is facilitated.

2. The added cells have the option to be linked to the regular grid cells. Due to this, fluid energy can be transported out of the domain and is not echoed back. This means that other mechanisms such as sponge layers become superfluous at the boundaries. The prescription of cells according to other solution field data than the level-set value is supported.

The handling of particles exiting the domain is stabilized using this algorithm by one-sided linking of the flux dynamics. Consequently, sponge layers and the regular prescription of cell values for boundary cells containing moving bodies are avoided. This solves, for example, the problem of setting the outflow boundary conditions which are not generic anymore if the cell contains particle surfaces. The application of the boundary conditions is adapted to fit this novel mechanism.

3.3.3.4 Geometric conservation law

To avoid non-physical perturbations of the discrete solution of moving bodies, an additional transport term has to be satisfied. The so-called geometric conservation law (GCL) is necessary in an arbitrary Lagrangian-Eulerian formulation to regulate the reconstruction of the variables \mathbf{Q} from the volumetric quantities $\mathbf{Q}V$.

The GCL formulation is adapted to Eq. 3.20 and reads

$$V^{(0)} = V^{n},$$

$$V^{(1)} = V^{(0)} - \Delta t (\mathbf{u} \cdot \mathbf{n} A)_{\Gamma}^{n},$$

$$V^{(k)} = V^{(0)} - \Delta t ((1 - \alpha_{k-1})(\mathbf{u} \cdot \mathbf{n} A)_{\Gamma}^{n} + \alpha_{k-1}(\mathbf{u} \cdot \mathbf{n} A)_{\Gamma}^{n}), \text{ for } k = 2, ..., s,$$

$$V^{n+1} = V^{s}.$$
(3.23)

The law states that the discrete formulation in the reworked Runge-Kutta scheme does not alter a uniform flow field even under the motion of the control volumes, i.e., the moving particles. It does so by updating the volumes V of the cut-cells at each Runge-Kutta sub-step k while keeping all other geometric quantities constant for the remainder of the timestep. Fulfilling the geometric conservation law ensures that the timestep Δt , as computed, in Eq. 3.22 does not become infinitesimally small.

3.3.3.5 Small cell correction

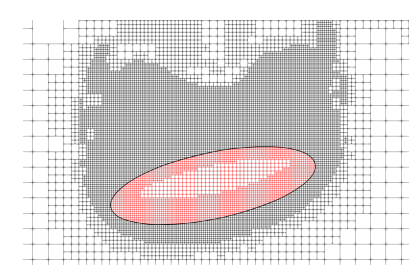
Due to particle movement, the fluid volume of a given cell can become arbitrarily small before vanishing in cut-cell methods. This reduces the domain of influence which renders explicit schemes unstable. While different strategies to combat this problem exist, an interpolation routine coupled with a flux-redistribution step developed by Schneiders et al. [99] is used in the present thesis. Here, cells with vanishing cell

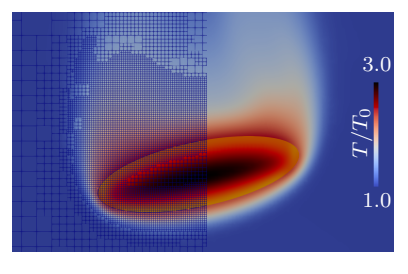
volumina are reconstructed using a least-squares reconstruction. The ensuing delta of the conservative variables and the reconstructed data is subsequently redistributed to the neighboring cells. A detailed description is given in Schneiders et al. [99].

3.4 Enthalpy solver

A novel solver for the computation of fully-resolved solid bodies is introduced. The aim of this solver is to solve the conservation equation for the enthalpy Eq. 2.9 which facilitates the solution of heat dynamics inside of solid or deformable bodies.

To accomplish this, the novel solver is based on the finite volume solver presented in Ch. 3.3. The level-set method and the multi-cut cell method are used to properly model the dynamics inside of the particles.





- (a) Adaptively refined grid of the fluid domain in (b) Resulting temperature distribution within the black and the enthalpy domain in red.
 - particle and the fluid domain.

Fig. 3.12: Modeling of two coupled domains, a fluid domain and a solid domain. Notice the consistent description of the interface line which results in the exact split of a shared cell into a fluid and solid cell which allows the conservative linking of the multiphysics domains

The enthalpy solver is used to model the heat transfer dynamics of solid bodies of arbitrary complex shape. Moving bodies are fully supported and the conservation of thermal energy is ensured by the usage of the aforementioned mechanisms.

While arbitrarily shaped bodies, such as, e.g., combustion engines, heated plates, or turbo machinery, are imaginable, the solver is used for the computation of spherical and ellipsoidal particles under the influence of thermal energy in this thesis.

Eq. 2.9 is solved to map the thermal dynamics inside a solid body. The goal is to investigate the interaction of the particles and the surrounding carrier fluid.

As seen in Fig. 3.12, the solver is set up such that the interface lines between the fluid and solid domain are synchronized at all times. The common interface line then allows the linking of the two domains to exchange data as, e.g., observed in thermal equalization processes. The solver is part of an investigation to conjugate heat transfer and the approach to the exchange of the thermal energy will be described in detail in Ch. 3.6.

3.5 Coupling

The coupling of information between different modalities specialized in the computation of varying phases is a fundamental task in multiphysics simulations. The term coupling refers to the synchronization and the exchange of information between different solvers and phases [115].

The spatial and temporal coupling is presented in this section. Particular emphasis is placed on the implementation on high-performance computing systems that utilize distributed memory methods. In the following, the overall concept and mechanism of the coupling is presented. After that, a specific example on how the approach is used in this thesis is outlined by the description of the slicing technique used to link the pipe and the jet domain described in Ch. 5.

3.5.1 Coupling mechanism

The efficient coupling of the different solvers is ensured by the usage of distinct MPI ranks along the Hilbert curve. As shown in Fig. 3.3, the distribution of the cells along the Hilbert curve is based on the course of the curve which splits the joint grid into distinct subdomains and distributes them to all available MPI ranks. The different solvers are subsequently imposed onto the MPI ranks, i.e., all solvers are assigned the respective subdomains such that the solvers contain the same cells. This allows the direct exchange between the solvers as no out-of-memory exchanges need to be initiated, i.e., the numerical structure of the joint Cartesian grid allows information to be exchanged with minimal interference of the computation process. The processes are defined so that the exchange can be carried out at pre-defined points in time. This increases the overall performance and reduces idle times significantly.

This is in contrast to other methods, such as segregated solvers, where distinct ranks are applied to solve the different equations in the individual subdomains. The coupling between two solvers in such methods can be realized by libraries such as PreCICE [14]. When it comes to the execution of the overall solution method on HPC systems, the solvers in such methods are assigned to different ranks executed on parallel compute hardware. This requires a domain decompositioning where the individual compute load on each rank of the parallel executed tasks becomes identical to achieve a high parallel efficiency. This approach can be useful for fixed meshes, but can become considerably less efficient when solution adaptive meshes are used. Then, a repartitioning of the overall problem and a regeneration of the connectivity between the solvers can become necessary after each mesh adaptation step.

Additionally, the accurate prediction of the dynamics across the fluid-solid interface poses significantly larger challenges when the solid surface moves through the fluid flow. In this case, the spatial domains are dynamically changing, which can be taken into account by various strategies. One option is to use deformable meshes where the fluid domain is constantly adapted to the solid domain. This approach, however,

requires mesh regeneration efforts, which may be possible for small body movements, but become computationally unfeasible when several solid bodies with arbitrary shape and movement have to be resolved. Alternatively, one could use overset or chimera meshes [5, 9, 10, 108], in which the solid body and the fluid domain in the vicinity of the body is resolved with a mesh moving with the body such that the interface line between the fluid and the solid mesh does not change. In this case, the overset formulation, however, poses the same challenges as when a pure fluid flow simulation with moving bodies is conducted [108]. The overset mesh formulation becomes especially difficult to implement on parallel compute systems since the connection between the overset mesh points has to be regenerated possibly in each time step, which can involve considerable communication effort and thus, reduces the parallel efficiency. Furthermore, when the distance of solid bodies becomes small, the problem arises, which of the overlapping mesh points will be chosen to define the local solution. Finally, it is difficult to formulate a fully conservative solution method, due to the arbitrary cut interfaces of the overset mesh cells [108]. Recent developments in hole-cutting methods provide more advanced solutions for the execution on parallel compute systems [17], however, with only moderate parallel efficiency.

3.5.2 Solver coupling

The coupling of multiple solvers is facilitated by a mapping of the solver cell id to the joint grid cell id. Since the joint grid is split into parts of varying lengths which are adapted by the different MPI ranks, the joint grid cell id and the solver-specific cell id will differ. To maintain a direct connection between the cell ids, additional lookup tables are stored. With this, the direct derivation of the local cell to the joint grid cell by each solver is possible and the coupling of the same cell in different solvers is straightforward.

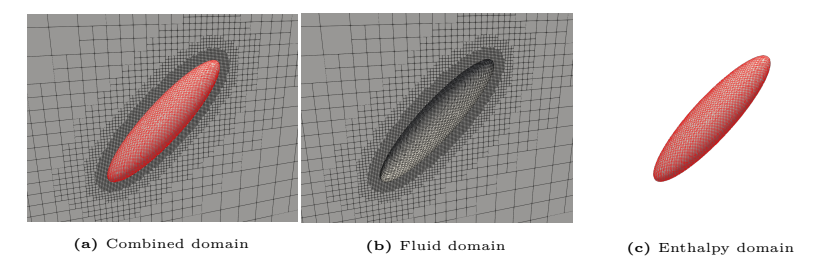


Fig. 3.13: Illustration of how the joint grid is used by multiple solvers. The fluid domain and the solid domain consist of the same grid cells which are subsequently marked as active/inactive by the cut-cell generation. With this approach, the moving of the particles is ensured and the linking of the interface line is consistent through the different domains.

Due to the direct connection of cells within different solvers, information of any kind, e.g., cell information or surface data, can be exchanged and synchronized. Additionally, solver class specific data such as, e.g., variables or arrays, can be exchanged. This facilitates the efficient exchange of information between different phases and modalities.

The coupling algorithm additionally makes use of the predefined work tasks defined by each solver. Once a specific work task is finished, the coupling algorithm is called and synchronizes/exchanges the respective data.

The coupling of the particle solver (Ch. 3.2) and the finite volume solver (Ch. 3.3) is shown here as an example. The aim is to simulate a particle-laden flow in which the finite volume solver computes the flow dynamics and the particle solver solves the motion equations for the individual particles.

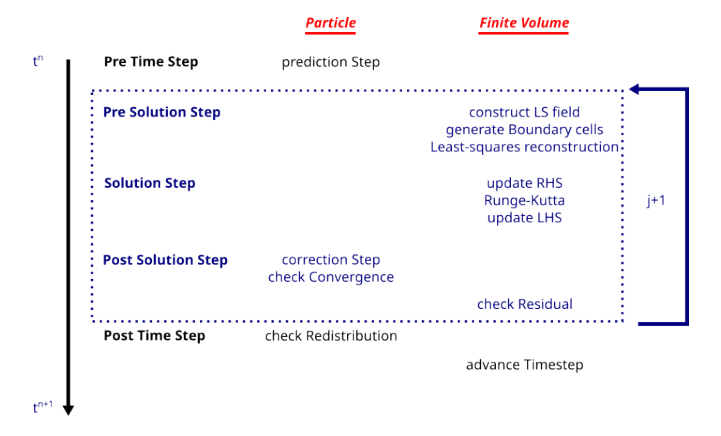


Fig. 3.14: Flowchart of the coupled solution of the particle solver and the finite volume solver. The inner iteration of the predictor-correct scheme encapsulates the solution step and the pre- and post-solution step.

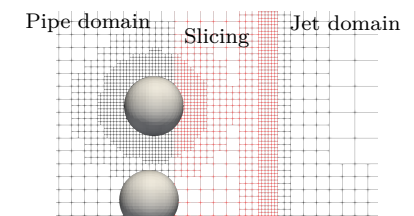
As shown in Fig. 3.14, the overall structure is such that the different solvers are called alternating. Once the necessary data for the temporal integration of the particle data is known, the exchange is initiated. Subsequently, the particles are integrated in time and collisions are accounted for before the data is synchronized for the ensuing computations. Hence, additional constraints in the execution order are accounted for and the scheme is rendered such that the mechanisms of the previously described predictor-corrector Runge-Kutta is exploited.

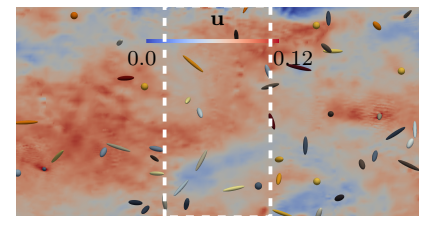
The coupling mechanism facilitates the exchange of different kind of information. In the following, an example used in Ch. 5 is given where two fluid domains are coupled.

3.5.3 Slicing technique

The investigation in Ch. 5 inspects particle-laden turbulent free jet flow. One of the challenges associated with numerical studies of free jet flow are the inflow conditions. The most common approach is the generation of synthetic turbulence, which is characterized by random velocity fluctuations in the inflow cross-sectional area. If a particle-laden problem is considered, particles with random orientations, velocities, and rotational dynamics are additionally assumed. It is obvious that the aforementioned particle properties fail to align with the turbulent characteristics of the flow field. Consequently, there is a discrepancy between the inflow boundary conditions and the actual physical conditions. This discrepancy is often exacerbated by the interaction between the particle and the carrier fluid. This discrepancy alters the results as significant turbulence development is observed in the near-field of the jet exit [8, 15].

To achieve an accurate solution of a particle-laden free jet flow, it is essential to assume boundary conditions that are coherent and naturally developed. The solution of a concurrently computed periodic turbulent pipe flow generates such inflow conditions. A slicing technique is used to inject the instantaneous solution of a particle-laden turbulent pipe flow as inflow condition to the free jet domain. To be more precise, the domains partially overlap and the overlapping areas are coupled such that a continuous flow is achieved as shown in Fig. 3.15.





- (a) Split of the joint Cartesian grid into two do-(b) The velocity u in the pipe and jet domain. The mains, a pipe domain and a jet domain as used in Ch. 5. The red cells are consistent in both domains which allows the direct exchange of data between the two domain at these cells.
 - slicing technique is applied within the white boundaries. The smooth transition between the two domains is clearly discernible.

Fig. 3.15: The coupling of multiple solvers facilitates the usage of a pipe domain as inflow condition for a jet domain. The transfer of data is conducted by a slicing technique on overlapping cells which results in a smooth transition of the flow field through the domain boundaries.

This achieves a coupling of the flow states, providing naturally evolved and physically correct flow and particle information as flow- and particle information are transferred. The coupling takes place on one or both sides. In the case of Ch. 5, there is a one-sided transfer from the pipe flow to the free jet.

A mapping between the corresponding cells of both domains is stored to facilitate the exchange of the data. The respective cells are exchanged at each Runge-Kutta sub-state. Two options are implemented:

- The direct exchange of the conservative variables: the conservative variables
 Q of each cell in the target area are overwritten by the source variables. In a multi-layer exchange, a transition function can be defined.
- 2. The exchange of RHS information: the cell data is updated using the flux through the cell surfaces, summarized as an update of the right hand side. In the second coupling mode, the corresponding right hand side information is exchanged and applied to the target cells.

The consistent transfer of cell information from one domain to the other results in a continuous flow and coherent turbulent structures. A validation of the method is given in Ch. 4.3.

In contrast to the flow field, the exchange of particle information is more complex. Due to the parallel structure of the particle class, further MPI exchanges are necessary.

To avoid duplicates of the same particle, a mapping of already existing particles is stored in the overlapping areas. The computationally cheap mapping is queried when new bodies cross the periodic boundary. If the mapping returns negative, the particle is added to the jet domain by transferring all particle properties, i.e., velocities, rotational dynamics, and more. During the transfer, the global number of bodies and the global ids are also updated and synchronized within the MPI subdomains.

The exchange of the flow field and the particle data results in physically correct flow and coherent particle information as input boundary conditions for the free jet. No further assumptions for the inflow condition are needed and the correct mixing and development of the turbulent scales is ensured in the jet near-field area.

3.5.3.1 Flow periodicity

To continuously supply data of coherent information to the jet domain, periodicity is applied at the pipe in- and outlet. Periodicity is applied by means of a cell-mapping. Multiple layers of cells are marked as source and target cells upon which the exchange is initiated. Subsequently, the mapping is used for the update of the conservative variables ${\bf Q}$ or the RHS information at each Runge-Kutta sub-stage. The modalities of the previously described slicing technique are mirrored. Two different update methods are implemented:

- 1. The direct exchange of the conservative variables
- 2. The exchange of RHS information to update the conservative variables

In addition to the update of the conservative variables, additional information of the boundary cells is exchanged to ensure the proper transfer of the dynamics of the periodic boundaries. The periodicity of the spherical and ellipsoidal bodies is conducted by the previously described particle solver. Periodic ghost particles are added upon the crossing of the periodic boundaries. These particles mirror their local counterpart under the assumption of an adjusted particle position. Once the particles center of mass of a periodic ghost particle intersects the new domain, the local/periodic body status is switched. Upon leaving the periodic boundaries, the periodic ghost particle is removed.

With the coupling of the fluid cells and the solid bodies to the periodic boundaries, the efficient coupling of the scheme is achieved. The periodicity shows to be fully conservative and well equipped to model the periodic dynamics of the flow field and the particles.

3.6 Application of boundary conditions

The boundary conditions are formulated using multiple ghost cells in a multi-cut cell method [99]. The cut-cell algorithm properly reshapes the respective cells according to the body or phase interfaces. Multiple cuts of a single cell are possible, i.e., more than one cut surface can be generated per cell. This allows several surface elements of one or several bodies to intersect a cell, which can happen, e.g., with complex geometric shapes or bodies at a small distance. Each boundary surface is connected to its corresponding ghost cell allowing an accurate formulation of the corresponding boundary conditions for each cut surface [99].

The computation of the ghost cell variables is conducted using an image point I normal to the boundary surface. The resulting values at the image point location are reconstructed using a second-order accurate least-squares reconstruction scheme. The ghost cell values G are determined at a mirror position

$$\mathbf{x}_{G} = \mathbf{x}_{C} - max\left(2\Psi, \ \Psi + \frac{l}{2}\right) \cdot \mathbf{n}_{\Gamma}$$
(3.24)

to the image point I, see Fig. 3.16, where Ψ is the distance between the cell center and the surface and l is the length of an uncut cell.

The boundary conditions are formulated using primitive variables. For the solid phase and the fluid phase, the ghost cell velocities $\mathbf{u}_{\mathbf{G}}$ are determined by Dirichlet boundary conditions

$$\mathbf{u}_{\mathbf{G}}(\mathbf{x},t) = 2\,\mathbf{u}_{\mathbf{\Gamma}}(\mathbf{x},t) - \mathbf{u}_{\mathbf{I}}(\mathbf{x},t),\tag{3.25}$$

where $\mathbf{u}_{\Gamma}(\mathbf{x},t)$ denotes the body surface velocity and $\mathbf{u}_{\mathbf{I}}(\mathbf{x},t)$ the velocity at the image point.

Robin boundary conditions

$$\frac{p_C - p_G}{\Psi + h/2} + \kappa \frac{\Psi p_G + h/2 p_C}{\Psi + h/2} = 0 \tag{3.26}$$

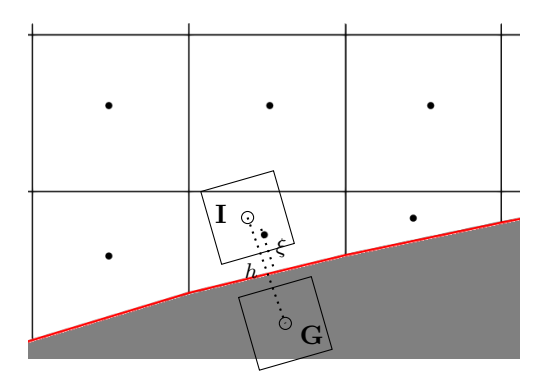


Fig. 3.16: Schematic of the prescription of ghost cells. Ghost cell values G are determined at a mirror position of a reconstructed image point I at a distance h. A multiple ghost cell approach is used for the simulation.

are prescribed for the fluid ghost cell pressure p_G defined by the distance Ψ from the cell to the boundary surface and based on the fluid cell pressure p_C and the distance from the cell position to the ghost cell h. The quantity $\kappa = \gamma T_{\Gamma}^{-1} (D\mathbf{u}/Dt \cdot \mathbf{n})_{\Gamma}$ is defined by the substantial material derivative $D\mathbf{u}/Dt \cdot \mathbf{n}$ and the temperature T_{Γ} on the surface Γ [98].

In the isothermal case, the density is prescribed either for isothermal or adiabatic configurations analogous to the derivation of p_G .

In the non-isothermal configurations, specific boundary conditions for the density in the fluid phase and for the temperature in the solid phase are prescribed. The prescription is outlined in the following.

Conjugate Heat Transfer Coupling

The coupling of fully-resolved solid bodies and the surrounding carrier fluid is conducted by conjugate heat transfer. Conjugate heat transfer dictates that the surface temperature T_{Γ} and the heat flux q_{Γ} through the surface Γ must be equal for the fluid and solid phases [51], i.e.,

$$T_f|_{\Gamma} = T_s|_{\Gamma} = T_{\Gamma} \tag{3.27a}$$

$$q_f|_{\Gamma} = q_s|_{\Gamma} = q_{\Gamma} , \qquad (3.27b)$$

where the heat flux is defined as $q_i = k \left(\frac{\partial T_i}{\partial n} \right)$.

To fulfill these conditions and maintain energy conservation, an iterative procedure is proposed. Estimates for the initial surface temperature values indicated by the superscript $(\cdot)^0$ in the fluid and solid phase are determined by the respective cell values for the temperature $T_{s,c}$ and $T_{f,c}$ and temperature gradients next to the

surface Γ . Subsequently, the weighted mean of both surface values is considered as initial value for T_{Γ}^0 with

$$T_f^0|_{\Gamma} = T_{f,c} - \mathbf{n_f} \cdot \nabla \mathbf{T_{f,c}}$$
(3.28a)

$$T_s^0|_{\Gamma} = T_{s,c} - \mathbf{n_s} \cdot \nabla \mathbf{T_{s,c}}$$
 (3.28b)

$$T_{\Gamma}^0 = d_f \cdot T_f^0 + d_s \cdot T_s^0 \tag{3.28c}$$

where $\mathbf{n_i}$ is a unit normal vector and d_f and d_s are the normalized surface distances, the sum of which is unity.

Using the initial surface temperature T^0_{Γ} , the temperature gradient and thus, the resulting heat flux can be calculated in both phases independently from each other. The resulting heat fluxes q^{ν}_f and q^{ν}_s are used to update the surface temperature in subsequent iteration steps $\nu+1$ by

$$T_{\Gamma}^{\nu+1} = T_{\Gamma}^{\nu} - \alpha \cdot \left(q_f^{\nu} - q_s^{\nu} \right) . \tag{3.29}$$

The factor $\alpha = \epsilon \frac{L_{ref}}{\overline{k_0}}$ represents a non-dimensionalized scaled step size where ϵ can be a constant or a function, see e.g. Kingma & Ba [56], L_{ref} is a reference length, and k_0 being a reference thermal conductivity.

During the iteration process, the differences in the heat fluxes in the fluid and solid decrease such that a converged value for the body surface temperature T_{Γ} is determined. The iteration process is considered converged when the difference of the heat fluxes defined by the L1-Norm $\mathcal{R} = \frac{L_{ref}}{k_0} \cdot \left| \left| q_f^{\nu}/T_{f,ref} - q_s^{\nu}/T_{s,ref} \right| \right|$ satisfies the condition $\mathcal{R} < 10^{-14}$, i.e., the difference is almost machine zero.

Typically, this threshold value is met in less than 15 iterations. When the converged solution for T_{Γ} is obtained, the resulting temperature is used as a surface value for both domains, and the ghost cell values are computed as described in the last chapter.

Choice of step size α

The choice of the scaled step size α in Eq. 3.29 determines the rate of convergence for the surface temperature. Too small a choice of the step size can result in a large number of iterations or, if the convergence threshold is not reached or not chosen small enough, in a loss of energy conservation. If α is chosen too large, the iteration may not converge or even diverge.

Fig. 3.17 shows the residual \mathcal{R} as function of the iteration steps s_{it} for a specific cell surface. The predetermined convergence criterium $\mathcal{R} < 10^{-14}$ is met within 7 iterations steps for the unscaled step size $\alpha = 0.05$ for a non-dimensional temperature difference between the fluid cell and the corresponding solid cell adjacent to the surface of $\Delta T = 2(T_s - T_f)/(T_s + T_f) = 0.08$.

For a larger step size α , Fig. 3.17 shows that the solution converges slower (dotted line) or does diverge (red line). This is a well-known problem in iterative algorithms used to find a minimum value. If the algorithm fails to reach the convergence

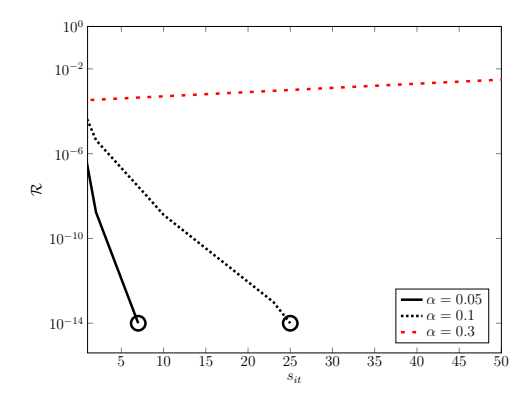


Fig. 3.17: Logarithmic plot of the residual \mathcal{R} as a function of the iteration step count s_{it} for $\alpha=0.05$ (solid, black), $\alpha=0.1$ (dotted, black), $\alpha=0.3$ (dashed, red). The circle indicates, that the convergence threshold is reached. The choice of the step width α clearly impacts the convergence rate. For $\alpha=0.3$, the iteration does not converge.

threshold within a pre-defined maximum number of iterations, a loss of conservation can occur. This can be avoided with a meaningful choice of α .

The update of the surface temperature T_{Γ} is computed independent from the local spatial step. However, with coarser mesh spacings, the temperature values at the cell centers of the neighbouring fluid and solid cells T_f and T_s show potentially larger differences. This increase in the temperature difference may necessitate larger step sizes α or more iteration steps to reach convergence.

Further impact of the mesh spacing on the solution is discussed in the grid convergence study presented in Ch. 4.3.1.

For the solid phase, the temperature occurs directly in Eq. 2.9, whereas in the fluid phase (Eq. 2.1), the surface temperature is taken into account via the non-dimensional equation of state $T = \gamma p/\rho$. Note that the same approach can be used for moving bodies, for which the surface pressure is determined by the Robin boundary condition Eq. 3.26.

4 Solver validation

The numerical methods applied in this thesis have been used and validated in a wide range of different fundamental and engineering-relevant fields. Flow problems such as turbo machinery [13, 44], aeroacoustics [30, 95], or wind turbines [46, 47] are only a few examples. The numerical methods for the particle calculations have been extensively validated in isotropic turbulent flows [25, 97, 100].

However, as modifications and novel code contribute to the simulation framework m-AIA in the context of this thesis, the following chapter shows the validation of the framework in the different investigated fields.

First, the modifications necessary to compute the particle-laden pipe-jet flow discussed in Ch. 5 are outlined. The dynamics inside the pipe and free jet domain are compared to reference results from the literature.

To evaluate the numerical approaches in regard to the heat dynamics used in Ch. 6, different aspects of thermal dynamics are investigated. The dynamics of the heat exchanges are relatively unexplored in the current simulation framework and new additions are contributed. The dynamics of isothermal heat transfer, used in the derivation of the correlation equation for the Nusselt number Nu outlined in Ch. 6.1, are shown first. Subsequently, the novel enthalpy solver is evaluated in a wide array of generic test cases of varying shape and configuration. The coupling efficiency is evaluated and its suitability for high performance computing systems is highlighted.

4.1 Turbulent pipe-free jet flow

First, the approach used in Ch. 5 is validated where a particle-laden pipe flow is coupled to turbulent free jet flow. The investigation of the coupled pipe-jet flow is susceptible to various numerical inaccuracies due to its complex interactions. To validate the approach, the velocity profile inside the pipe and the jet domain is inspected. This validates not only the dynamics inside each domain, but also the slicing technique and its approach to supply proper inflow conditions.

4.1.1 Turbulent pipe flow

The Reynolds number based on the friction velocity is $Re_{\tau}=448$ while it is $Re_{D}=15\,546$ based on the bulk velocity \overline{u}_{b} at the jet inflow section. This is somewhat different from the Reynolds number $Re_{\tau}=500$ in Chin et al. [20, 21] and slightly lower than $Re_{\tau}\approx450$ in Pirozzoli et al. [81]. A 118 million-cell mesh was used with local mesh refinement of the viscous wall layer.

The time and streamwise averaged axial velocity profile as a function of the radial direction r normalized by the centerline velocity \overline{u}_{cl} is compared in Fig. 4.1 with the data of Chin et al. [21]. The results are in close agreement. The maximum discrepancy between the velocity distributions is below 3%. Furthermore, the time-averaged centerline velocity is $\overline{u}_{cl}/u_b=1.27$ which agrees with the result $\overline{u}_{cl}/u_b=1.27$ in Pirozzoli et al. [81].

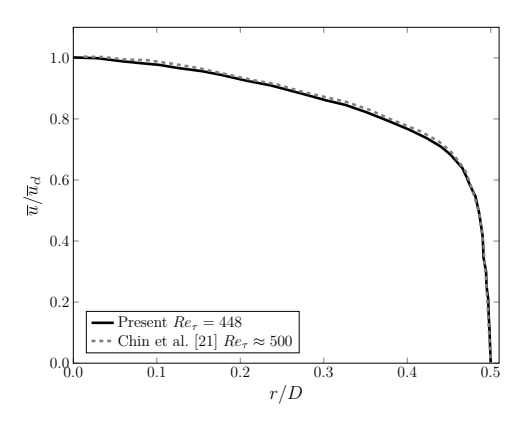


Fig. 4.1: Time and streamwise averaged velocity component $\overline{u}/\overline{u}_{cl}$ normalized by the maximum velocity on the centerline as a function of the radius r/D. The solution is compared with results of Chin et al. [21].

The distribution of the root-mean-square of the velocity fluctuations normalized by the friction velocity u_{τ} is shown in Fig. 4.2. Again, the maximum deviation between the current data and data by Chin et al. [21] is 3% which is acceptable due to the slightly different friction velocity Reynolds numbers.

It is fair to conclude that the velocity field in the single-phase pipe flow is accurately predicted by the numerical method.

4.1.2 Turbulent free jet flow

To further validate the numerical approach for a turbulent free jet including the slicing technique, a single-phase jet is simulated. The Reynolds number $Re_D=15\,546$ is that of the latter discussed particle-laden jet since the single-phase data serve as reference solution for the multiphase solution. The mesh contains 118 million cells for the periodic pipe domain and 593 million cells for the turbulent free jet. Furthermore, the schematic of the turbulent free jet in Fig. 5.2 is also valid for the single-phase flow.

The mean velocity profile $\overline{u}_{cl}/\overline{u}_{cl,x=0}$ along the centerline in the axial direction of the free jet domain is compared with experimental data from Papadopoulos et al. [80] in Fig. 4.3. The authors conducted measurements for two jets at Reynolds numbers

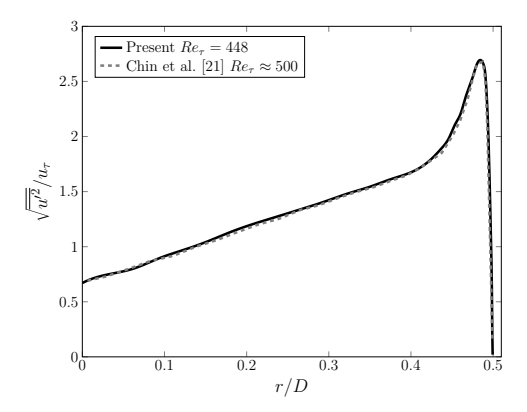


Fig. 4.2: Streamwise root-mean-square velocity fluctuations normalized by the wall-friction velocity $\sqrt{u'^2}/u_{\tau}$ as a function of the distance from the centerline r/D compared with results from Chin et al. [21].

based on the bulk velocity $Re_1 = 13\,300$ and $Re_2 = 17\,500$. In the experimental setup, the jet emerges from a long straight pipe such that a fully-developed turbulent pipe flow at the exit is ensured. The comparison of the present numerical and the experimental results show good agreement. The deviation at various distances from the nozzle exit is below 4%.

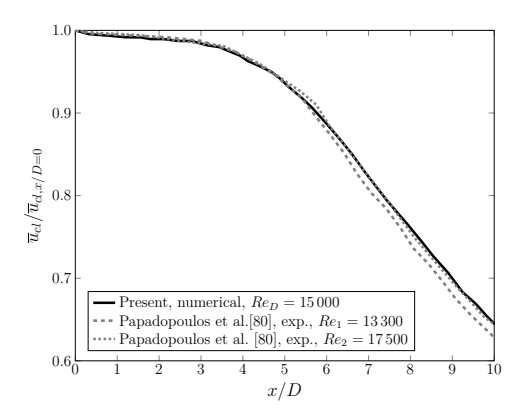


Fig. 4.3: Centerline velocity normalized by the centerline velocity at the nozzle exit $\overline{u}_{cl}/\overline{u}_{cl,0}$ compared with experimental data from Papadopoulos et al. [80].

4.1.3 Conclusions

The comparisons of the results for the turbulent pipe and free jet flow with data from the literature shows the high quality of the current numerical method. The reference data from the literature are matched with high accuracy in the pipe and the free jet domain. The mean velocity across the pipe radius and the velocity fluctuations compare very well to Chin et al. [21]. The turbulent profile is clearly discernible and the maximum centerline velocity matches perfectly with that reported by Pirozzoli et al. [81]. Inside the turbulent free jet flow, the axial decline of velocity is accurate when comparing the present results to Papadopoulos et al. [80] such that the slicing technique is considered validated. Thus, the method can be used to analyze the flow of particle-laden turbulent pipe and free jet flow as shown in Ch. 6.1

4.2 Constant surface temperature

Lagrangian point-particle models reduce the particles to finite-sized small points and describe the interaction between the different phases by correlation equations. This entails simplifications such that the particle surface has a spatially constant temperature. Mirroring this assumption, the derivation of a correlation equation for the Nusselt number Nu is conducted by assuming a constant surface temperature (CST). The mechanisms used in Ch. 6.1 entailing this assumption are evaluated in the following.

4.2.1 Grid convergence study

To assess the quality of the findings discussed in Ch. 6.1, a grid convergence study is presented and the method is validated with special focus on heat transfer. To determine the necessary mesh resolution, the flow at Re=1 and Re=100 over an ellipsoid with an aspect ratio $\beta=8$, a temperature ratio $T_R=1.05$, and an inclination angle $\phi=45^{\circ}$ is considered (Fig. 6.2). At Re=1, the viscous forces dominate the flow, while the pressure forces characterize the flow at Re=100.

This is a very challenging flow problem due to the extended streamwise development of the shear stress on the particle surface and the recirculation in the wake of the particle. In Tab. 4.1, the resolution defined by the minimum cell size per volume-equivalent diameter Δ_{min}/d_{eq} , the Reynolds numbers, and the Nusselt numbers for a static temperature ratio $T_R=1.05$ are listed.

The quality of the solution is determined by the averaged Nusselt number, while the solution for $\Delta_{min}/d_{eq}=1/128$ defines the reference solution. The data shows that for grid resolutions $\Delta_{min}/d_{eq}=1/48$ and finer the percentage deviation of the averaged Nusselt number from the reference value is less than 1%. In other words, this resolution is a good compromise between computational cost and accuracy. Higher resolutions reduce the error only marginally while significantly increasing the computational cost. The decrease of the relative deviation of the Nusselt number as

	$Nu(T_R = 1.05)$				
Δ_{min}/d_{eq}	Re = 1	Re = 100			
1/16	3.12 (1.9%)	11.78 (2.2%)			
1/24	3.14 (1.3%)	11.66 (1.1%)			
1/32	3.16 (0.6%)	11.60 (0.6%)			
1/48	3.17 (0.3%)	11.56 (0.3%)			
1/64	3.18 (0.1%)	11.54 (0.2%)			
1/128	3.18	11.53			

Tab. 4.1: Averaged Nusselt number for each resolution. The deviation in percentage with respect to the reference value for $\Delta_{min}/d_{eq}=1/128$ is given in parentheses.

a function of the mesh resolution in Fig. 4.4 shows the second-order accuracy of the numerical method.

To characterize the impact of the boundary location, i.e., the computational domain sizes defined by the number of cells in the streamwise, spanwise, and normal direction, the boundary dimensions $80 \times 32 \times 32$, $96 \times 48 \times 48$, and $120 \times 64 \times 64$ all scaled by d_{eq} are validated. The deviation between the medium domain and the largest domain is below 1%. Considering these results, the following analysis is based on the domain size $96 \times 48 \times 48$.

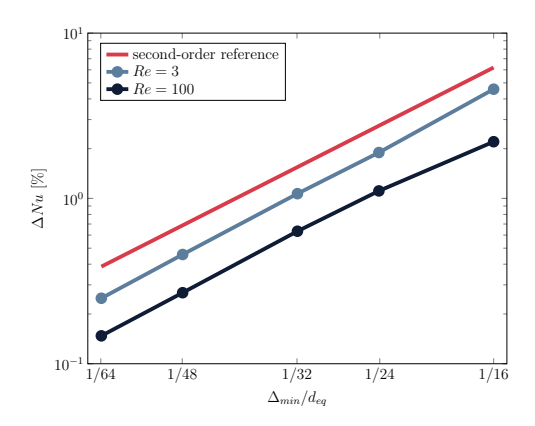


Fig. 4.4: Logarithmic plot of the relative deviations to a fine simulation at $\Delta_{min}/d_{eq}=1/128$. The red line represents the theoretical minimum error attainable by the second-order accurate methods used.

4.2.2 Numerical validation

To validate the numerical method, which has been successfully applied to various fundamental and engineering flow problems such as, e.g., Schneiders et al. [82, 98]

and Pogorelov et al. [82], for heat transfer problems, the flow past a sphere $T_R > 1$ in uniform flow is computed.

First, a sphere with a small temperature ratio $T_R \to 1$ but $T_R > 1$ is considered.

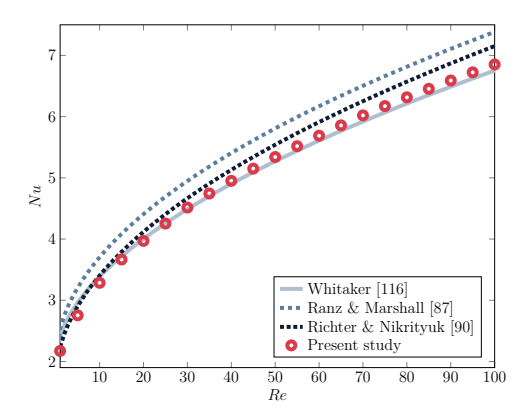


Fig. 4.5: Flow past a sphere at a small temperature ratio $T_R \to 1$. Shown is Nu over Re in comparison with data from Whitaker [116], Ranz & Marshall [87], and Richter & Nikrityuk [90].

The distribution of the Nusselt number Nu as a function of the Reynolds number in Fig. 4.5 shows good agreement with the correlation function by Whitaker [116]. The direct comparison yields the mean deviation to be below 2% with a maximum deviation below 4%. The maximum deviation from the correlation functions by Ranz & Marshall [87] and Richter & Nikrityuk [90] is below 10%.

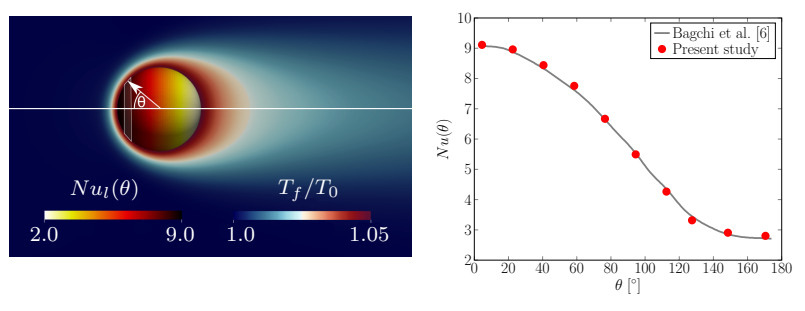
Next, an extended range of temperature ratios is investigated and the results are compared with data from Kurose et al. [61], Nagata et al. [76], and Ganguli & Lele [28] who also varied the fluid properties with the temperature.

Kurose et al. [61] simulated by a finite volume method the flow past a sphere at $T_s/T_0 = 1000K/293K \approx 3.4$ and a sphere at $T_s/T_0 = 293K/1000K \approx 0.3$ for Re = 50 and Re = 100. Nagata et al. [76] analyzed the temperature ratios $T_R = T_S/T_\infty = [0.5, 0.9, 1.1, 1.5, 2.0]$ at Re = 100. Ganguli & Lele [28] inspected a sphere $T_R > 1$ at low Reynolds numbers $Re \le 10$ in the absence of buoyancy. The quantitative comparison of the Nusselt numbers in Tab. 4.2 evidences the maximum deviation to be 10%, which is considered acceptable.

Finally, the distribution of the local Nusselt number, i.e., the spatial heat transfer variation on the surface of a sphere, is determined. That is, the local Nusselt number $Nu_l(\theta)$ is computed in slices and circumferentially averaged about the x-axis (Fig. 4.6a). The results of the local Nusselt number $Nu_l(\theta)$ in the range $0^{\circ} \leq \theta \leq 180^{\circ}$ are compared with the data from Bagchi et al. [6] at Re = 50 and $T_R \to 1$. It is evident that they are in very good agreement (Fig. 4.6b).

Kurose et al. [61]				Ganguli & Lele [28]				
Re = 50	Nu (Kurose)	Nu (current)	ΔNu	Re = 1	Nu (Ganguli)	Nu (current)	ΔNu	
$T_R = 0.3$	11.5	12.70	9.4%	$T_R = 1.1$	2.21	2.26	2.26%	
$T_R = 3.4$	2.8	2.57	8.9%	$T_R = 1.5$	2.06	2.11	2.43%	
				$T_R = 2.0$	1.88	1.93	2.66%	
Re = 100	Nu (Kurose)	Nu (current)	ΔNu	Re = 10	Nu (Ganguli)	Nu (current)	ΔNu	
$T_R = 0.3$	14.9	15.33	2.8%	$T_R = 1.1$	3.17	3.24	2.16%	
$T_R = 3.4$	3.3	3.01	9.6%	$T_R = 1.5$	2.95	3.02	2.32%	
				$T_R = 2.0$	2.69	2.77	2.88%	
Nagata et al. [76]								
Re = 100	Nu (Nagata)	Nu (current)	ΔNu					
$T_R = 0.5$	11.8	12.62	6.5%					
$T_R = 0.9$	8.2	8.64	5.1%					
$T_R = 1.1$	5.5	5.52	0.4%					
$T_R = 1.5$	5.0	4.76	5.0%					
$T_R = 2.0$	4.3	4.29	0.1%					

Tab. 4.2: Flow past a sphere at several T_R for Re = 50 and Re = 100 compared with data from Kurose et al. [61] and Nagata et al. [76], and compared with data from Ganguli & Lele [28] at Re = 1 and Re = 10.



(a) Illustration of the slicing technique to determine (b) Averaged local Nusselt number as a function of the local Nusselt number $Nu_l(\theta)$ θ in comparison to Bagchi et al. [6]

Fig. 4.6: Uniform flow over a sphere at Re = 50 and $T_R \rightarrow 1$.

4.2.3 Conclusions

The comparisons of the results for the flow of heated and cooled spheres with data from the literature shows the high quality of the current numerical method. The reference results from the scientific literature are matched with good accuracy within a wide array of different configurations related to the topic of thermal dynamics. A grid convergence study determines the minimal solution that is necessary to obtain highly accurate results with minimizing computational efforts. Subsequently, a comparison of a fixed sphere with $T_R > 1$ to reference results from Kurose et al. [61], Nagata et al. [76], and Ganguli & Lele [28] shows the accuracy of the used algorithms by comparison of the Nusselt number Nu. Thus, the method can be used to thoroughly analyze the flow over ellipsoids for various Re, ϕ , β , and T_R as shown

in Ch. 6.1

4.3 Conjugate heat transfer

The conjugate heat transfer model presented in Ch. 3.6 is applied to generic test cases consisting of stationary and moving solid bodies in fluid flow to validate and show its wide application range. Different problems characterized by varying mechanisms are considered. First, a grid convergence study is conducted to investigate the accuracy of the proposed method and the impact of the cell size on the results. Then, the results of the coupling method and the one-dimensional analytical equation proposed by He & Oldfield [40] are compared. Results for a fixed spherical body in uniform flow are discussed with regard to the Nusselt number Nu and the results for the CHT for a backward-facing step flow are presented. Subsequently, the conservation properties of the method are asserted by a fixed and shape-transforming body in an adiabatic enclosure. Additionally, results for moving bodies are presented which demonstrate the accuracy and versatility of the developed method. Finally, the efficient implementation of the algorithm for usage on parallel computing systems is shown by scaling and benchmark plots.

4.3.1 Grid convergence study

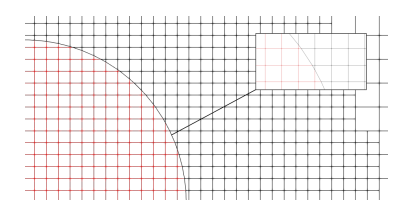
The impact of the mesh resolution on the simulation results of the conjugate heat transfer for a sphere in a uniform flow is discussed. The Reynolds number based on the sphere diameter is $Re_d=100$ and an initial Gaussian temperature distribution in the sphere is chosen, where the sphere interface line has a temperature ratio of $T_{R,\Gamma}=T_{\Gamma}/T_f=2.0$. The ratio of specific heats is $\gamma=1.4$ with Prandtl number Pr=0.72=const. The center of mass of the sphere with diameter d=1.0 is located at $0.0\times0.0\times0.0$ in a domain defined by $-15.0\times-15.0\times-15.0$ to $50.0\times15.0\times15.0$. The boundary conditions on the sphere surface are described in Ch. 3.6. For the fluid, freestream conditions are given for the velocity and density and the pressure is extrapolated from the flow field at the inlet and the lateral boundaries. On the outflow boundary, von Neumann boundary conditions are applied for the velocity and density, whereas the freestream value is prescribed for the pressure.

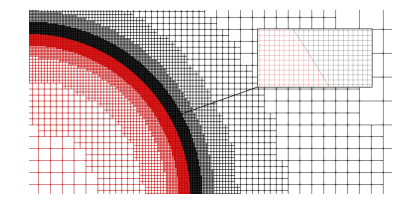
In the mesh convergence study, the maximum spatial step in the far field of the sphere is held constant, while the mesh around the sphere is progressively refined as specified in Tab. 4.3. The highest mesh refinement with a minimum cell length of $\Delta_{min}/d=0.0023$ is used to obtain a reference solution. In the finest mesh, approx. 448 cells are distributed over the diameter of the sphere.

Fig. 4.7 depicts the coarsest and the finest mesh used for the grid convergence study. The coarse mesh resolution l_1 is defined by a minimum cell length $\Delta_{min,l_1}/d = 0.0366$ and the fine mesh resolution by a maximum refinement level $\Delta_{min,l_5}/d = 0.0023$.

Parameter	Case l_i	Grid spacing Δ_{min}/d	Cells per diameter d/Δ_{min}
Max grid spacing		0.2929	
Min grid spacing	$egin{array}{c} l_1 \\ l_2 \\ l_3 \\ l_4 \\ l_5 \end{array}$	0.0366 0.0183 0.0092 0.0046 0.0023	28 56 112 224 448

Tab. 4.3: Mesh configurations in the grid convergence study.





- (a) Coarsest mesh l_1 in the grid convergence study with a minimum cell-width of $\Delta_{min,l_1}/d=0.0366$.
- (b) Finest mesh l_5 in the grid convergence study with a minimum cell-width of $\Delta_{min,l_5}/d=0.0023$ which defines the reference solution.

Fig. 4.7: Zoom of the region around the sphere for the coarsest (left) and finest (right) mesh used in the grid convergence study.

The surface temperature of the surfaces around $\phi=45^\circ$ is evaluated at a non-dimensional time $tu_\infty/d=33.3$. The semi-log plot of the error $(T_{l_i}-T_{l_5})/T_{l_5}$ is shown in Fig. 4.8.

The deviation decreases linearly in the semi-log plot. The distribution shows second-order accuracy. Since the overall accuracy of the discrete approximation of the spatial and temporal derivatives in the governing equations is of second order, the coupling approach proves to be at least second-order accurate. Therefore, it can be concluded that the presented surface coupling condition for the conjugate heat transfer is a consistent formulation which does not induce further inaccuracies.

4.3.2 Validation of the coupling formulation

In the following, generic test problems to validate the coupling formalism between the fluid and solid phases and to assess the accuracy of the approach are discussed.

4.3.2.1 One-dimensional steady heat conduction

For steady conduction in one-dimensional (1D) space, the surface temperature T_{Γ} at the interface is given by the analytical relation

$$T_{\Gamma} = \frac{T_s(k_s/\Delta x_s) + T_f(k_f/\Delta x_f)}{k_s/\Delta x_s + k_f/\Delta x_f}$$
(4.1)

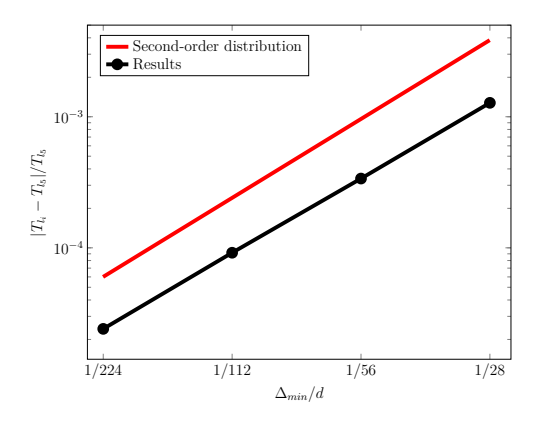
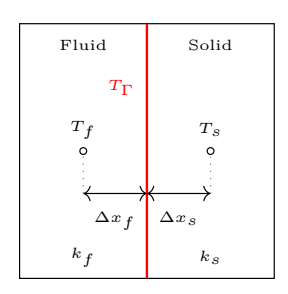
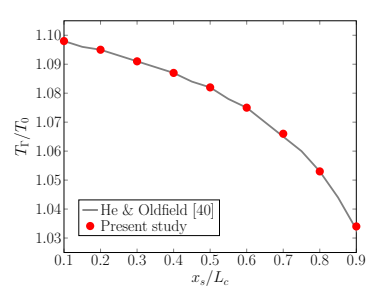


Fig. 4.8: Logarithmic plot of the relative deviation $|T_{l_i} - T_{l_5}|/T_{l_5}$ from a fine simulation at $\Delta_{min,l_5}/d = 1/448$. The red line indicates the theoretical minimum error corresponding to the second-order accuracy of the applied methods.

where Δx_s and Δx_f describe the mesh spacings [40]. The thermal state at the boundary interface can be analytically described by a harmonious average of the respective cell temperatures T_s and T_f , distances Δx_s and Δx_f , and thermal conductivities k_s and k_f (Fig. 4.9a).





- (a) Schematic illustration of the relation of the analytical equation by He & Oldfield [40]. The interface of the fluid domain with temperature T_f and the solid domain with T_s has the temperature T_Γ . The quantities Δx_f and Δx_s define the distances from the interface to the respective cell centers.
- (b) Comparison of the analytical solution Eq. 4.1 with the solution of the coupling method. The ratio of the surface temperature T_{Γ}/T_0 is shown as a function of the position of the cell interface x_S/L_c normalized by the cell length of an uncut cell L_C . Hence, $x_S/L_c=0.5$ means an even split of the cell volume.

Fig. 4.9: Schematic and results for the analytical equation derived by He & Oldfield [40].

The coupling method described in Ch. 3.6 is used to determine the surface temperature of an arbitrary single surface (Fig. 4.9a). The comparison with the analytical equation

in Fig. 4.9b shows the perfect agreement between the computed and the iteratively determined surface temperatures as a function of the surface-cell distance. The results for varying surface temperature ratios are precisely predicted and the mean deviation is well below 1%. Note that this accuracy is determined by the limit value defined for the iteration process. This indicates the proper derivation of the surface temperature. The results confirm that the iterative approach successfully determines the surface temperature with high accuracy for varying cut cell configurations.

4.3.2.2 Stationary isothermal sphere in uniform flow

Next, the case of a uniform flow over a stationary isothermal sphere is considered. That is, the temperature ratio between the sphere and the fluid is $T_R = T_s/T_f = 1.05$ and the heat capacity is $c_p \to \infty$ to allow the comparison to 0D configurations, i.e., the particle temperature is effectively isothermal. The Reynolds number of the freestream flow is $Re_d = 50$. The minimum mesh spacing is $\Delta_{min}/d = 0.018$ with local grid refinement which results in a total grid size of 4 million cells.

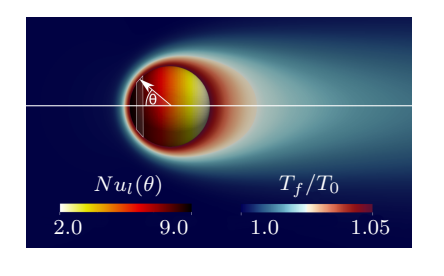
To evaluate the prediction accuracy of the resulting heat flux, the integral Nusselt number Nu

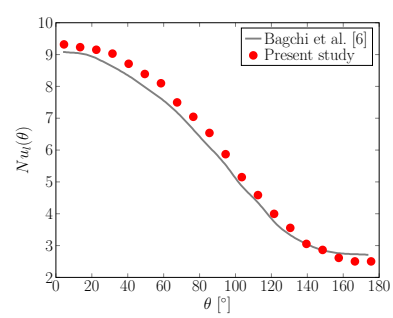
$$Nu = \frac{d}{k A \Delta T} \oint \mathbf{q}(\mathbf{x}) \cdot \mathbf{n} \, dA \tag{4.2}$$

is determined. The quantity d defines the sphere diameter, A is the surface of the sphere, $\oint \mathbf{q}(\mathbf{x}) \cdot \mathbf{n} \, dA$ is the integrated heat flux, and $\Delta T = T_s - T_f$ is the temperature difference between the solid and the fluid phase. A mesh resolution of $\Delta_{min}/d = 1/48$ is used which is based on the results in Kiwitt et al. [58].

In Fig. 4.10, the results for the local Nusselt number $Nu_l(\Theta)$ are compared with the findings in Bagchi et al. [6], in which the heat transfer from a sphere in a uniform flow was determined by direct numerical simulation at various Reynolds numbers. A visualization of the temperature distribution in the flow field and of the distribution of the local Nusselt number across the sphere surface is presented in Fig. 4.10a. The distribution of the local Nusselt number as a function of the angle θ is compared with the results from Bagchi et al. [6] in Fig. 4.10b. The agreement between both distributions is convincing, the maximum deviation for the local Nusselt number on the surface of the sphere is less than 4%. The heat flux, and thus, $Nu_l(\Theta)$, is highest at the front stagnation point of the body. Subsequently, the heat transfer reduces to a minimum at the rear of the sphere. The heat transfer is accurately captured by the present coupling method. Results for other parameter combinations of T_s/T_f and Re_{∞} , not presented in this paper, show similar agreement.

Furthermore, the data of the surface integrated and time-averaged Nusselt number are compared to the correlation equations from Whitaker [116], Kurose et al. [61], Nagata et al. [76], and Ganguli & Lele [28] since these correlations are often used in Lagrangian point-particle models. The results are summarized in Tab. 4.4. The flow parameters vary for the Reynolds number in the range of $1 \le Re \le 1000$ and for the temperature ratio. In all simulated configurations, the results match the findings published by the aforementioned authors. For the entire range of Reynolds numbers





- (a) Local Nusselt number $Nu_l(\Theta)$ on the surface and temperature distribution T_f/T_0 in the flow field.
- (b) Local Nusselt number $Nu_l(\Theta)$ as a function of the angle Θ . The results are averaged in slices from $0^\circ-180^\circ$ degrees.

Fig. 4.10: Isothermal sphere in uniform steady flow, comparison with findings from Bagchi et al. [6].

Kurose et al. [61]				Ganguli & Lele [28]				
Re = 50	Nu (Kurose)	Nu (present)	ΔNu		Re = 1	Nu (Ganguli)	Nu (present)	ΔNu
$T_R = 0.3$	11.5	12.0	4.2%	_	$T_R = 1.1$	2.21	2.24	1.34%
$T_R = 3.4$	2.8	2.9	3.4%		$T_R = 1.5$	2.06	2.09	1.43%
	•				$T_R = 2.0$	1.88	1.90	1.05%
Re = 100	Nu (Kurose)	Nu (present)	ΔNu		Re = 10	Nu (Ganguli)	Nu (present)	ΔNu
$T_R = 0.3$	14.9	15.7	5.09%		$T_R = 1.1$	3.17	3.21	1.25%
$T_R = 3.4$	3.3	3.2	3.13%		$T_R = 1.5$	2.95	3.01	1.99%
					$T_R = 2.0$	2.69	2.74	1.83%
							•	
Nagata et al. [76]				Whitaker [116]				
Re = 100	Nu (Nagata)	Nu (present)	ΔNu	μ	$/\mu_s = 1.1$	Nu (Whitaker)	Nu (present)	ΔNu
$T_R = 0.5$	11.8	12.1	2.48%		Re = 100	6.72	6.93	3.03%
$T_R = 0.9$	8.2	8.1	1.24%		Re = 200	8.88	9.11	2.53%
$T_R = 1.1$	5.5	5.5	0.4%		Re = 300	10.59	10.76	1.58%
$T_R = 1.5$	5.0	5.0	0.5%		Re = 500	13.36	13.49	0.96%
$T_R = 2.0$	4.3	4.2	2.4%	1	Re = 1000	18.65	19.01	1.89%

Tab. 4.4: Flow past a fixed isothermal sphere at several temperature ratios T_R compared with data from Kurose et al. [61] and Nagata et al. [76] at Re=50 and Re=100, compared with data from Ganguli & Lele [28] at Re=1 and Re=10, and compared to Whitaker [116] at various Reynolds numbers.

an average deviation below 5% is obtained. It can be concluded that the current coupling method yields accurate results for an isothermal body in steady flow for $T_R > 1$.

4.3.2.3 CHT for a backward-facing step

The backward-facing step (BFS) is as a generic configuration for separated flows. The separation is well defined, while the reattachment length is very susceptible. Such a flow field is often observed in engineering flow problems.

The flow forms a separation bubble behind the step, which reattaches further downstream. This reattachment considerably impacts the heat transfer, as evidenced by Chen et al. [18]. The recirculating flow and the reattachment are known to modulate the shear stress distributions and heat transfer rates in the fluid-solid interface [18, 19]. The simple geometry and the intricate flow physics make this problem an ideal benchmark case.

The current configuration corresponds to that of Ramšak [85], which is depicted in Fig. 4.11. The Reynolds number based on the step height H of the laminar inflow is $Re_H=800$ and the Prandtl number is Pr=0.71. The minimum mesh spacing is $\Delta_{min}/H=0.01$ with local grid refinement which results in a total grid size of 27 million cells.

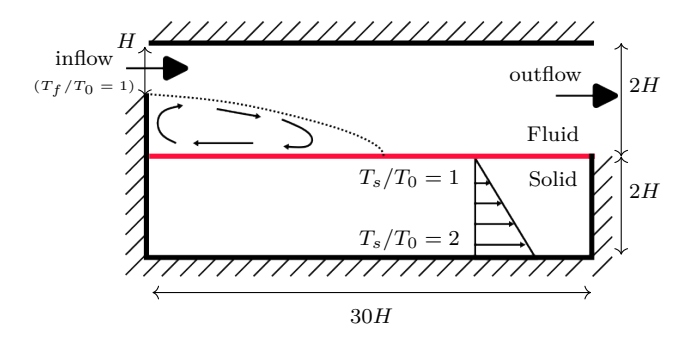


Fig. 4.11: Backward-facing step configuration from [85]. Its streamwise extent is 30H based on the step height H. The height of the solid domain is 2H.

Laminar inflow and outflow conditions are prescribed in the streamwise x-direction, in the spanwise z-direction periodic conditions are applied. Adiabatic boundary conditions are imposed on the top and vertical walls, while the bottom wall in the solid domain is isothermal. On the wall surface, defined by the red line in Fig. 4.11, the boundary conditions outlined in Ch. 3.6 are prescribed. Initially, the temperature distribution in the solid domain is set as linear function in the y-direction and set to $T_f = T_0$ in the fluid phase.

The simulation results for $0 \le x/H \le 20$ are visualized in Fig. 4.12 by temperature contours and streamlines. For the temperature ratio defined in this validation setup, the overall flow structure is only slightly influenced by the temperature distribution in the solid phase. The laminar separation bubble reattaches at approx. $x_c/H = 11.6$ which agrees well with the results of Ramšak [85].

In Fig. 4.13, the temperature distribution T/T_0 in the x-direction on the fluid-solid interface is shown. Note that the solution by Ramšak [85] is a 2D result, while in this study a 3D simulation is performed. Due to the vanishing gradients in the spanwise direction z, the results of the 2D and the 3D simulation are almost identical. Overall, the comparison shows good agreement. Along the fluid-solid interface, the

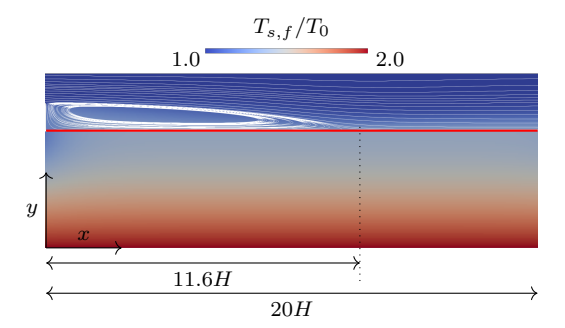


Fig. 4.12: Temperature field and streamline distribution for the backward-facing step case at $Re_H=800$. The bold red line indicates the interface between the fluid and the solid domain. The streamlines visualize the separation bubble and the reattachment point at x/H=11.6.

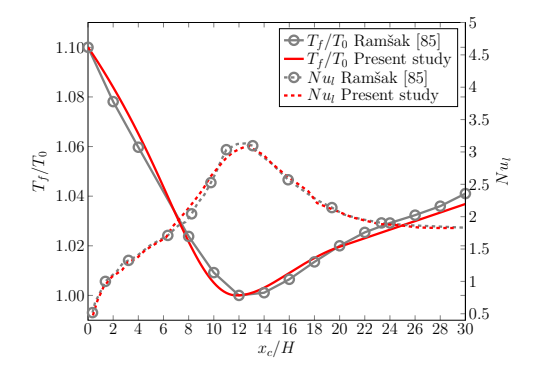


Fig. 4.13: Simulation of the CHT for a BFS setup. Comparison of results for the temperature and the Nusselt number distribution on the fluid-solid interface obtained with the present method with those from [85].

temperature distribution decreases until the minimum temperature $T/T_0 \approx 1$ is reached at $x_c/H \approx 12$ and then it increases until the end of the domain. The comparison with the flow field and the streamline distribution in Fig. 4.12 shows that the location of the temperature minimum roughly coincides with the reattachment location. This is also true for the peak Nusselt number as shown in Fig. 4.13. The results show that the presented method yields reliable results in generic setups for CHT in steady flows.

4.3.3 Energy conservation

In the following section, the conservation properties of the proposed method are validated. That is, the energy flux through the fluid-solid interface is verified. First, a fixed sphere in an adiabatic enclosure is validated. Then, the same setup for a shape-transforming body is investigated.

4.3.3.1 Fixed sphere in an adiabatic enclosure

The essential part of CHT in fluid-body interactions is the exchange of momentum and energy. To show that no energy is numerically dissipated by the coupling method, a reference case of a sphere of diameter d at a fixed position in an adiabatic environment is considered. The initial homogeneous temperature distribution is $T_R = T_s/T_0 = 1.2$ and the fluid domain possesses a zero velocity. The outer boundaries of the fluid domain are defined as adiabatic walls such that the combined energy of the fluid and solid domain should remain constant. The minimum mesh spacing is $\Delta_{min}/d = 0.018$ with local grid refinement which results in a total grid size of 7 million cells.

The energy variations within the fluid and solid phase are monitored during the simulation, i.e., the energy flux across the body interface and the individual changes in total energy in both domains are determined at each timestep. Since the solid domain loses energy due to cooling by the fluid, the fluid domain must receive this amount of energy due to heating. Checking the rate of total energy change allows the identification of unphysical energy sources or sinks, i.e., the assessment of whether energy conservation is satisfied.

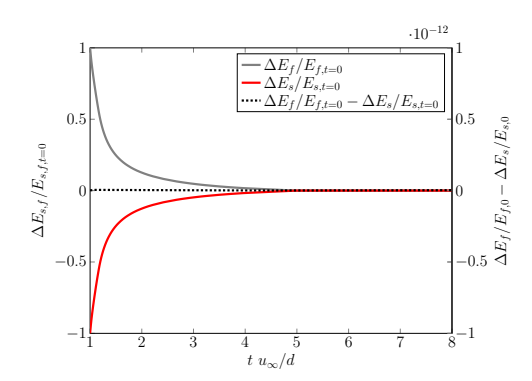


Fig. 4.14: Development of the total energy error in the fluid and solid normalized by the initial total energies $E_f(t=0)$ and $E_s(t=0)$ and the energy loss $\Delta E_f/E_f(t=0) - \Delta E_s/E_s(t=0)$ as a function of the non-dimensional time $t \ u_\infty/d$. The relative error $\Delta E_f/E_f(t=0) - \Delta E_s/E_s(t=0)$ is on the order of 10^{-14} , i.e., in machine precision range.

The total energy loss across both domains shown in Fig. 4.14 is approximately at machine precision level, i.e., the energy loss is negligible. This means that the total energy is conserved during the cooling and heating processes of the two phases since all energy is properly transferred over the interface. In brief, energy conservation is satisfied for this generic test problem.

4.3.3.2 Shape-transforming body in an adiabatic enclosure

Next, a fixed body undergoing a deformation of the shape in an adiabatic environment is considered. The setup is similar to that described in the previous section Ch. 4.3.3.1. Initially, the body has the shape of a sphere and slowly transforms into a prolate ellipsoidal body of aspect ratio $\beta=c/a=2$ and back into a sphere where $\beta=1$. The aspect ratio β is defined by the ratio of the major axis c and the minor axis a. The body volume is kept constant during the transformation based on the volume-equivalent diameter $d_{eq}=1$ such that the evaluation of the energy conservation is simplified. The minimum mesh spacing is $\Delta_{min}/d_{eq}=0.009$ with local grid refinement which results in a total grid size of 27 million cells. Note that the grid around the shape-transforming body is refined to the highest level such that the body remains in the highest refinement region during the shape transformation.

The energy exchange between the fluid and the body during the transformation is determined as in Ch. 4.3.3.1.

In Fig. 4.15, the shape transformation from the spherical to the ellipsoidal shape and back to the spherical shape is shown together with the temperature contours in the fluid domain as a function of time. The transformation of the body shape is done slowly to minimize the impact of the shape change on the temperature and the flow field.

All energy fluxes through the interface are tracked and contrasted with each other. The results in Fig. 4.16 show somewhat higher energy conservation errors on the order of 10^{-11} . Slight pressure and velocity fluctuations, and thus, energy modulations, on the interface cannot totally be avoided due to the changing body shape although the small cell correction technique [99] is used in the simulation. Overall, however, the results confirm that the coupling method does conserve energy in an extremely high accuracy range for slowly shape-varying bodies.

4.3.4 CHT for moving bodies

In the following, the proposed methodology is validated for a moving body case. A comparison between the moving and a reference non-moving configuration is used by switching the Eulerian and Lagrangian frame of reference.

The validation of the proposed method for the heat exchange in moving bodies presents a significant challenge. To the best of the authors' knowledge, there is no suitable CHT reference case that allows a detailed validation of the method, especially for moving bodies of arbitrary shape.

As previously stated, the method is based on an iterative approach that utilizes cell information, i.e., it is implicitly applicable to moving bodies. To validate this

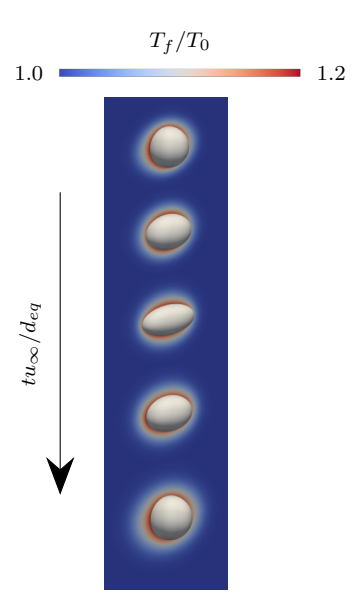


Fig. 4.15: Shape-transforming body in a domain with external adiabatic boundaries. The transformation process is shown. The body shape changes from spherical to ellipsoidal with an aspect ratio $\beta=2$ and back to spherical with an initial diameter d_0 . Furthermore, the temperature contours in the fluid domain are shown.

hypothesis, two configurations are examined. The first configuration is the case of a single ellipsoidal body at a fixed position in a flow defined by a freestream Reynolds number $Re_{\infty} = 100$ and a Mach number Ma = 0.1. The second case is defined by the body moving at $u_s = u_{\infty}$ through a flow field at rest such that Re_{∞} and Ma are again $Re_{\infty} = 100$ and Ma = 0.1. In other words, the Lagrangian and the Eulerian descriptions of the flow fields are compared.

The minimum mesh spacing is $\Delta_{min}/d_{eq} = 0.005$ with local grid refinement which results in a total grid size of 21 million cells. For the moving case, the locally refined grid moves with the particle.

The aspect ratio of the ellipsoid is $\beta=4$ and the inclination angle is $\phi_0=45^\circ$ as shown by the red grid in Fig. 4.17. The initial temperature ratio is $T_R=T_s/T_f=1.2$. This represents a challenging configuration for the thermal and mechanical predictions due to the high pressure gradients at the tips of the ellipsoid.

Fig. 4.18 shows contours of the temperature field for the moving and non-moving case. It can be seen that the flow field is virtually alike, indicating that the heat transfer dynamics is identically predicted independently of the movement of the body.

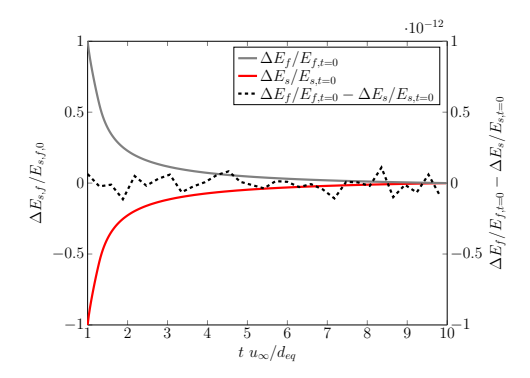


Fig. 4.16: Development of the total energy error in the fluid and solid normalized by the initial total energies $E_f(t=0)$ and $E_s(t=0)$ and the energy loss $\Delta E_f/E_f(t=0) - \Delta E_s/E_s(t=0)$ as a function of the non-dimensional time $t \, u_\infty/d$. The relative error $\Delta E_f/E_f(t=0) - \Delta E_s/E_s(t=0)$ is slightly higher than machine precision due to the relative movement of the surfaces during the shape transformation.

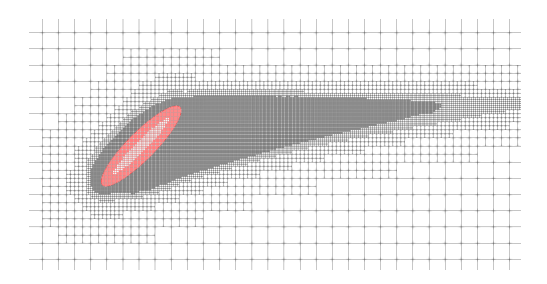
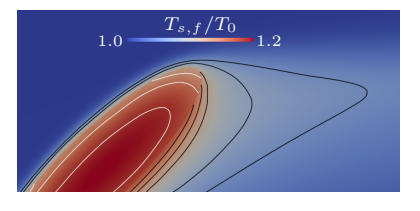


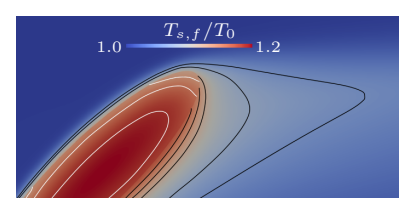
Fig. 4.17: Locally adapted grid around a body (red) at $\beta=4$ and $\phi_0=45^\circ$, and fluid (black). The local refinement is determined by the fluid temperature and the strain rate.



(a) Stationary ellipsoid with coupled boundary conditions in uniform flow.
(b) Moving ellipsoid with coupled boundary conditions in a quiescent flow field.

Fig. 4.18: Comparison of the temperature contours for an ellipsoid $\beta=4$ and $\phi=45^{\circ}$.





- in uniform flow.
- Temperature contours of a stationary ellipsoid (b) Temperature contours of a moving ellipsoid in a quiescent flow field.

Fig. 4.19: Comparison of the temperature contours for a stationary ellipsoid in uniform flow and a moving ellipsoid in a flow field at rest. The white contours describe the body temperature, whereas the black lines show the fluid temperature contours.

This is further supported by quantitatively analyzing the temperature distribution in the near-field in Fig. 4.19. The comparison of the temperature contours in close proximity to the ellipsoid shows no differences. The contours for T_f/T_0 and T_s/T_0 are virtually indistinguishable. Accumulating the individual cell values inside the contours yields a deviation of 2.7%. This is a highly accurate result, especially considering that an adaptively refined mesh is used for the moving ellipsoid.

A more detailed plot is shown in Fig. 4.20. The temperature along the centerline of the ellipsoid, i.e., from tip to tip through the center of mass, of an instantaneous time step is shown. It is evident that the differences are again on the order of machine zero. To highlight the small deviation, the difference between the two setups is shown by the black line. The little peaks are mainly due to the sudden changes in the mesh refinement for the moving body case.

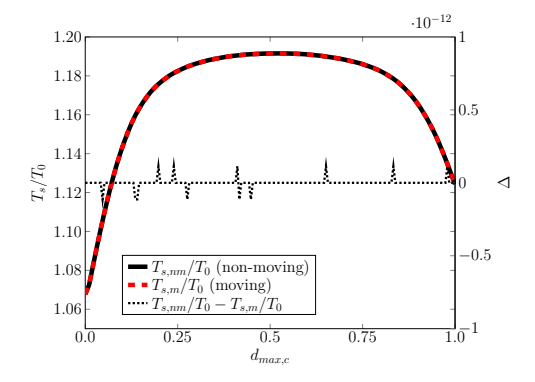


Fig. 4.20: Temperature distribution along the centerline of an ellipsoid from tip to tip passing through the center of mass.

The temporal development of the fluid temperature at the very top of the ellipsoid's

tip, i.e., at $\phi \approx 130^\circ$, is shown in Fig. 4.21 for the moving and the non-moving configuration. Note that the temperature is averaged over several cells between $126^\circ \le \phi \le 135^\circ$. The solutions for both cases are almost identical. The maximum deviation is less than 1%. This confirms the applicability of the coupled method for the moving case of arbitrarily shaped bodies. Therefore, it can be concluded that the numerical method produces valid results for stationary, deformable, and moving bodies.

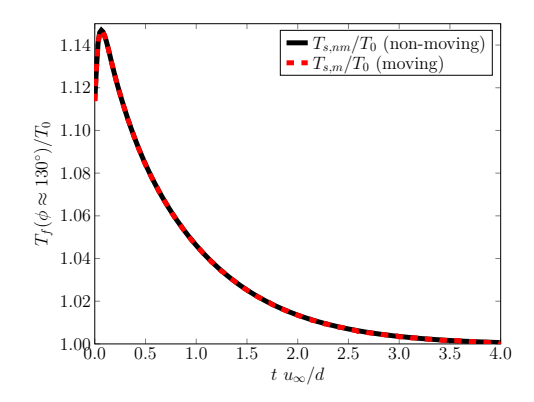


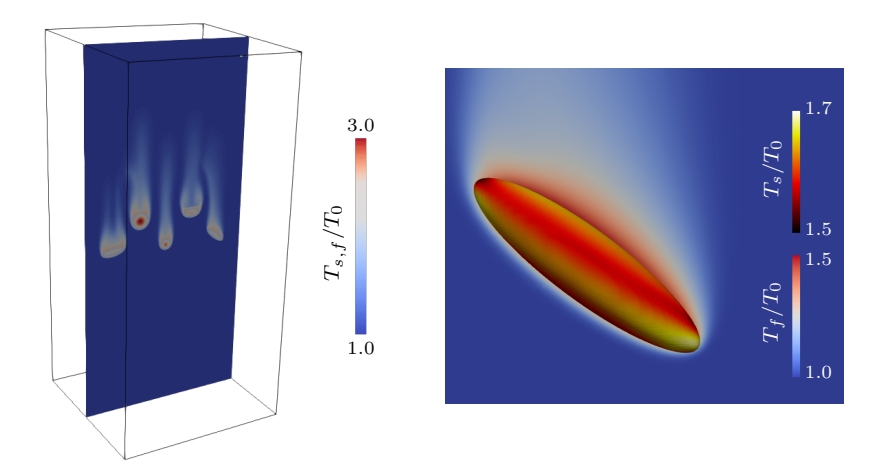
Fig. 4.21: Comparison of the fluid temperature at φ ≈ 130°, i.e., at the top ellipsoidal bodie's tip. The deviation between the line plot of the moving and the non-moving configuration is less than 1%.

4.3.5 Freely falling bodies

To further show the broad application range, the problem of 5 freely falling particles of various shapes, i.e., spherical, prolate, and oblate shape, in air is considered. To be more precise, the particles possess varying volumina with aspect ratios $\beta=4$, $\beta=1$, $\beta=0.25$, $\beta=0.5$, and $\beta=2$.

The configuration is such that the freestream Reynolds number encountered by the falling particles is $Re_{\infty}\approx 100$. The Prandtl number is Pr=0.72. The initial temperature distribution inside the particles possesses a Gaussian distribution where the highest temperature $T_s/T_0=3.5$ is located at the center of each particle, i.e., the temperature is lower on the surface compared to the body center. The initial temperature of the flow field is $T_f=T_0$. The minimum mesh spacing is $\Delta_{min}/de_q=0.004$ with local grid refinement which results in a total grid size of 197 million cells.

The illustration of the direct particle-fluid simulation in Fig. 4.22a The computation is based on a direct particle-fluid simulation which takes advantage of adaptive mesh refinement for each particle independently as shown in Fig. 4.17. The illustration in Fig. 4.22a indicates that the bodies tumble and rotate due to the aerodynamic



- (a) Cut plane showing contours of the temperature (b) CHT simulation for a freely falling particle in a field for five freely falling bodies of varying shape
 - fluid at initially rest and constant temperature. Shown are temperature contours in a cut plane through the fluid and solid.

Fig. 4.22: Freely falling particles of varying shape and aspect ratio in periodic quiescent flow.

forces acting on the bodies and the temporal development of T_s/T_0 differs between the various bodies. Due to the varying curvatures of the different body shapes, the motion of the bodies differs, which results in varying thermal gradients on the surface. The differences in the surface temperature distribution between the bodies are obvious. The strongly varying temperature distribution on the windward and the leeward side is evidenced in Fig. 4.22b for one of the ellipsoidal particles. In regions with a locally higher velocity close to the body surface, the heat transfer is larger resulting in a locally lower temperature. This emphasizes the necessity for accurate simulations when CHT for moving objects in a fluid flow is investigated. A detailed discussion of this topic, however, is beyond the scope of this study.

4.3.6 Parallel performance on HPC systems

The proposed coupling method is based on the joint Cartesian mesh approach which facilitates the direct exchange of the coupling information on the body surface. Unlike other solution approaches, e.g., in segregated solvers or overset meshes [5, 9, 10, 108], additional communication between solvers and mesh regeneration efforts, which are computationally expensive for large body displacements or setups containing a large number of bodies, are avoided.

The execution time for the simulation depends strongly on whether or not dynamic load balancing is used. Due to the moving bodies resolved with the solution adaptive mesh, the workload of the cells shifts through the subdomains, which causes an imbalanced workload. This is demonstrated in Fig. 4.23, where the wall-clock time per physical time step is plotted for two simulations using 128 nodes for the problem of five freely falling particles. In the direct particle-fluid simulation, the bodies of varying shape are resolved on a locally refined Cartesian mesh. The joint mesh has 197 million cells such that the minimum particle diameter is resolved by $d_{min}/h_{min}=54$ cells. The number of cells in the fluid domain is approx. 171 million and the solid domain is resolved by about 26 million cells.

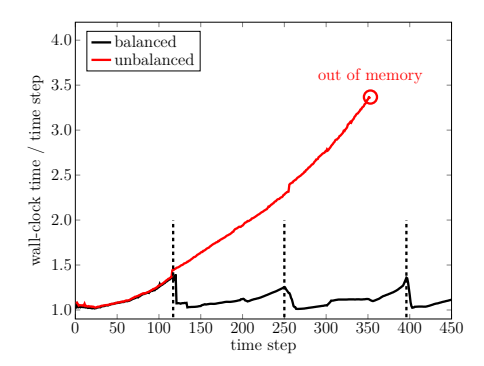


Fig. 4.23: Temporal development of the duration of a single time step for a balanced and unbalanced configuration of five freely falling particles. The dashed lines indicate load balancing events in the balanced configuration.

In the first simulation, dynamic load balancing is used which is switched off in the second simulation. Whereas the wall-clock time per time step is almost constant in the balanced simulation, the time increases monotonically in the unbalanced simulation until a single partition runs of out memory due to the creation of additional cells in the adaptive mesh refinement. The dynamic load balancing means only a small computational overhead, since the domain decompositioning based on a space filling curve can be performed by communication between neighboring subdomains such that no global repartitioning is required.

To demonstrate that a high parallel efficiency of the coupling method can be achieved, a strong scaling test is performed for the five freely falling body problem shown in Fig. 4.22a. The performance of the method including dynamic load balancing is evaluated using 16, 32, 64, and 128 nodes of the HPC system Hawk installed at HLRS Stuttgart. That is, only the number of CPU cores is varied. Each compute node is equipped with two AMD EPYC 7742 CPUs and 256 GB memory. Each CPU has 64 cores from which only every other CPU core is used by the simulation. The solver m-AIA uses a hybrid MPI and OpenMP parallelization, which is implemented using the parallel STL defined in the C++ standard 17. Fig. 4.24 shows the strong scaling results for the five freely falling bodies. The parallel efficiency remains high

with increasing number of nodes. The achieved speed-up in the strong scaling test is close to the ideal speed-up.

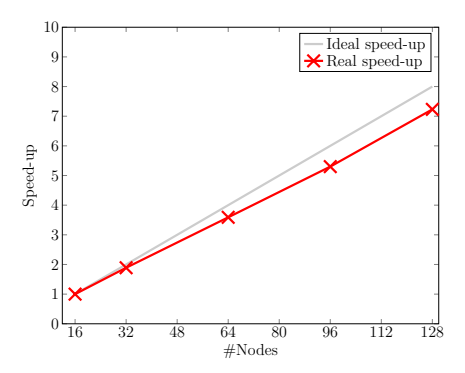


Fig. 4.24: Speed-up of the strong-scaling benchmark. The speed-up is in relation to the reference solution with 16 nodes at Hawk (HLRS Stuttgart).

4.3.7 Conclusions

An efficient numerical method to predict the thermal exchange by means of conjugate heat transfer between fluid and solid domains is presented. The algorithm uses an iterative conjugate heat transfer formulation at the interface, which ensures the conservation of mass, momentum, and energy. The method is applicable to fixed, moving, and deformable solid bodies of arbitrary shape.

The presented method demonstrates high accuracy across several test cases. Validation against an analytical solution for a generic body surface temperature shows excellent agreement. For heat transfer of a spherical body in uniform flow, local and averaged Nusselt numbers closely match literature values with deviations under 5%. The method accurately models dynamics in separating flow, as shown by the non-isothermal backward-facing step data. Energy conservation is verified by equilibrating a spherical body in a fluid at rest with adiabatic walls and for shape-transforming bodies.

Additionally, the applicability of the method to moving bodies of arbitrary shape is investigated by simulating moving and non-moving bodies in quiescent and uniform flow. Energy exchange results for five freely falling bodies with initial Gaussian temperature distributions highlight the need for precise methods to predict spatially varying temperatures in moving bodies.

The parallel efficiency of the method is demonstrated by a strong scaling test which is based on up to 8 192 compute cores. Additionally, the comparison of load balanced and unbalanced configurations shows the efficiency of the method in regard to performance and memory allocations.

The presented method relies on the usage of Cartesian hierarchical meshes. Since the accurate prediction of the heat transfer requires high mesh resolution at the surface, the method suffers from the limitation of the applicability of Cartesian meshes. In particular, the method may become expensive in the simulation of high Reynolds number flows. A wall function that predicts the heat transfer with a coarser mesh resolution at the surface could remedy this problem.

5 Particle-laden free jet flow

In the context of industrial combustion processes utilizing fine-scale fuels, solid particles are blown into a combustion chamber where they burn off in the presence of an oxidising atmosphere, in most cases air. A portion of the combustion air is injected alongside the fuel within the primary flow, resulting in a turbulent, two-phase free jet upon entry into the combustion chamber. In a first step, the combustion influence is neglected. That is, this numerical investigation focuses on analyzing the impact of non-spherical, ellipsoidal particles on the physics, i.e., the spreading rate, the kinetic energy, the dissipation rate etc., of non-heated turbulent free jet flow.

These dynamics will be addressed in this chapter by performing direct particle-fluid simulations for a non-spherical particle-laden turbulent free jet and comparing the multiphase jet flow data with single-phase turbulent free jet data for the same flow parameters. The direct comparison highlights the modulation impact of the particles. Energy and turbulence statistics are shown and the impact of the spherical and ellipsoidal particle characteristics are discussed.

An overall impression of the instantaneous flow field is shown in Fig. 5.1 in which the distribution of the particles and the development of the potential core, that is defined by the region near the centerline that has almost uniform mean velocity, and the free-shear layers are indicated.

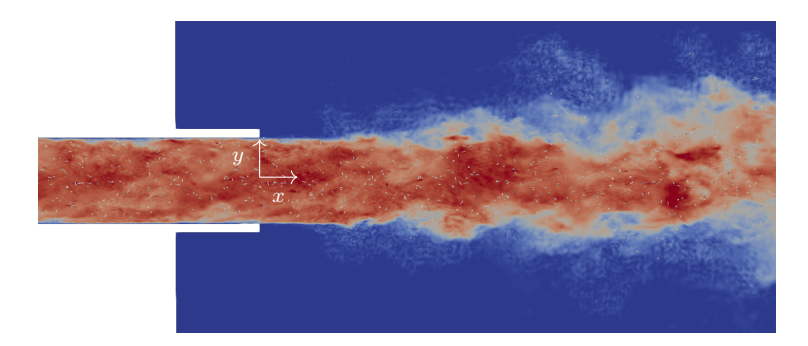


Fig. 5.1: Instantaneous absolute velocity contours for the particle-laden pipe and jet flow. Particles are shown in grey color.

5.1 Current research

There is a vast amount of literature on particle-laden flows for configurations like channel flow, pipe flow, and free jet flow. Since the current investigation is defined by the impact of non-spherical, ellipsoidal particles, only experimental and numerical studies of such non-spherical particle-laden flows are discussed in the following. To the best of the authors' knowledge, the number of journal publications in the field of non-spherical isothermal pipe or free jet flows is low. Scientific publications regarding pipe flow is included in the literature review since the pipe flow determines the inflow distribution of the turbulent free jet.

Black & McQuay [12] performed experiments in co-axial jet and swirling flows to assess the influence of the shapes of spherical and non-spherical particles on the particle dynamics. The two-component phase-Doppler particle analyzer technique was used to collect data for the particle velocities. The authors observed that non-spherical particles follow the fluid velocity much closer than the spherical particles. The essential reasons for these results are: First, the non-spherical particles show an increase in the drag coefficient which lowers the response time. The drag forces depend on the particle orientation such that the non-spherical particles tend to behave more like the gas phase. Finally, the terminal velocity of the non-spherical particles is lower than that of the spherical particles.

Ljus et al. [64] experimentally investigated spherical and pulp fibre particles with large aspect ratios in turbulent pipe flow. The Reynolds number based on the bulk velocity was in the range $82\,000-130\,000$ and the particle mass loading was 0.01-0.1. The measurements were conducted using a wedge-shaped hot-film probe with a static calibration method. The authors reported significant turbulence intensity modulation by the particles. The modulation impact depended on the particle diameter. Whereas spherical particles showed a modulation as a function of the radial position, the pulp fibres were shown to decrease the turbulence intensity over the entire cross sectional area.

Qi et al. [84] presented experimental measurements of fibrous particles with long aspect ratios in turbulent pipe-jet flow. The bulk velocity Reynolds number was 70 000 and the fibre aspect ratio was 40. Particle-tracking velocimetry was used to measure the particle characteristics. The results showed that the fibres possess a preferential orientation at 54° to the axial direction. However, the orientations covered a wide range from 30° to 90° . The absolute value of the mean angular velocity of the fibres increased with the radial distance from the axis centerline such that the lowest angular velocity was observed at the centerline of the jet.

Gupta et al. [35] numerically investigated the effect of the particle shape of prolate ellipsoids on the fluid statistics in particle-laden turbulent pipe flow at Reynolds number based on the friction velocity $Re_{\tau} \approx 250$ and volume loading $\zeta_v = 0.48\%$. The finite-sized particles with aspect ratios in the range of $\beta = 1$, $\beta = 2$, and $\beta = 3$ are compared to a single-phase reference solution. It was shown that the local accumulation of particles close to the wall decreases for ellipsoids with increasing aspect ratio due to slower rotation than the spheres near to the wall. The prolate particles tend to align with their major axes in the streamwise direction.

Guo et al. [33] used a model that accounts for spheroidal particle drag force and torque within an Eulerian-Lagrangian model to simulate pulverized biomass jets. The findings of particle and fluid velocities yielded large differences. It was also shown that the spheroid model led to a more dispersed distribution regarding the particle residence time and local concentration compared to the reference models.

The literature review shows that there are hardly any detailed results on non-spherical, ellipsoidal particle-laden turbulent free jets. That is, the impact of the shape of non-spherical, ellipsoidal particles on the orientation and the preferential distribution of the particles, the fluid kinetic energy, the jet geometry etc. are not discussed in the existing literature. These questions will be addressed in the following by performing direct particle-fluid simulations for a non-spherical particle-laden turbulent free jet and comparing the multiphase jet flow data with single-phase turbulent free jet data for the same flow parameters. The direct comparison highlights the modulation impact of the particles. Energy and turbulence statistics are shown and the impact of the spherical and ellipsoidal particle characteristics are discussed.

5.2 Domain of integration

A schematic of the pipe and the free jet domain is shown in Fig. 5.2. Both domains possess their own independent mesh resolution. However, the mesh in the crossflow section of the pipe is identical to that at the inflow boundary of the jet domain such that the solution in the pipe domain can be transferred at each time step without interpolation. The particles and all associated information are transferred accordingly. The slicing technique guarantees physically correct velocity distributions, particle positions and particle velocities as inflow conditions for the jet domain such that no assumptions regarding the turbulent flow state or particle dynamics have to be made [15].

The fully-developed turbulent pipe flow is simulated by a periodic boundary condition in streamwise direction where a volume forcing is applied to mimic a pressure gradient in the axial direction. While the free jet is coupled to the solution in the pipe flow, the solution in the pipe domain is independent from the solution in the free jet domain, i.e., one-directional coupling is applied.

On the outflow boundaries of the free jet domain the static pressure is prescribed. Von Neumann type boundary conditions are defined for the density and velocity. When particles enter or exit the domain, a special treatment around the particles is applied that is related to the adaptive mesh extension.

The boundary conditions on the particle surfaces are applied as described in Ch. 3.6 and as sketched in Fig. 3.16.

The pipe has a diameter D and a length L=6 D. This streamwise extent is based on the work of Chin et al. [21] in which the influence of the periodic pipe length on the turbulence statistics was investigated. The free jet domain consists of a box with a length of 50D in the streamwise and 15D in the radial direction. Note that the

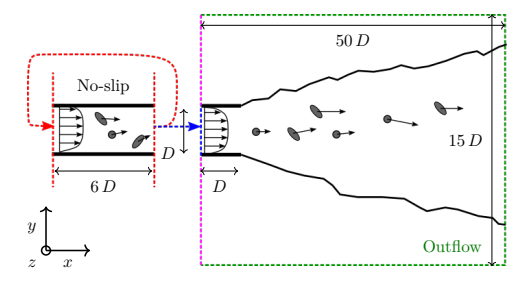


Fig. 5.2: Schematic illustration of the slicing technique to determine the inflow condition for the particle-laden jet. The simulations for the pipe and jet domains are conducted concurrently. A plane of the fully-developed pipe flow solution is transferred to the inflow boundary of the jet domain at each time step. The sketch also defines the domain sizes and imposed boundary conditions: periodic boundary conditions are implemented at the pipe in- and outlet, while outflow boundary conditions are defined on all other boundaries of the jet domain outside of the pipe. A no-slip isothermal wall boundary condition is used on the pipe wall.

pipe domain extends a length of one D into the jet domain as sketched in Fig. 5.2. There is no coflow around the free jet.

5.3 Flow and particle parameters

The Reynolds number based on the pipe diameter and the velocity at the jet inflow section is $Re_D = 15\,546$ and the Reynolds number computed with the friction velocity is $Re_{\tau} = 448$. The Mach number is M = 0.1 and the Prandtl number is Pr = 0.72.

The particles are initially placed at random locations within the pipe domain and the initial particle velocity equals the local fluid velocity. Random orientations of the particles are assumed. The particle aspect ratios cover the range $1 \le \beta \le 8$. The spectrum of the aspect ratio for the particles is uniform, i.e., equal amounts of particles (12.5%) for each of the 8 different aspect ratios are ensured. As stated before, all particles have the same volume based on the volume-equivalent diameter which is $d_{eq}/D = 0.01$. All particles have the same density ratio $\rho_p/\rho_f = 600$ which is relevant for biomass particles [34]. The particle Stokes number is $St_0 = 50$.

The volume loading in the pipe domain is approx. $\zeta_v = 6.67 \times 10^{-4}$ and the resulting mass loading is $\zeta_m \approx 0.4$. The number of particles in the pipe domain is 5 981. It remains constant due to the periodic boundary conditions for the pipe simulation. In the near field of the jet $x/D \leq 10$, the number of particles is approx. 10 000. It slightly varies since the number of particles entering is not necessarily identical to the number of particles exiting the jet domain. The particle parameters are summarized in Tab. 5.1.

Particle parameter	Value
Diameter d_{eq}/D	0.01
Aspect ratio β	1,2,3,4,5,6,7,8
Percentage of each β	12.5%
Density ratio ρ_p/ρ_f	600
Volume loading ζ_v	0.00667
Mass loading ζ_m	0.4
Stokes number St_0	50

Tab. 5.1: Particle parameters

5.4 Particle-laden turbulent pipe flow

The fully-developed pipe flow determines the instantaneous inflow for the free jet flow. Therefore, the flow dynamics of the fully-developed particle-laden pipe flow is investigated first. The spatial distribution and relative velocity between the particles and the fluid in the pipe flow are discussed and the energy exchange between the solid and fluid phase is analyzed with emphasis on the impact on the fluid dissipation.

The turbulent flow in the pipe is simulated concurrently with the flow in the jet domain. As stated before, one-way coupling is used such that the pipe flow solution is not influenced by the jet results. The particle dynamics are analyzed statistically and the interaction between the two phases is discussed.

5.4.1 Particle distribution

The dynamics of spherical and non-spherical particles differ. Due to their anisotropic shape, ellipsoidal particles show a concentration maximum at a position different from that of spherical particles inside turbulent pipe flow. The time-averaged particle distribution in the pipe is shown in Fig. 5.3 for spherical and ellipsoidal particles, i.e., for individual aspect ratios and the mean for all aspect ratios $\beta \geq 2$.

The general trend of ellipsoidal particles to accumulate closer to the pipe wall rather than in the pipe center is indicated. The results show an approximately linear increase in concentration with increasing pipe radius until a maximum is reached at $r/D \approx 0.32$. Spherical particles show a maximum concentration closer to the pipe wall at approx. $r/D \approx 0.4$.

The resulting particle concentration is related to the average residence time of the particles at a specific radial location, which is a function of the local radial velocity of the particles. Thus, the probability that a particle is located at a certain radius should be higher, where the radial velocity of the particles is smaller. In

Fig. 5.4, the absolute radial velocity
$$|u_R| = \left| \frac{yv + zw}{\sqrt{y^2 + z^2}} \right|$$
 normalized by u_b is shown

for $\beta = 1$, $\beta = 2$, $\beta = 4$, and $\beta = 8$ as a function of the radial coordinate r/D. The comparison of the radial velocity for the spherical and ellipsoidal particles shows that the magnitude of the velocity differs for the various aspect ratios. Whereas the curves follow a similar trend of increased velocities at the pipe center and pipe wall,

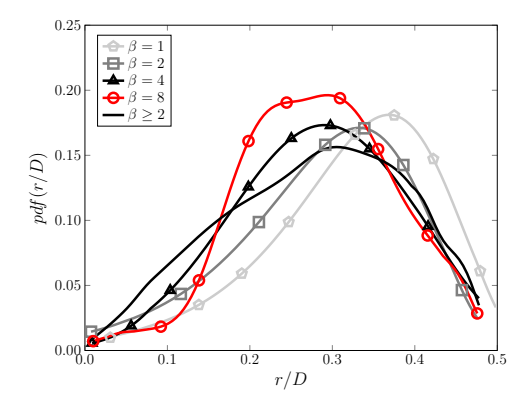


Fig. 5.3: Probability density function of particles with aspect ratio $\beta=1,\ \beta=2,\ \beta=4,$ and $\beta=8$. The solid black line, which represents the mean distribution of the ellipsoidal particles $\beta\geq 2$, shows a preferential distribution in the pipe domain at approx. $r/D\approx 0.32$. The statistics are computed for the full streamwise extent of the pipe domain.

the particles show larger radial velocities with increasing aspect ratio. Especially in the center of the pipe and near the pipe wall, the radial velocity increases with increasing aspect ratio, which leads to a lower probability that a particle will be present in this area.

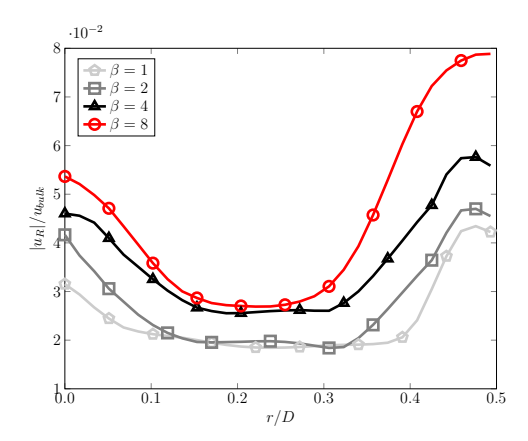


Fig. 5.4: Absolute radial velocity $|u_R|/u_b$ as a function of the radial position r/D. The preferential concentration at $r/D \approx 0.32$ by the particles is caused by the lower radial velocity between the pipe center and the wall.

Several phenomena are identified for the different dynamics of spherical and ellipsoidal particles. Due to the elongated shape, the ratio of the length of prolate particles in relation to the turbulent scales becomes larger than that of spherical particles. Therefore, the ellipsoidal particles experience larger differences in the inhomogeneous turbulent velocity field in the near-wall region. As a result, they are more likely to experience torque, which induces a rotation of the particle. The interaction of the rotating particle with the flow field eventually causes the particle to translate.

In addition, the turbulent velocity profile strengthens the motion of the particles within the domain through the localized loads on the particle surfaces. The spatially varying forces on the particle surfaces are induced by the local eddies such that additional torque and radial momentum are imposed on the surfaces of the particles. The high Stokes number $St_0=50$ means that the particles largely maintain their momentum. However, eventually the mechanical loads generated by the large-scale coherent structures in the flow field, i.e., the vertical structures are greater than the particle sizes, impact the particle trajectories. The relative mass distribution within the particles further influences this dynamic as the forces required to induce rotation are lower than those necessary to modulate the linear velocity.

In the following, a more detailed analysis of the impact of the particle aspect ratio β on the radial position within the turbulent pipe flow is conducted. The separate particle distributions for $\beta=2$, $\beta=4$, and $\beta=8$ are also shown in Fig. 5.3. The particle concentrations show the maximum values to shift towards the pipe center with increasing aspect ratio. The distributions of spherical and prolate ellipsoidal particles with aspect ratio $\beta=2$ exhibit a close resemblance. In contrast, the ellipsoidal shapes $\beta=2$ and $\beta=8$ possess distinctly different distributions. The distribution of the intermediate aspect ratio of $\beta=4$ lies between the two extremes. For increasing aspect ratio β , the maximum develops a plateau-like distribution which shifts progressively towards the center of the pipe. This behavior can be attributed to enhanced rotational dynamics among elongated particles as discussed before. This results in a more uniform distribution compared to that of spherical particles. Similar phenomena have been reported by Gupta et al. [35].

It is evident that the particle aspect ratio plays a crucial role in the radial particle distribution. The shift in distribution correlates to localized low radial velocity and increased rotational dynamics.

5.4.2 Linear velocity statistics

Previous research for spherical particles has shown that the ratio of the particle velocity and the local fluid velocity is a function of the radial position within turbulent pipe flow [83, 105].

To investigate this hypothesis for prolates, the time-averaged fluid velocity \overline{u} and the time-averaged particle velocities \overline{u}_p in the streamwise direction are shown in Fig. 5.5. The velocities for spherical particles are indicated by the subscript $(\cdot)_{p,s}$ and ellipsoidal particles are marked by the subscript $(\cdot)_{p,e}$. The distributions of the particle velocities \overline{u}_p normalized by the centerline velocity \overline{u}_{cl} in the pipe show that

the particle velocity is higher than the local fluid velocity near the pipe wall. The opposite is observed near the centerline.

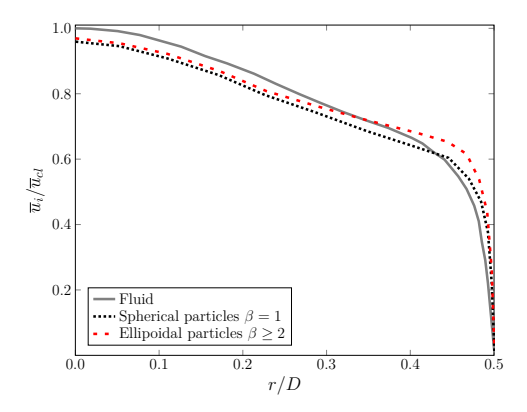


Fig. 5.5: Fluid velocity \overline{u} and velocities of spherical $\overline{u}_{p,s}$, and ellipsoidal $\overline{u}_{p,e}$ particles as a function of r/D. Near the centerline the particle velocities are smaller than the fluid velocity, while near the pipe wall the opposite is observed. On average, ellipsoidal particles are slightly faster than spherical particles due to the increased surface area exposed to the carrier flow.

Kaftori et al. [53] reported similar behavior for spherical particles. The authors concluded that the combination of rotational spin and linear movement resulted in increased particle velocities in relation to the local fluid [52, 53, 74]. This behavior is directly linked to the large Stokes number $St_0 = 50$ and the inertia resulting from it. For small Stokes numbers $St_0 \ll 1$, it is expected that the differences between the fluid velocity and the particle velocity will subside, i.e., the particles will align closely with the local fluid dynamics and act as tracer particles.

A comparison of the relative velocity distribution of the spherical particles and the ellipsoidal particles shows that the overall trend is very similar. The tendency of the particles to have a lower velocity than the fluid flow near the centerline is consistent with the behavior of spherical particles. The same is true near the pipe wall. Due to the equal mass of all particles irrespective of their aspect ratio, the particles have the same Stokes number St_0 and thus, show similar inertial behavior. Hence, the differences are mainly due to the particle shape. The ellipsoidal particles expose a larger surface area to the carrier fluid. Consequently, the ellipsoidal particles tend to experience larger mechanical loads on the windward side and maintain their inertia for a longer time. As a result, the velocity of the ellipsoidal particles near the pipe wall is greater than the spherical particle velocity.

5.4.3 Rotational statistics

The anisotropic shape of the ellipsoidal particles and the locally varying forces on the particle surface generate rotational forces which are less important for spherical particles. For ellipsoidal particles, this force distribution leads to rotational dynamics and eventually to linear movement due to interaction with the turbulent carrier fluid.

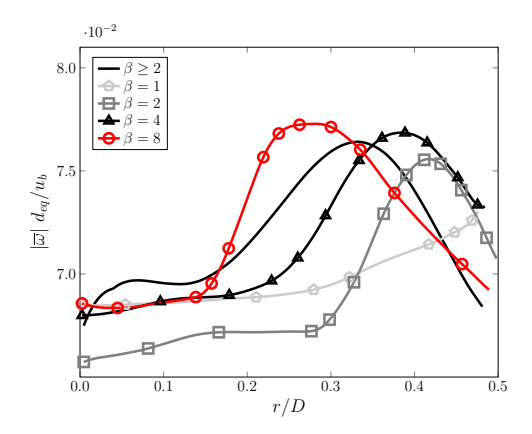


Fig. 5.6: Mean absolute angular velocity $|\overline{\omega}|$ d_{eq}/u_b as a function of r/D. The maximum angular velocity is observed at $r/D \approx 0.32$ which aligns well with the position where the particle velocities are aligned with the fluid velocity, i.e., small differences of the local fluid velocity yield the rotational dynamics.

To support this hypothesis, Fig. 5.6 shows the time-averaged absolute angular velocity $|\overline{\omega}| d_{eq}/u_b$ over r/D. The averaged vorticity rates peak at $r/D \approx 0.32$. This is in the range of the radial position where the ratio of the particle to the fluid velocity changes as shown in Fig. 5.5. The relative velocity at the particle tips of the ellipsoids is more likely of varying direction such that modulations on the surface have a comparably greater impact. This results in increased rotational dynamics due to the locally varying forces and velocities of the fluid.

The enhanced dynamics at $r/D \approx 0.32$ leads to a preferential orientation on average. The relative orientation of the ellipsoidal particles in relation to the streamwise axis is analyzed by the probability distribution function $pdf(\phi_x)$ illustrated in Fig. 5.7. Considering the illustration in Fig. 2.2, ϕ_x is the angle between the elongated particle major axis c and the fluid streamwise axis x. The results of the ellipsoidal particles indicate a preferential orientation of approx. 90° . Furthermore, two distinct peaks at $\phi_x = 55^\circ$ and $\phi_x = 125^\circ$, i.e., at approx. $\pm 35^\circ$ from the mean orientation of 90° are observed. The shear flow and the boundary layer on the pipe walls determine the loads on the particles. An inclination of the ellipsoidal particles of $90^\circ \pm \sim 35^\circ$ results from the pressure and velocity differences at the particle tips. Moreover, note the slight trend towards higher angles for increased aspect ratios.

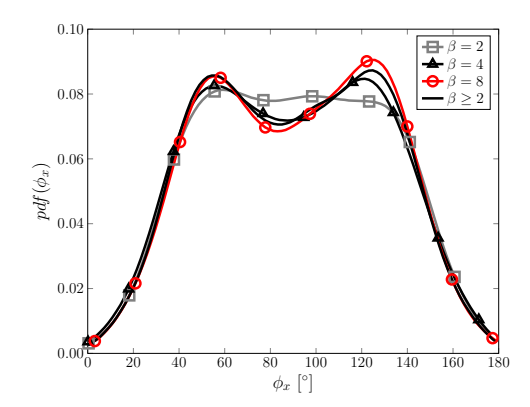


Fig. 5.7: Probability density function of the particle inclination angle $pdf(\phi_x)$. Except for $\beta=2$, two peaks are observed at $\phi_x=55^\circ$ and $\phi_x=125^\circ$, i.e., a deviation of $\pm 35^\circ$ from the perpendicular orientation. The statistics are computed for the full streamwise extent of the pipe domain.

This finding is in agreement with the results by van Wachem et al. [112] who reported an average value of approx. $60^{\circ} - 70^{\circ}$ for $\beta = 2.5$ for turbulent channel flow at $Re_{\tau} = 600$ when wall effects were incorporated.

The probability density function $pdf(r/D, \phi_x)$ as a function of the particle position r/D and the orientation ϕ_x in Fig. 5.8 evidences that the maxima at $\phi_x = 55^{\circ}$ and $\phi_x = 125^{\circ}$ primarily occur near the pipe wall where the ratio of the particle to the fluid velocity changes from > 1 to < 1 (see Fig. 5.5). Outside of these areas, the distribution is more random and uniform.

5.4.4 Multiphase energy exchange

Previous publications have shown a close relationship between the relative velocity ratio of the particle and the local fluid (u_p/u) and the energy exchange rates in multiphase setups [111, 122]. Furthermore, Zhao et al. [122] have shown that the energy exchange between the two phases due to the mean motion exceeds the exchange caused by the velocity fluctuations. To be more precise, the majority of the energy exchange is associated with the streamwise motions.

In Ch. 5.4.3 it was shown that the anisotropic ellipsoidal particles undergo additional rotation. It is stated in many publications such as [7, 16, 64, 81, 86, 109, 111, 122] that this additional rotation impacts the energy exchange. This is investigated in the following.

As shown in the last section, the velocity ratio $\overline{u}_p/\overline{u}$ differs with the relative position of the particles inside the pipe. This results in varying shear-stress and strain rates across the pipe diameter and altered fluid dissipation rates. The ellipsoidal particle

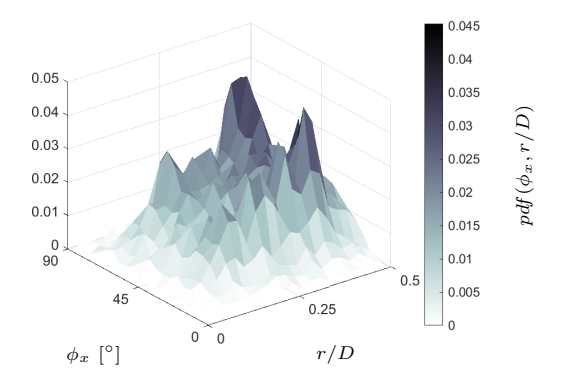
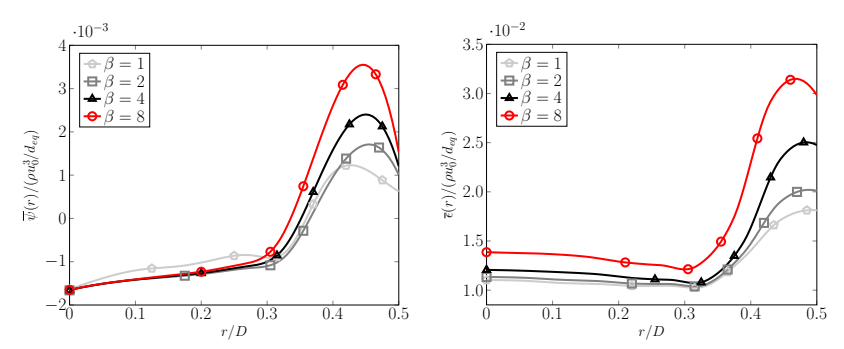


Fig. 5.8: Mutidimensional plot of the probability density function $pdf(r/D, \phi_x)$ for $\beta \geq 2$ as a function of the angle ϕ_x and the radial position r/D. The maxima at $\phi_x = 55^{\circ}$ and $\phi_x = 125^{\circ}$ primarily occur near the pipe wall.

shape additionally leads to a more complex dynamics in the particle wake due to entrainment, which further modulates the energy exchange.



(a) Mean interphase energy exchange $\overline{\psi}(r)$ normal- (b) Mean viscous dissipation rate $\overline{\epsilon}(r)$ normalized ized by $(\rho u_0^3/D)$.

Fig. 5.9: Comparison of the mean interphase energy exchange rate $\overline{\psi}$ (a) and the mean viscous dissipation rate $\overline{\epsilon}$ (b) for the investigated particle aspect ratios.

The dependence of the particle-fluid energy exchange on $\overline{u}_p/\overline{u}$ is investigated for spherical and ellipsoidal particles. Fig. 5.9a shows the time-averaged energy transfer $\overline{\psi}(r)/(\rho u_0^3/d_{eq})$ between the fluid and the particles as a function of r/D. The convention of $\psi \geq 0$ implies that energy is transferred from the particle to the fluid.

The energy transfer depends on the relative position inside the pipe. It is positive in the near-wall region and negative near the pipe center, i.e., energy is transferred from the particles to the fluid in the near-wall region for all aspect ratios. The particle transfer of energy is predominantly found near the pipe wall where the particle velocity is higher than the fluid velocity $u_p/u > 1$. This emphasizes the strong impact of the ratio of relative velocities and is attributed to the Stokes number St_0 .

Since the ellipsoidal particles on average are faster than the spherical particles near the wall, increased energy transfer rates are observed for ellipsoidal particles. Furthermore, larger aspect ratios yield higher transfer rates. Since all particles have the same mass, the surplus in energy transfer is caused by the differences in the relative velocities and the anisotropic shape which results in rotational dynamics yielding higher energy transfer rates. However, on average the momentum due to the rotation is one order of magnitude smaller than the momentum transferred by linear movement.

In contrast, the energy exchange near the pipe center is negative, i.e., energy is absorbed by the particles from the fluid. The ratio u_p/u is < 1 which facilitates the transfer of kinetic energy from the fluid to the particles. Since u_p/u is similar for different particle aspect ratios, comparable energy exchange rates are determined.

The particles additionally modulate the fluid dissipation due to the crossing-trajectory effect [97, 100]. With increasing $\overline{u}_p/\overline{u}$, the modulation is enhanced due to the increased shear stress on the particle surfaces. Additionally, the wake of the particles invokes fluid entrainment and thus, increased dissipation.

Fig. 5.9b shows by the local dissipation rate $\overline{\epsilon}(r)/(\rho u_0^3/d_{eq})$ over r/D that this assumption holds true for spherical and ellipsoidal particles. Qualitatively, the dissipation distribution behaves similar as the interphase energy transfer. The dissipation caused by the ellipsoidal particles is larger than for the spherical shape. This is especially true near the pipe wall where $\overline{u}_p/\overline{u}>1$, which results in larger relative velocities and thus dissipation rates. Furthermore, the particle tips of the ellipsoids generate localized pressure minima and steep velocity gradients which enhance the dissipation in the flow field.

In summary, the additional dissipation induced by ellipsoidal particles is greater than the energy transferred from the particle to the fluid. Near the pipe wall, energy is transferred towards the fluid and the fluid dissipation is significantly enhanced. Near the centerline, the energy transfer is negative and lower dissipation rates are observed. This is similar for spherical particles. However, a larger particle aspect ratio results in higher additional strain and dissipation.

5.5 Particle-laden turbulent free jet flow

The dynamics and the impact of the particles on the turbulent free jet flow are investigated next. The focus is on the near field $x/D \le 10$. The spatial dynamics

of the particles are presented and their impact on the flow structure are analyzed. Kinetic energy and turbulent intensity statistics are discussed.

5.5.1 Particle statistics

The near field of the turbulent free jet single-phase flow is characterized by the rapid development of the turbulent scales [15]. The initial instability modes trigger the development of the flow structures in the shear layer. The subsequent mixing results in vortices which will roll-up and stretch the vortices in the potential core [8].

The development of the flow field in the intermediate region $10 \le x/D \le 70$ is characterized by the highly anisotropic turbulent structures formed in the initial phase of the jet interacting with each other before reaching self-similarity in the far field $x/D \ge 70$.

The particles impact the flow development due to the particle-fluid energy exchange and local interphase and dissipation modulations as a function of the local position. In the following, the particle linear and rotational dynamics are discussed. Statistics equivalent to the analysis for the pipe flow evidence the impact of the different particle shapes on the turbulent free jet flow.

The probability density distribution pdf(r/D) of the particle positions of different shapes as a function of the radial position r/D at x/D = 10, i.e., at the end of the near field, is shown in Fig. 5.10. The overall shape of the particle distributions is quite similar for the different particle aspect ratios. However, the ellipsoidal particles show a slightly wider radial distribution in comparison to spherical particles and the spreading increases for larger β .

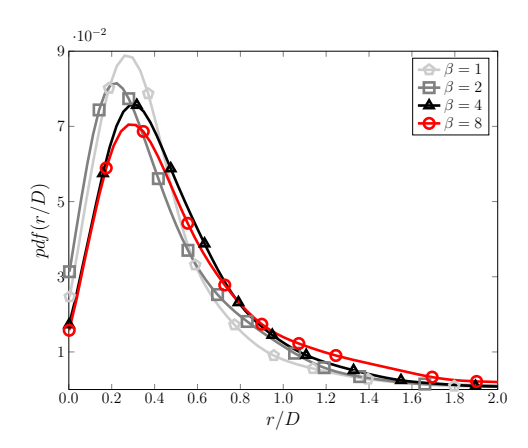
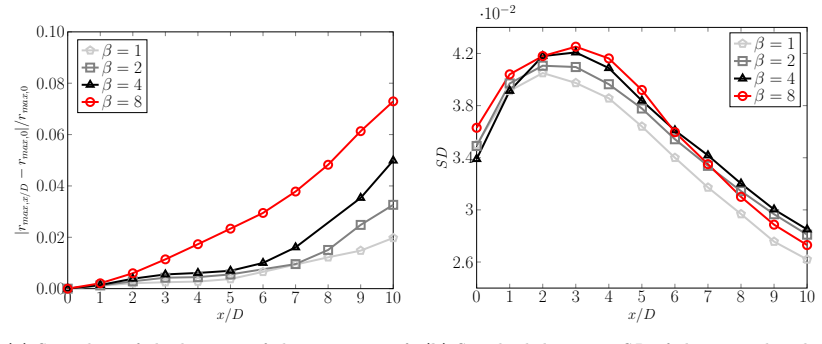


Fig. 5.10: Probability density function of particles with aspect ratio $\beta=1,\ \beta=2,\ \beta=4,$ and $\beta=8$ at x/D=10 in turbulent free jet flow.

When investigating the maximum of the probability density function, ellipsoidal particles of larger aspect ratios tend to align further away from the jet centerline.

The location of the maximum of the probability density function $r_{\max,x/D}$ is plotted in the streamwise direction x/D in Fig. 5.11a normalized by the location at the jet exit $r_{\max,0}$. It is evident that ellipsoidal particles spread faster in radial direction than spherical particles. While the maximum of the PDF for spherical particles ($\beta=1$) changes its location only marginally, ellipsoids with an aspect ratio $\beta=8$ show a three times higher spreading compared to $\beta=1$.



- (a) Spreading of the location of the maximum of the YDF $r_{max,x/D}$ normalized by its initial tions location $r_{max,0}$.
- (b) Standard deviation SD of the mean distributions as a function of the streamwise coordinate x/D.

Fig. 5.11: Particle spreading in turbulent free jet flow.

The standard deviation $SD = \sqrt{\frac{1}{N-1} \sum_{i=0}^{N} |pdf(r/D) - \psi_{mean}|_i^2}$ with the mean of the distribution ψ_{mean} at the respective distance x/D is shown in Fig. 5.11b for the different aspect ratios. The deviation from the mean increases for all aspect ratios in the streamwise direction x/D until $x/D \approx 3$. Further downstream, the standard deviation decreases which implies that particles tend to cluster closer together with increasing distances from the nozzle exit. It can be concluded that the aspect ratio of the particles has a large impact on their spreading rate in the turbulent free jet.

The higher spreading of the ellipsoidal particles in the turbulent free jet flow is correlated to their increased rotational dynamics. The probability density function $pdf(|\overline{\omega}|\ d_{eq}/u_b)$ of the absolute angular velocity $|\overline{\omega}|\ d_{eq}/u_b$ is shown at x/D=5 and x/D=10 in Fig. 5.12. The distributions show that ellipsoidal particles with an aspect ratio of $\beta=8$ possess higher angular velocities compared to particles with smaller aspect ratios. Further downstream at x/D=10, the angular velocity slightly increases for all aspect ratios in comparison to x/D=5.

Since the jet free shear layer merges towards the end of the potential core the particles are subject to larger scale fluctuations in the turbulent jet, which increases

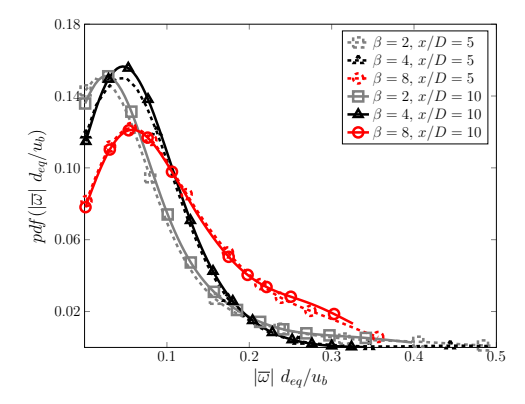


Fig. 5.12: Probability density function $pdf(|\overline{\omega}|\ d_{eq}/u_b)$ of the absolute angular velocity $|\overline{\omega}|\ d_{eq}/u_b$ for x/D=5 (dashed) and x/D=10 (solid).

the likelihood of varying surface forces around the particles such that the rotational dynamics is enhanced.

Fig. 5.13 shows the average orientation of all ellipsoidal particles $\beta \geq 2$ and the individual orientation of the $\beta = 2$, $\beta = 4$, and $\beta = 8$ at the end of the near field x/D = 10. The alignment with the streamwise axis is similar to the result in Fig. 5.7 for the pipe flow. However, the dip at $\phi_x \approx 90^\circ$ has disappeared. In other words,

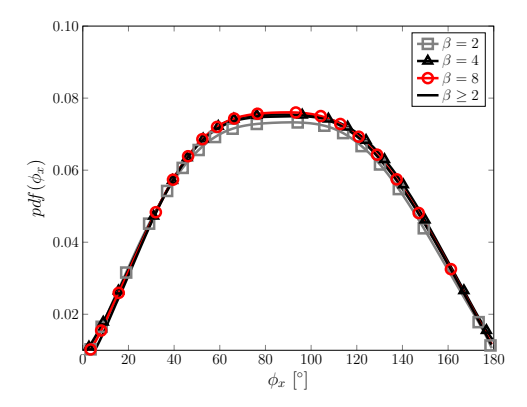
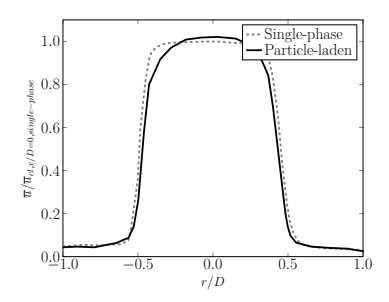
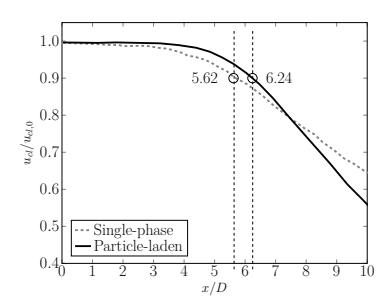


Fig. 5.13: Probability density function $pdf(\phi_x)$ of the particle orientation ϕ_x at x/D=10 for ellipsoidal particles.

the particles tend to align normal to the streamwise direction without any clear deviations. Compared to the pipe flow, the velocity gradients in the radial direction





- (a) Radial extension of the velocity $\overline{u/u}_{cl,x/D=0,single-phase}$ for the single-phase and particle-laden case at x/D=1.
- (b) Development of the velocity $\overline{u}_{cl}/\overline{u}_{cl,0}$ in the streamwise direction for the single-phase and the particle-laden flow.

Fig. 5.14: Impact of the presence of the spherical and non-spherical particles on the carrier fluid velocity in the turbulent free jet flow for the particle-laden and single-phase configuration.

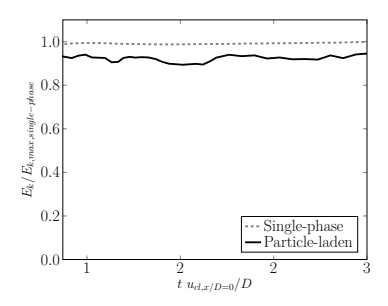
are reduced such that the forces on the particle surface are more evenly distributed. The ellipsoidal particles consequently tend to behave as bluff bodies. Similar results are reported by Fröhlich et al. [25] who investigated settling ellipsoids in isotropic decaying turbulence by means of Lagrangian point-particle models.

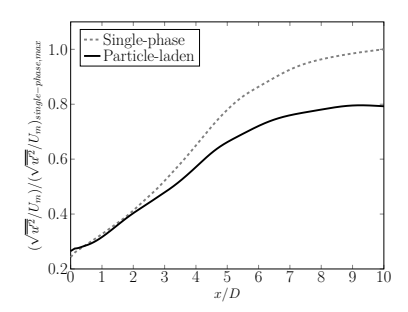
5.5.2 Jet structure

The flow structure of a free jet is characterized by the development of the free shear layer and the potential core. The velocity profile in Fig. 5.14a shows the single and multiphase solution in the potential core at x/D=1. The single-phase jet velocity profile is wider than that of the particle-laden jet whose radial extension is reduced by approx. 4%. The narrower extension is compensated by a slightly higher peak velocity on the centerline. Due to the small distance to the jet exit plane, it is clear that the distributions in Fig. 5.14a are strongly affected by the upstream pipe flow.

The particle-laden potential core has a higher mean velocity on its centerline. Due to the relative transfer of kinetic energy inside the potential core resulting from the spatially varying ratio of interphase energy exchange and increased dissipation rates, the shear layer of the jet is modulated. This means that the kinetic energy is more centralized to the core compared to the single-phase case. This results in lower velocity gradients in the radial direction which further impacts the energy decay rates. As a consequence of the altered core geometry, the length of the potential core is significantly increased. The length is defined by the position where the centerline velocity is less than 90% of its initial value, i.e., $x_{cl}(\overline{u}_{cl}/\overline{u}_{cl,0} = 0.9)$.

To counterbalance the elevated velocities on the centerline, Fig. 5.14b shows that the distribution of the centerline velocity of the particle-laden flow has a steeper decrease. The development of the dynamics in the turbulent free jet flow in the near





- (a) Temporal development of the normalized fluid kinetic energy of the single-phase and particleladen flow.
- (b) Streamwise development of the turbulence intensity $\sqrt{u'^2}/U_m$ normalized by the single-phase maximum turbulence intensity $(\sqrt{u'^2}/U_m)_{max}$ on the centerline for the single-phase and particle-laden jet.

Fig. 5.15: Impact of the presence of the spherical and non-spherical particles on the carrier fluid energy in the turbulent free jet flow for the particle-laden and single-phase configuration.

field $(0 \le x/D \le 10)$ develops like a sudden expansion. Due to the free-shear layers, turbulence further develops before reaching self-similarity further downstream.

Hence, Fig. 5.14b shows that the decay of fluid energy is greater at $x/D \geq 7$ for the particle-laden jet flow. The previously outlined tendency of the particles to increase the local fluid dissipation is related to the inertia forces of the particles. To be more precise, the inertia of the particles in the turbulent free jet decreases due to the spreading of the jet. Consequently, the fluid velocity is higher than the particle velocity which lowers the fluid kinetic energy. The tendency to break up coherent turbulent structures and enhance the transfer from the large-scale to the small-scale motions in the near field is well known [8, 15]. This is further intensified by the particles which facilitate the break-up process. This statement is further investigated in the following.

5.5.3 Fluid kinetic energy

The temporal development of the total kinetic energy of the fluid in the near field is shown in Fig. 5.15a for the single-phase jet and the particle-laden jet normalized by the maximum kinetic energy $E_{k,max,single-phase}$ of the single-phase flow. The kinetic energy is integrated in a volume $[0 \le x/D \le 10, -5 \le y \le 5, -5 \le z \le 5]$ and is normalized by the kinetic energy of the single-phase flow and the integrated volume, i.e., excluding the volume of the embedded particles.

The distribution of the single-phase jet possesses hardly any fluctuations. The kinetic energy reaches an almost steady value. The particle-laden jet fluctuates, it shows an unsteady distribution caused by the energy modulations of the carrier

flow imposed by the particles. The fluid kinetic energy in the particle-laden jet is reduced by approx. 9.1%. The kinetic energy distribution does not converge to a constant steady state value since the number of particles and their aspect ratios vary temporally in the jet volume.

5.5.4 Fluid turbulence intensity

The impact of different particle shapes on the turbulence intensity in fluid flow depends on various parameters [31, 64, 102, 109, 111].

To assess the impact of non-spherical particles on the intensity of the turbulent scales, the turbulence intensity $\sqrt{\overline{u'^2}}/U_m$ normalized by the single-phase maximum turbulence intensity is evaluated along the centerline. It is shown in Fig. 5.15b for the single-phase and the particle-laden jet.

Overall, the distributions follow a similar trend. Initially, the development of the turbulence intensity is indentical. At the nozzle exit, the initial instabilities generated by the free shear layer result in turbulent flow structures which convect downstream [8, 15]. Vortex roll-ups occur which enhance the spreading of the jet in the near field. This interaction breaks up coherent structures resulting in the development of the turbulent fluctuations in the later stages of the jet development [8, 15]. The tendency is enforced by the particles which are known to break up coherent large-scale motions [24]. The turbulence intensity of the particle-laden jet and the single-phase jet diverge at $x/D \geq 3$ where the particle-laden jet is severely damped.

The increased break-up of coherent structures and the higher dissipation due to the velocity differences between the carrier fluid and the particles cause the energy of the fluid to decrease and the turbulence intensity to be weakened. As shown before, the dissipation rate is impacted by the anisotropic particle shapes and the rotational dynamics. Therefore, the dissipation of the fluid is increased by the increased stress on the particle surfaces resulting in the steep drop off shown in Fig. 5.14b. At the end of the near field, the turbulence intensity is reduced by approx. 20%.

5.6 Conclusions

The impact of spherical and ellipsoidal particles on the overall flow structure in turbulent free jet flow is investigated. The particles possess aspect ratios in the range $1 \le \beta \le 8$. The simulations are performed using a cut-cell method in a finite volume formulation. The surfaces are described by a level set method. Using the multi-cut cell method, highly accurate results were achieved, conserving mass, momentum, and energy.

The turbulent free jet is computed simultaneously with a pipe flow. The latter provides the inflow data for the jet. This setup ensures physically correct particle and fluid properties at the jet inflow boundary.

The particle dynamics and flow characteristics of the fully-developed periodic pipe flow are investigated separately from the turbulent free jet flow. The particle distribution is assessed and the preferred orientation as a function of the varying particle aspect ratios is outlined. The results show preferential concentrations and orientations based on the particle aspect ratio and the relative position inside the pipe. For increasing aspect ratios, the distribution of the particles inside the pipe takes a more uniform distribution. Whereas spherical particles tend to align close to the pipe wall, ellipsoidal particles tend to align throughout the domain as the aspect ratio β increases. The major reason for the different distribution inside the pipe is the anisotropic particle shape, i.e., the elongated major axis. Due to the particle shape, rotational movement is induced that leads to increased spanwise dynamics. Preferential orientations of the ellipsoidal particles are identified at $\phi_x \approx 55^{\circ}$ and $\phi_x \approx 125^{\circ}$, i.e., $90^{\circ} \pm \sim 35^{\circ}$ where ϕ_x is the inclination angle against the streamwise direction. The almost perpendicular orientation is caused by the relative velocity and pressure differences at the particle tips of the anisotropic particles resulting in varying mechanical forces at the particle surfaces. The particles interact with the carrier fluid by transferring kinetic energy to and from the fluid. Depending on the relative position inside the pipe, all particles are shown to extract energy from the pipe center and to transfer energy to the fluid towards the pipe walls. This tendency is further amplified by the aspect ratio, i.e., a higher aspect ratio tends to increase the energy transfer. The particles are shown to additionally induce dissipation in the fluid. Similar trends as to the energy transfer are observed although varying in magnitude. The magnitude of the induced dissipation is on average larger than the energy transfer. This is shown to be caused by the additional rotational dynamics of the ellipsoidal particles and the relative velocity differences between the fluid and the particles.

Subsequently, the turbulent free jet flow is analyzed focusing on the near field region $x/D \leq 10$. The jet flow is modulated by the particles. That is, the jet radial extension is reduced by approx. 4% due to the particles. The velocity along the centerline has a steeper negative slope in the particle-laden jet since the particles induce additional dissipation. The comparison of the kinetic energy budgets between a single-phase and the particle-laden jet reveals an attenuation of the fluid kinetic energy by approx. 9% through the particles. The turbulence intensity is reduced by approx. 20%.

6 Heat transfer dynamics

In combustion processes, understanding heat transfer dynamics is crucial for optimizing energy efficiency, enhancing safety, and minimizing environmental impact. When fuels undergo chemical reactions to release energy, heat transfer dynamics play a significant role in fuel utilization efficiency and affect emissions, fluid dynamics, and overall system performance. Investigating the heat transfer mechanisms of non-spherical particles provides deeper insights into the behavior of these complex multiphase systems.

This chapter investigates non-isothermal multiphase flow. The focus will initially be on the study of ellipsoidal particles in a uniform flow. The data of more than 6 600 fully-resolved simulations in the parameter spaces Re, β , ϕ and T_R will be used to derive a correlation equation for the Nusselt number Nu.

The model for the calculation of fully-resolved particles, as presented in Ch. 3.6, is used for the investigation of heat transfer dynamics. By connecting the surfaces between the particle and the fluid, a physically correct and conservative energy exchange is ensured. As a result, thermal equalization processes between the particle and the fluid are reproduced with high accuracy. This method is used to investigate the accuracy of Lagrangian point-particle models. The configuration of a single ellipsoidal particle in uniform flow used for the correlation derivation in Ch. 6.1 is computed with fully resolving the thermal dynamics inside the particle. The flow field is discussed and the differences between the leeward and windward sides are specifically addressed.

Ultimately, this exploration will underscore the importance of effective heat management in achieving sustainable and efficient combustion technologies.

6.1 Correlation equation for the Nusselt number of ellipsoidal particles

Previous research has shown that the particle shape and the inclination of the particles have a major impact on the fluid-particle interaction [43, 50, 66, 93]. Recently, Fröhlich et al. [26] have shown a distinct relationship between the non-spherical particle dynamics and the Reynolds number, the inclination angle, and the aspect ratio. In a subsequent study, Fröhlich et al. [25] showed that ellipsoidal particles show a preferential orientation perpendicular to the settling direction impacting the particle velocity and thus, the particle dynamics. The impact on the heat transfer was not considered in either work.

Furthermore, work conducted by Kurose et al. [61] and Nagata et al. [76] showed that for a uniform flow past a sphere of surface temperature T_S and freestream fluid temperature T_∞ the temperature ratio $T_R = T_S/T_\infty$ severely impacts the Nusselt number. For a sphere $T_R < 1$ the Nusselt number increases, whereas for a sphere $T_R > 1$ Nu decreases. This is explained by the change in viscosity caused by the temperature modulation in the surrounding gaseous fluid. Recent work by Ganguli & Lele [28] shows that this behavior is also observed at low Reynolds numbers $Re \leq 10$.

To further emphasize the difference between the numerical results of the present study of an ellipsoid Nu_{sim} and the prediction based on the equation by Whitaker [116] Nu_{corr} for spheres at $T_R=1.05$ and $T_R=0.35$, the deviation $\Delta Nu=\left|\frac{Nu_{sim}-Nu_{corr}}{Nu_{corr}}\right|$ · 100 [%] is illustrated in Fig. 6.1 for the maximum deviation of an inclination range $0^{\circ} < \phi < 90^{\circ}$. Clearly, the correlation functions for spheres are insufficient to pre-

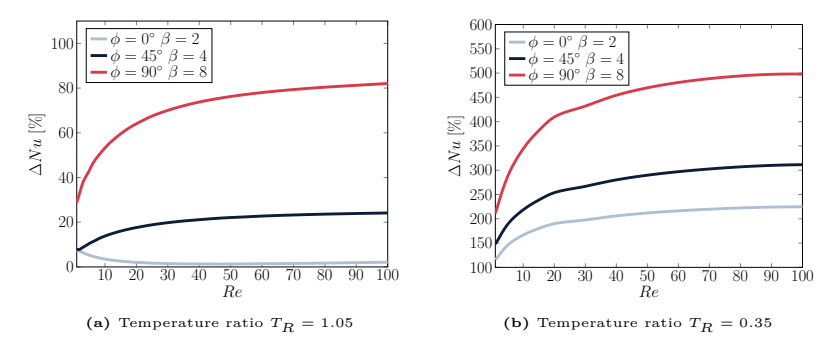


Fig. 6.1: Deviations of the correlation function by Whitaker [116] and the fully-resolved numerical results as a function of Reynolds number Re of prolate particles for varying inclination angle ϕ , aspect ratio β . and temperature ratios.

dict Nu for ellipsoidal particles, i.e., $\beta > 1$. The deviation increases up to over 80% with increasing aspect ratio for small temperature differences, i.e., $T_R = 1.05$. This deviation becomes even more pronounced for $T_R = 0.35$.

To the best of the authors' knowledge, there are no studies available in the literature in which the impact of the shape of the particle, the particle Reynolds number, the inclination angle, and the temperature ratio are analyzed and summarized in a correlation for the Nusselt number Nu. This, however, is necessary to perform efficient and accurate simulations of ellipsoidal particle-laden flows with a pronounced temperature difference between the particles and the carrier fluid as encountered in combustion chambers [3, 4, 49, 79].

To investigate the impact in regard to the heat transfer, direct numerical simulations are performed for a uniform flow over a single particle with a constant surface temperature. The data are used to analyze the essential physical phenomena characteristic for the present parameter space. The structures of the flow and temperature fields in the near-wall and the outer-flow regions are investigated to physically describe the impact of geometric, freestream, and heat transfer variations. Subsequently, the data from more than $6\,600$ simulations are used to derive a novel correlation function for the Nusselt number Nu that can be subsequently applied to conduct highly accurate point-particle computations.

6.1.1 Current research

The expressions most commonly used for the heat transfer are those by Ranz & Marshall [87] and Whitaker [116], or are based on these.

In early investigations, Frössling [27] developed a theoretical model for the evaporation of falling liquid droplets, combining molecular diffusion with convective effects caused by the droplets motion through air. The author derived a correlation equation that quantifies how convection enhances mass transfer, forming the basis for modern droplet evaporation theory.

Follow-up investigations regarding the impact of different flow parameters on the heat transfer of a spherical particle expressed by the Nusselt number Nu were published by Ranz & Marshall [87]. Based on measurements of water droplets in air in a Reynolds number range $Re_F \leq 200$, the authors proposed the equation

$$Nu = 2 + 0.6 Re_F^{1/2} Pr_F^{1/3}, (6.1)$$

with the subscript F representing the fluid properties being computed at film temperature $T_F = \frac{1}{2}(T_S + T_\infty)$.

Later, Whitaker [116] reviewed the available literature and proposed the equation

$$Nu = 2 + \left(0.4 Re^{\frac{1}{2}} + 0.06 Re^{\frac{2}{3}}\right) Pr^{0.4} \left(\frac{\mu_{\infty}}{\mu_{s}}\right)^{\frac{1}{4}}, \tag{6.2}$$

with the dynamic viscosity at freestream conditions μ_{∞} and the dynamic viscosity evaluated at surface temperature μ_s for a single sphere in freestream. The equation is valid for spheres in the parameter range $3.5 \le Re \le 7.6 \cdot 10^4$, $0.71 \le Pr \le 380$, and $1.0 \le \left(\frac{\mu_{\infty}}{\mu_s}\right) \le 3.2$ all determined at freestream conditions. This equation yields a maximum deviation of $\pm 30\%$ compared to experimental data.

The comparison of the solutions of the equations by Ranz & Marshall [87] and Whitaker [116] shows that the results can deviate by up to 10%. Several improvements have been presented in the last half century [23], i.e., the validity range and accuracy of the correlations have been improved. For instance, Wiskel et al. [118] increased the applicable temperature range of the formulation by Whitaker [116].

In contrast to the analysis of spherical particles, very few correlation expressions have been published for ellipsoidal particles. In general, these correlation functions are valid in a very limited parameter space. Richter & Nikrityuk [90] studied the heat and fluid flow past non-spherical particles, i.e., ellipsoidal and cubic particles, for varying inclination angles ϕ at the constant temperature ratio $T_R = 1.33$ and the

constant aspect ratio $\beta=2$. They presented correlation functions for the particle dynamics and the Nusselt number in the Reynolds number range $Re \leq 200$ and $0^{\circ} \leq \phi \leq 90^{\circ}$.

Ke et al. [55] investigated for a fixed ellipsoidal particle $T_R > 1$ the impact of the particle shape, the inclination angle, and the Reynolds number. Based on 125 simulations, the authors proposed a correlation for the parameter space $0.25 \le \beta \le 2.5$, $0^{\circ} \le \phi \le 90^{\circ}$, and $10 \le Re \le 200$. This parameter space partially overlaps with the current study and their correlation will therefore be used for comparison with the findings in this study.

6.1.2 Computational setup

The conservation equations Eq. 2.1 and Eq. 2.9 are discretized by a finite volume method using a locally-adapted hierarchical Cartesian mesh [39, 98]. The inviscid fluxes are solved by an upwind-biased scheme, the viscous fluxes are computed by a central scheme [11], and the temporal integration is performed by a predictor-corrector Runge-Kutta scheme [98]. The contour of the surface of the ellipsoid is described by a level-set function [37]. The surface is discretized by a cut-cell method in which intersected Cartesian cells are redefined according to the local boundary [98]. This ensures a strict conservation of mass, momentum, and energy of the multi-phase system.

At the inlet and the lateral boundaries, freestream conditions are given for the velocity and density, the pressure is extrapolated from the flow field (Fig. 6.2a, grey). On the outflow boundary (Fig. 6.2a, red), von Neumann boundary conditions are defined for the velocity and density, while for the pressure its freestream value is prescribed. A no-slip, isothermal condition is imposed on the surface of the ellipsoid.

The coordinate system (x, y, z) is fixed at the center of mass of the ellipsoid (Fig. 6.2b) which is located at $(0.25 L_x, 0.5 L_y, 0.5 L_z)$ in a domain defined by the streamwise (x), spanwise (y) and normal (z) lengths $L_x = 96 d_{eq}$, $L_y = 48 d_{eq}$, and $L_z = 48 d_{eq}$. It was shown in Ch. 4.2.1 that the minimum cell size $d_{eq}/\Delta_{min} = 48$ is a good compromise between computational cost and accuracy.

Adaptive mesh refinement [36] is used which is controlled by distinct threshold values based on the statistical distribution of given parameters around each sensor. Sensors are defined as local flow characteristics, i.e., strain rate gradient and the temperature gradient, determined throughout the domain (Fig. 6.2c). The local refinement is based on up to five refinement steps. Furthermore, the area surrounding the ellipsoid is refined based on a static, distance-based parameter to the highest refinement level. This ensures a proper resolution of all boundary layer phenomena on the surface of the ellipsoid. The adaptive mesh refinement is complemented by dynamic load-balancing [77].

The freestream velocity u_{∞} is determined by the Mach number Ma=0.1 and the particle Reynolds number Re varies in the range $1 \leq Re \leq 100$. The ratio of the surface temperature T_S and the freestream fluid temperature T_{∞} covers the interval $0.35 \leq T_R \leq 1.65$. The Prandtl number is Pr=0.72=const.

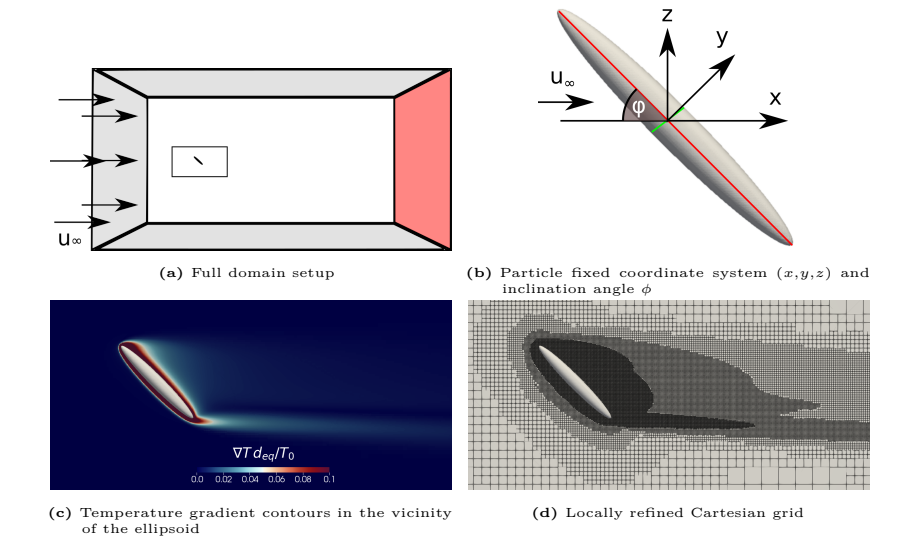


Fig. 6.2: Numerical setup of the flow configuration.

The inclination angle ϕ , i.e., the angle between the major axis of the ellipsoid and the freestream direction (Fig. 6.2b), is varied in the range $0^{\circ} \leq \phi \leq 90^{\circ}$. The aspect ratio β , defined by the ratio between the major- and minor axis, is varied between $1.5 \leq \beta \leq 8$, while the two minor axes are kept at a constant ratio of unity.

Note that the particle does not move, i.e., the location and orientation of the ellipsoid is fixed and buoyancy effects are neglected.

6.1.3 Fluid dynamics

In the following, the impact of the Reynolds number Re, the inclination angle ϕ , the aspect ratio β , and the temperature ratio T_R on the Nusselt number of a prolate ellipsoid in uniform flow is discussed. For $T_R=1.05$, the complete (red and black) parameter range of Re, ϕ , and β in Tab. 6.1 is analyzed, whereas for $T_R \neq 1.05$ only the red parameter combinations are investigated. In total, approx. 6 600 parameter combinations were considered.

To accurately separate the influence of each individual parameter, the flow and temperature fields are presented in Ch. 6.1.4. The discussion will focus on the interaction between the flow field and the heat transfer. First, the temperature ratio is considered $T_R = 1.05 = const.$ and the parameters, i.e., the Reynolds number, the inclination angle, and the aspect ratio, will be varied. Then, the temperature ratio and the lower limit of the studied Reynolds number range will be investigated.

Parameter	investigated range
Re	1, 2, 3, 4, 5, 6, 8, 10, 12, 15, 18, 20, 25, 30, 35, 40, 45, 50, 55, 60, 65, 70, 75, 80, 85, 90, 95, 100
β	$1.5, \frac{2}{2}, 3, \frac{4}{4}, 5, 6, \frac{7}{8}$
ϕ	0°, 5°, 10°, 15°, 20°, 25°, 30°, 35°, 40°, 45°, 50°, 55°, 60°, 65°, 70°, 75°, 80°, 85°, 90°
T_R	0.35, 0.55, 0.75, 0.95, 1.05, 1.25, 1.45, 1.65

Tab. 6.1: Investigated parameter space. Configurations of varying temperature gradients are considered, the Reynolds number is based on the volume-equivalent diameter d_{eq} and the aspect ratio $1.5 \le \beta \le 8$ is chosen to cover the most common aspect ratios in technical environments [78, 79].

In Ch. 6.1.5.2, the novel Nusselt number correlation equation is introduced and its accuracy and broad applicability range are discussed.

6.1.4 Flow and temperature field

To better understand the intricate flow structure that determines the Nusselt number distribution via the interaction with the surface, certain flow and structure features such as separation, reattachment, vortices, etc. are visualized. For conciseness, only selected configurations are discussed. First, the impact of the Reynolds number, i.e., the viscous forces, is considered, followed by geometric variations defined by the inclination angle and the aspect ratio. Then, the temperature ratio is changed and finally, the low end of the investigated Reynolds number range is discussed.

6.1.4.1 Impact of Reynolds number

To illustrate the impact of the Reynolds number on the heat transfer, the temperature contour lines for Re=1 and Re=100 are shown in Fig. 6.3 for $\phi=0^{\circ}$, $\beta=2$, and $T_R=1.05$.

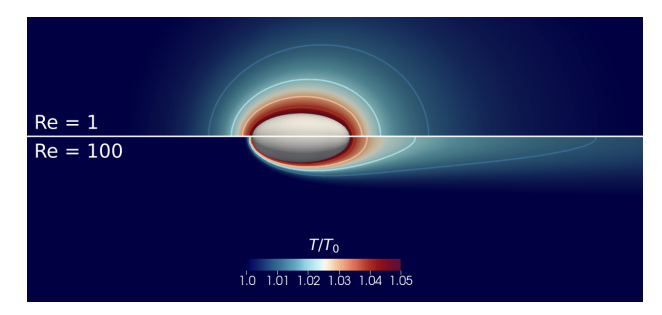


Fig. 6.3: Temperature distribution around an ellipsoidal particle at Re=1 (top) and Re=100 (bottom) for $\beta=2$, $\phi=0^{\circ}$, and $T_R=1.05$. The solid contour lines show the fluid temperature $T/T_0=[1.01,1.02,1.03,1.04]$.

The comparison evidences that at increasing Reynolds number the region of heat

transfer is compressed on the windward and stretched on the leeward side. This development is determined by the local velocity field and the trend is observed over the complete Reynolds number range.

Next, the impact of Re for varying inclination angle ϕ is discussed by analyzing the velocity and temperature fields, as well as the wall heat transfer for Re=10 and Re=90 shown in Fig. 6.4.

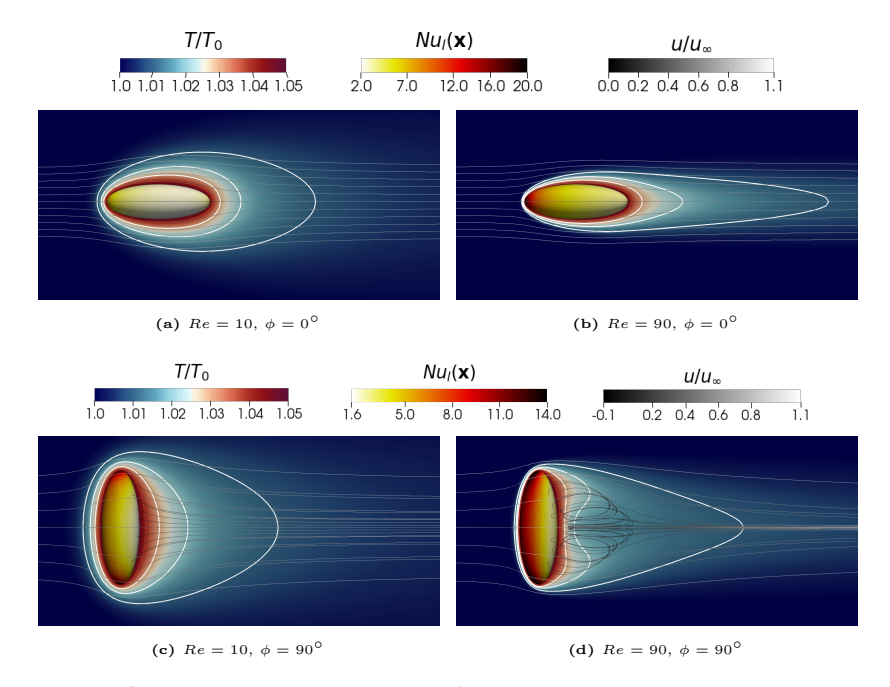


Fig. 6.4: Streamlines and temperature contours for Reynolds number Re = 10 and Re = 90 and inclination angle $\phi = 0^{\circ}$ and $\phi = 90^{\circ}$ at $\beta = 3$. Stream tracer particles are injected to highlight the flow topology in the wake of the ellipsoid. Furthermore, the Nusselt number distribution is shown. Note the different color scales for the local Nusselt number in (a,b) and (c,d).

For an ellipsoid with $\beta=3$ aligned in the streamwise direction, i.e., $\phi=0^\circ$ (Figs. 6.4a and 6.4b), the temperature contour lines are squeezed to the surface of the ellipsoid as Re increases. This observation agrees with the previous result that higher velocity gradients yield higher temperature gradients between the surface of the ellipsoid and the surrounding fluid. In other words, the heat transfer and thus, the Nusselt number, are increased. Furthermore, the difference in heat transfer between the windward and leeward stagnation point is amplified at higher Re as evidenced by

the stretched contour lines and an increased distribution of the local Nusselt number $Nu_l(\mathbf{x})$, which is defined by the local heat flux.

For a rotation of the ellipsoid about the y-axis by $\phi=90^\circ$, the flow field and the temperature field change drastically for Re=10 and Re=90. This varying susceptibility of the flow and temperature fields on the Reynolds number as a function of the inclination angle is primarily observed in the higher Reynolds Number range and for large inclination angles. At Re=10, the flow does not separate. Although there is a positive pressure gradient in the streamwise direction on the leeward side in the vicinity of the upper and lower tip of the ellipsoid, no flow detachment is observed. Only a slightly stretched wake region within the streamwise extent, which can be approximated by the major axis of the ellipsoids, characterizes the flow field and the temperature field. At Re=90 (Fig. 6.4d), however, the more pronounced positive pressure gradient near the upper and lower tip results in flow separation such that the leeward flow structure is determined by a massive vortex ring. This recirculating flow facilitates the removal of hot fluid from the leeward side leading to a higher heat transfer, i.e., an increasing Nusselt number. Note that this variation of the Nusselt number determined by ϕ is also true over the β regime.

6.1.4.2 Impact of inclination angle

Next, the impact of the orientation of the ellipsoid is analyzed.

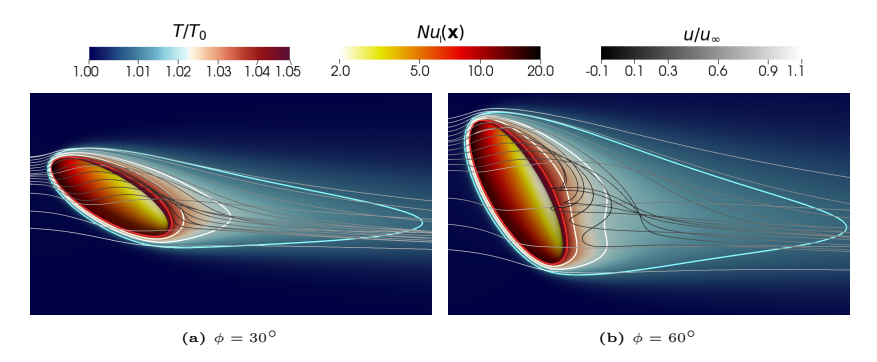


Fig. 6.5: Streamlines, temperature and Nusselt number contours for Re=90 and $\beta=3$ at varying inclination angles.

The streamlines, temperature, and Nusselt number contours are shown for two configurations $Re=90,\,\beta=3,\,\phi=30^\circ$ and $\phi=60^\circ$ in Fig. 6.5. While the former configuration is characterized by an attached flow, the latter is characterized by a detached flow. The varying flow structure is strongly determined by the distinct pressure gradients in the symmetry plane near the leeward tip of the ellipsoid.

Unlike the flow topology on the leeward side, the flow structure on the windward side is quite similar. It is characterized by the impingement of the uniform flow on the surface of the ellipsoid. This surface, which is exposed to the uniform flow, however, increases at higher inclination angles. For this reason, and the flow behavior on the leeward side, the mean Nusselt number Nu=7.50 for $\phi=60^\circ$ is higher by approx. 10% compared to Nu=6.98 for $\phi=30^\circ$. This result agrees with the findings by Richter & Nikrityuk [90] who reported an impact of the inclination angle of 7-12%.

The illustrations in Fig. 6.5a and Fig. 6.5b indicate that the peak value of the local Nusselt number $Nu_l(\mathbf{x})$ occurs at the tip of the ellipsoid independently from the inclination angle. The maximum value of the local Nusselt number $Nu_l(\mathbf{x})$, however, increases with decreasing inclination angles ϕ , i.e., the maximum value is observed at $\phi = 0^{\circ}$. This is attributed to the increased curvature of the ellipsoid relative to the freestream direction which enhances the velocity gradient at the tip at low inclination angles.

6.1.4.3 Impact of aspect ratio

The impact of the aspect ratio on the velocity, temperature and heat transfer field is illustrated in Fig. 6.6 for Re = 90 and $\phi = 45^{\circ}$ at $\beta = 2, 3, 6$, and 8. The overall flow structure does not change when $\beta \geq 3$, which was also observed by Fröhlich et al. [26].

However, unlike the flow topology, the mean Nusselt number strongly increases with higher aspect ratios, i.e., it almost linearly increases by $\sim 45\%$ from Nu=7.27 at $\beta=3$ to Nu=9.31 at $\beta=6$ and Nu=10.54 at $\beta=8$. Further analysis of the local Nusselt number $Nu_l(\mathbf{x})$ yields almost equal maximum values, i.e., $Nu_l(\mathbf{x})_{Max,\beta=6}=33.8$ and $Nu_l(\mathbf{x})_{Max,\beta=8}=33.9$. Consequently, it is the larger portion of the surface area which is exposed to relatively high local heat transfer rates which leads to an increased Nusselt number.

6.1.4.4 Impact of temperature ratio

The temperature fields for a flow at Re=100 over a particle at aspect ratio $\beta=8$ inclined by $\phi=90^\circ$ are shown in Fig. 6.7 for a temperature ratio $T_R=0.55$ (top) and a temperature ratio $T_R=1.45$ (bottom) ellipsoid. Two contour lines $T_a(\mathbf{x})=\frac{1}{2}(T_S+T_\infty)=T_F$ (white) and $T_b(\mathbf{x})=0.95\,T_\infty$ (black) are highlighted to emphasize the differences in the temperature fields of the particle-fluid temperature ratios.

The area confined by the contour lines T_a and T_b is somewhat larger for $T_R=1.45$ than for $T_R=0.55$. It is evident that the temperature ratio overall only slightly influences the extent of the particle surrounding temperature field. This result is due to the strong coupling between the temperature and the flow field. Especially the wake flow is defined by the separation on the leeward side which is primarily determined by the streamwise pressure gradient. Since the pressure variation hardly

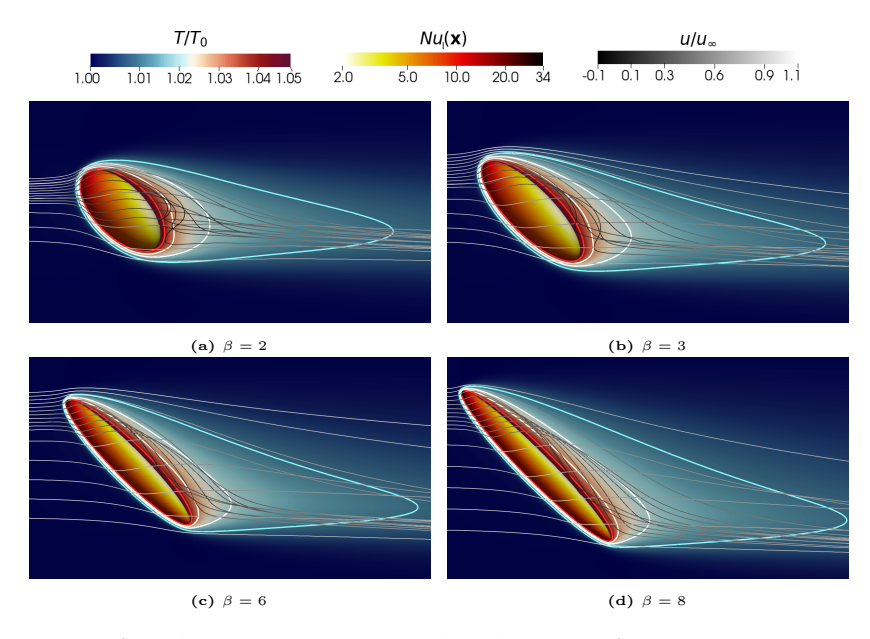


Fig. 6.6: Streamlines, temperature, and Nusselt number contours for various aspect ratios at Re=90 and $\phi=45^{\circ}$.

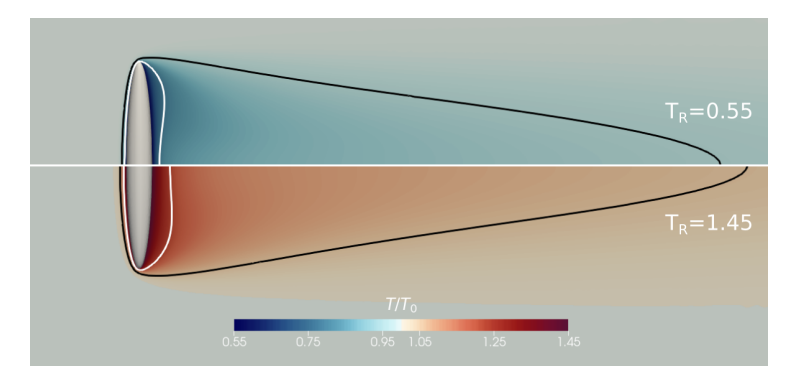


Fig. 6.7: Temperature and Nusselt number contours for a particle $T_R=0.55$ (top) and a particle $T_R=1.45$ (bottom) at Re=100, $\beta=8$, and $\phi=90^\circ$.

changes due to the constant Reynolds number the flow structure and thus, the temperature field, do not vary massively. This is in contrast to Kurose et al. [61]

who reported differing separation points. Note, however, that Kurose et al. [61] inspected spheres at higher Reynolds numbers, i.e., $50 \le Re \le 500$. In the Reynolds number range investigated in this study $1 \le Re \le 100$, the temperature ratio does not massively change the separation which is why the extent and the structure of the temperature field hardly varies.

The detailed analysis of the dynamic viscosity $\mu(T)$ surrounding the particle shows the link between the local dynamic viscosity $\mu(\mathbf{x})$ and the local fluid temperature $T(\mathbf{x})$ caused by the heat flux between the particle and the fluid flow (Fig. 6.8). For

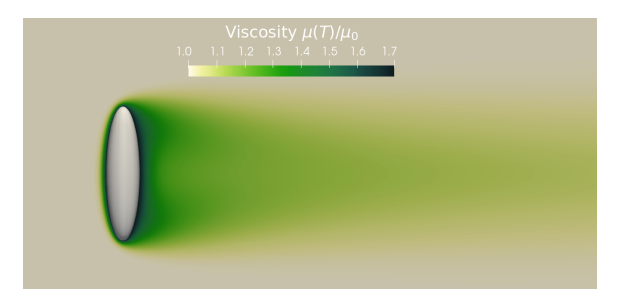


Fig. 6.8: Dynamic viscosity $\mu(T)/\mu_0$ of the fluid surrounding an ellipsoidal particle at $T_R=1.45$, $Re=100,\ \beta=4,$ and $\phi=90^{\circ}.$

 $T_R=1.45$, an increased local viscosity $\mu(\mathbf{x})$ is observed in the vicinity of the particle. This increased dynamic viscosity leads to a higher wall shear-stress $\tau_w=\mu\frac{\delta u_\parallel}{\delta n}$ with the wall-parallel velocity component u_\parallel and the wall-normal direction n. This reduces the fluid velocity near the wall and thus, the temperature gradient, yielding a lower heat flux and lower Nusselt number. The opposite result is true for $T_R<1$.

Note that the constancy of the Prandtl number also means $\mu(T)/\mu_0 = k(T)/k_0$ such that the contours are qualitatively alike.

6.1.4.5 Low Reynolds number limit

The equations by Ranz & Marshall [87] and Whitaker [116] are based on a lower limit of the Nusselt number obtained at creeping flow conditions, i.e., $Re \to 0$, of Nu=2. Since the temperature ratio impacts the temperature gradients directly, it is natural to assume different minimum Nusselt numbers at low Reynolds numbers as a function of the temperature ratio.

In the lower limit of the inspected Reynolds number range, i.e., $1 \le Re \le 10$, the inertial forces gradually vanish. The conductive mechanism becomes the dominant factor changing the dynamics of the heat transfer. Approaching Stokes flow conditions, different minimum Nusselt numbers are obtained depending on the particle shape. For spheres, the lower limit is $Nu \to 2$ for $Re \to 0$ and $T_R \to 1$ [28, 87, 116]. In contrast, values Nu < 2 for $Re \to 0$ at Pr = 0.7 for air are observed for prolate ellipsoids [68].

Since the impact of Re vanishes, a diminishing dependence of the heat transfer on the inclination angle ϕ is reached. That is, the dynamics is mostly governed by the geometry of the ellipsoid and the temperature gradients at the particle surface, to be more precise the shape determined by the aspect ratio β and the imposed temperature ratio T_R [120].

It is clear from the fully-resolved simulation data in Tab. 6.2 that the Nusselt numbers massively vary for the Reynolds number Re = 1 as a function of the temperature ratio T_R . The lowest Nusselt number at Re = 1 is obtained at the

$T_R < 1$	$Nu_{sim}(Re = 1)$	$T_R > 1$	$Nu_{sim}(Re = 1)$
0.35	4.98	1.05	2.34
0.55	3.48	1.25	2.06
0.75	2.91	1.45	1.89
0.95	2.51	1.65	1.75

Tab. 6.2: Smallest Nusselt number of all aspect ratios β at Re = 1 for several T_R .

highest temperature ratio $T_R = 1.65$. This trend is observed in the full range $1 \le Re \le 10$. To be more precise, for a particle $T_R < 1$ at Re = 1 the Nusselt number is Nu(Re = 1) > 2 and for a particle $T_R > 1$ the dimensionless wall heat transfer already reaches values Nu(Re = 1) < 2.

Next, the simulation data is used to present a correlation function for the Nusselt number in the considered parameter space.

6.1.5 Correlation equation

The parameter space is extremely large such that it is not straightforward to analytically derive an orientation dependent correlation function of the Nusselt number for ellipsoidal particles of different aspect ratios at various temperature ratios in uniform freestream flow. Therefore, a genetic programming approach is used to advance a symbolic regression tree to determine an accurate correlation function.

In the following, the regression method is briefly described and the novel correlation function is presented and discussed.

6.1.5.1 Regression method

A symbolic regression is a subgenre of regression analysis which constructs and searches for mathematical expressions that best describe a given dataset. To achieve this, the algorithm initializes a tree structure with randomly sampled functions and initializes them with arbitrary values.

Each generated expression is consecutively evaluated for its fitness and the tree is evolved accordingly in an iterative approach. Note that the term fitness represents the suitability of an expression to describe the dataset with regard to its accuracy and complexity. In general, each new generation has a higher fitness than the parent

generation, ultimately converging to a solution to describe a given dataset with almost arbitrary accuracy.

During the derivation of the proposed equation by the genetic programming algorithm, the full dataset is split into a training dataset and a validation dataset. The training dataset encompasses 90% of the full dataset, i.e., roughly 6 600 simulation results, while the validation dataset is comprised of the remaining 10%.

For further details, the reader is referred to the works by Zelinka et al. [121], Searson et al. [101], and Riolo et al. [91].

6.1.5.2 Novel correlation function

The discussion of the new correlation function for the Nusselt number determined by the regression method is split into two parts. First, the structure of the equation is analyzed and its accuracy is assessed. Subsequently, the results of the correlation function for the Nusselt number are compared with findings from the literature.

Structure and accuracy

The regression method derived the correlation function

$$Nu = 1.5 + \frac{0.5 - 0.05\sqrt{\beta^{-1}}}{T_R} + 0.37\frac{\sqrt{Re}}{T_R^{1.1}} + 0.1\frac{\sqrt{Re\,\beta^{sin(\phi)}\,\beta}}{T_R},\tag{6.3}$$

which was slightly adjusted to achieve a high accuracy at minimum complexity. That is, minor modifications were made, e.g., the coefficients were rounded slightly.

In the following, the physical meaning of the essential terms and their interactions are discussed.

For $Re \to 0$, the final two terms on the right-hand side vanish and the heat transfer is governed by the aspect ratio β and the temperature ratio T_R . The minimum Nusselt number reaches values Nu < 2 for $T_R > 1$ and Nu > 2 for $T_R < 1$. The discussion in Ch. 6.1.5.2 will show that the accuracy between the analytical solution for prolate spheroids [68] and the proposed equation at $Re \to 0$ is accurate within a maximum deviation < 10%.

Fig. 6.9 shows the Nusselt number Nu of an ellipsoid $\beta=2$, $\phi=0^{\circ}$, $T_R=0.55$ at Reynolds numbers $1 \leq Re \leq 10$. The simulation results are very accurately captured and the general trend of Nu is described very well.

The term $0.37 \frac{\sqrt{Re}}{T_R^{1.1}}$ accounts for the influence of the surrounding fluid on the convective heat transfer between the particle and the gas, with T_R reflecting the resulting temperature field due to the imposed heat flux.

The development of the Nusselt number as a function of the Reynolds number for different particle configurations are shown in Fig. 6.10. The distributions for the various configurations show a similar trend emphasizing that the qualitative behavior is dominated by the surrounding flow, characterized by the Reynolds

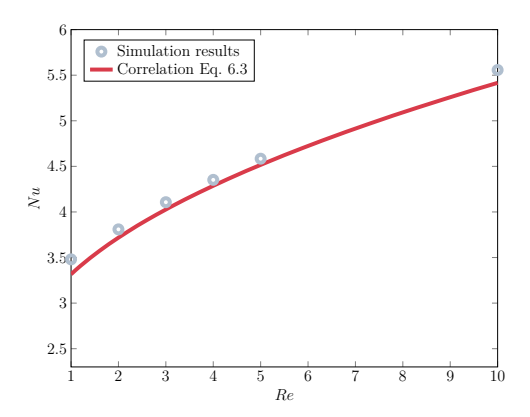


Fig. 6.9: Nusselt number Nu as a function of Reynolds number Re for an ellipsoid $\beta=2,\,\phi=0^{\circ},\,T_R=0.55$ at $Re\leq 10.$

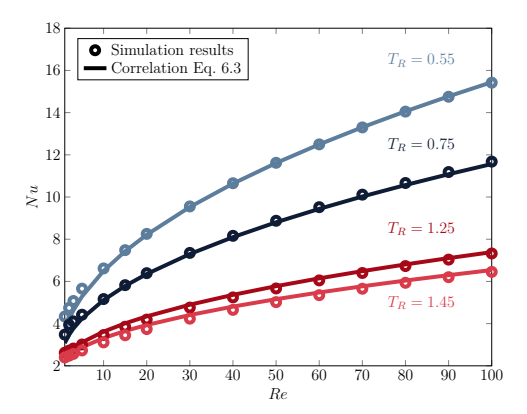


Fig. 6.10: Nusselt number Nu as a function of Reynolds number Re for several temperature ratios T_R at $\beta=4$ and $\phi=45^\circ$.

number. The slope increases moderately for decreasing T_R for particles $T_R > 1$, and more drastically for decreasing T_R for particles temperature ratios $T_R < 1$ due to the impact on the viscosity $\mu(T)$ and the thermal conductivity k(T) as discussed in Ch. 6.1.4.4.

Fig. 6.11 further highlights the high accuracy and versatility of Eq. 6.3 within the parameter space. Three configurations are shown in Fig. 6.11a for $T_R = 0.35$ and Fig. 6.11b for $T_R = 1.65$. The configurations are selected to show the accuracy in the extremes of the inspected parameter space, where the maximum deviations are

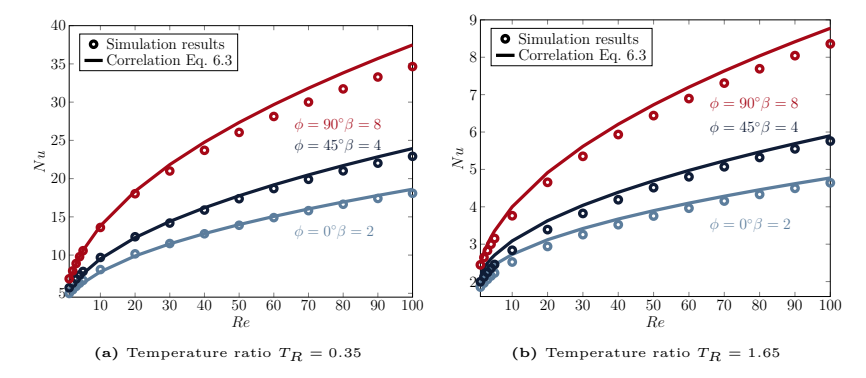


Fig. 6.11: Nusselt number Nu as a function of Reynolds number Re. Comparison of fully-resolved simulation and correlation data Eq. 6.3 for varying inclination angle ϕ and aspect ratio β .

found at high Reynolds number and high aspect ratio β in combination with high inclination angle ϕ .

The final term $0.1\,\frac{\sqrt{Re\,\beta^{sin(\phi)}\,\beta}}{T_R}$ models the relationship between the Reynolds number Re, the temperature ratio T_R , the inclination angle ϕ , and the aspect ratio β , i.e., the link between the shape and the orientation with respect to the surrounding flow is taken into account. Note that the inclination angle appears exclusively in combination with the aspect ratio. This ensures that the particle rotation does not falsify the results for a rotated sphere, i.e., $\beta=1$. Thus, Eq. 6.3 is also applicable to spheres.

The development of the Nusselt number for Re=80 is illustrated in Fig. 6.12 for $T_R=1.05$. The distributions show an S-curve shape, i.e., the plateau-like regions at low ($\phi \leq 10^{\circ}$) and high ($\phi \geq 80^{\circ}$) inclination angles are connected by the region with a pronounced slope in which the inflection point is located. The maximum slope increases for larger aspect ratios and is shifted to smaller inclination angles. That is, the overall sensitivity of the Nusselt number against β and ϕ grows.

Next, the dependence of Nu on β at Re=const. and $\phi=const.$ is discussed. It is shown in Fig. 6.13 that the Nusselt number increases almost linearly with the aspect ratio independent from the inclination angle and the Reynolds number. Additionally, the slope clearly grows at higher Reynolds number and higher inclination angle. To be more precise, the comparison of the Re=20 and Re=80 results for varying inclination angle ϕ evidences the pronounced impact of ϕ when changing from the low ϕ value to the mid ϕ value.

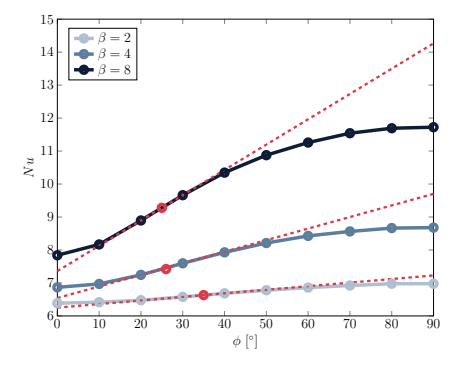


Fig. 6.12: Nusselt number Nu as a function of the inclination angle ϕ for varying aspect ratios β at Re=80 and $T_R=1.05$.

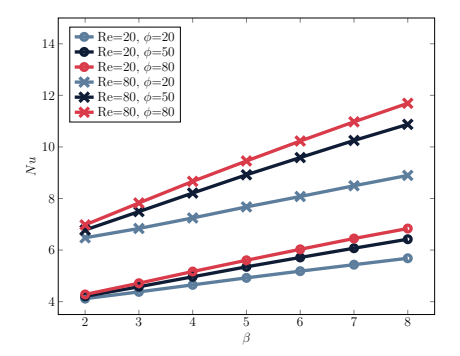


Fig. 6.13: Nusselt number Nu as a function of the aspect ratio β for various Re and ϕ configurations at $T_R=1.05$.

Sensitivity analysis

To further highlight the impact of the parameters on the Nusselt number, a sensitivity analysis is conducted. In the variance-based sensitivity analysis, the variance of the model output is split into individual fractions which are linked to the input parameters. The framework presented by Sobol [104] is applied in which the second-order indices quantify the impact of two coupled parameters on the output, i.e., the second-order indices quantify the variance of the output caused by the various combinations of the parameters. This analysis shows the impact of the meticulous amplification of the parameters, i.e., it reveals when the coupled impact is greater than the combined impact of each individual input parameter

Var(x, y) > Var(x) + Var(y).

Parameter	Second-order index	Percentage
$Re \phi$	0.014518	12.0%
Re eta	0.029160	24.2%
ReT_R	0.066108	54.7%
$\phi \beta$	0.003189	2.6%
ϕT_R	-0.007375	6.1%
βT_R	0.000405	0.4%

Tab. 6.3: Sensitivity analysis of the new Nu correlation function to quantify the impact of each input parameter.

The results in Tab. 6.3 emphasize the strong impact of the Reynolds number and the temperature ratio in Eq. 6.3. More than half of the variance in the output is attributed to the parameter combination ReT_R . The combinations $Re\beta$ and $Re\phi$ are also important due to the mechanisms discussed in Ch. 6.1.4, i.e., the larger area exposed to the increased heat transfer rates and the pressure gradient at the tip of the ellipsoid. The impact of $Re\phi$ shows to be similar to the impact described by Richter & Nikrityuk [90] which is 7-12%.

It was previously described by Fröhlich et al. [26] how the aspect ratio $\beta=3$ defines a turning point, i.e., the overall flow structure does not further change when $\beta\geq 3$. In Ch. 6.1.4.3, however, it was shown that the Nusselt number increases independent from the flow topology. To evidence the impact of the inclination angle ϕ and the aspect ratio β , the second-order indices are listed in Tab. 6.4 for two β -intervals.

$1 \le \beta \le 3$	Second-order index	Percentage	$4 \le \beta \le 8$	Second-order index	Percentage
$Re \phi$	0.011653	10.7%	$Re \phi$	0.021172	16.5%
$Re \beta$	0.016184	15.0%	$Re \beta$	0.021708	17.0%
$Re T_R$	0.073395	67.8%	$Re T_R$	0.072827	61.1%
$\phi \beta$	-0.000662	0.6%	$\phi \beta$	-0.001818	1.4%
ϕT_R	-0.003628	3.4%	ϕT_R	0.000015	0.1%
βT_R	0.002735	2.5%	βT_R	-0.005022	3.9%

Tab. 6.4: Second-order sensitivity analysis of the new Nu correlation function for the intervals $1 \le \beta \le 3$ and $4 \le \beta \le 8$.

The data show a varying impact of inclination angle ϕ and aspect ratio β implying that the inclination angle shows additional importance at high aspect ratios. Note that the impact of $Re \phi$ is 16.9% for $4 \le \beta \le 8$ even though the data in Tab. 6.4 includes small Reynolds numbers, i.e., a vanishing impact of ϕ as previously discussed.

Accuracy of the correlation equation

To assess the accuracy of Eq. 6.3, Tab. 6.5 shows the mean deviation $|\Delta Nu|$

 $\frac{1}{M}\sum_{i=1}^{M}|\Delta Nu_i|$ between the numerical results and the correlation results for several

temperature ratios T_R . The deviations are calculated for the complete parameter space, i.e., the deviations for each T_R are determined based on the full Re, ϕ , and β parameter space. The mean deviation $\overline{|\Delta Nu|}$ over the full investigated parameter

$T_R < 1$	$\overline{ \Delta Nu }$	$ \Delta Nu_{Max} $	$T_R > 1$	$ \Delta Nu $	$ \Delta Nu_{Max} $
$T_R = 0.35$	4.11%	15.76%	$T_R = 1.05$	4.54%	16.64%
$T_R = 0.55$	1.70%	16.89%	$T_R = 1.25$	2.08%	13.44%
$T_R = 0.75$	1.79%	17.06%	$T_R = 1.45$	2.51%	12.61%
$T_R = 0.95$	3.21%	17.37%	$T_R = 1.65$	4.69%	16.73%
$T_R < 1$	2.70%	17.37%	$T_R > 1$	3.45%	16.73%

Tab. 6.5: Mean and maximum deviations between the numerical and the prediction results for several T_R .

range is approx. 3% with a maximum deviation below 18%.

The distribution of ΔNu in Fig. 6.14 further shows the majority of all deviations of Nu to be less than |5%|. To be more precise, 36.8% of all deviations are $\leq |3|\%$, 66.9% are $\leq |5|\%$, and 93.9% are $\leq |10|\%$. The Gaussian distribution possesses a peak value at $\sim 3\%$ deviation. This slight shift is attributed to the minor rounding of the coefficients mentioned at the beginning of this section.

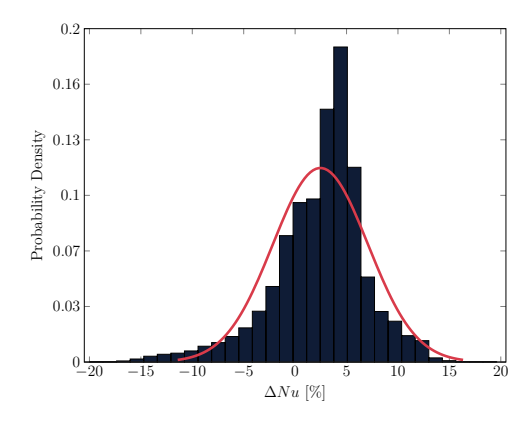
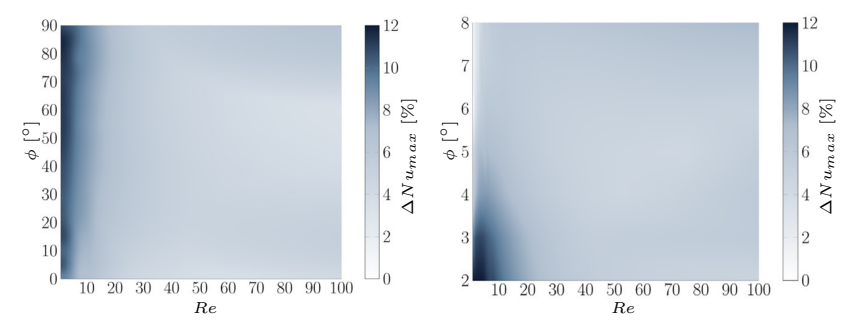


Fig. 6.14: Histogram of the deviation distribution, the solid red line defines the Gaussian distribution of the dataset.

To illustrate the dependence of the deviation of Eq. 6.3 as a function of the investigated parameter space, Fig. 6.15 shows the deviation $\Delta Nu(Re,\phi)$ for $\beta=4$ (Fig. 6.15a) and $\Delta Nu(Re,\beta)$ for $\phi=45^{\circ}$ (Fig. 6.15b) at $T_R=1.05$. It is evident that maximum deviations occur mainly for low Reynolds numbers at



(a) Contour map of $\Delta Nu(Re,\phi)$ for maximum deviations for $1 \le \beta \le 8$, $T_R = 1.05$ viations $0^\circ \le \phi \le 90^\circ$, $T_R = 1.05$

Fig. 6.15: Contour maps of the relative deviations ΔNu .

high inclination angles and low aspect ratios at $T_R = 1.05$, i.e., the extremes of the investigated parameter space.

To conclude, the novel correlation shows low deviations, i.e., $|\Delta Nu| < 4\%$, throughout the investigated parameter space. Thus, it is a promising function to be used in point-particle models to efficiently investigate multiphase flows with non-spherical particles and heat transfer.

Comparison

As mentioned in the Introduction, point-particle models of ellipsoidal particles are often based on correlation functions for spheres, e.g., the equation by Whitaker [116]. The comparison between Whitaker's equation and the novel equation Eq. 6.3 at $T_R = 1.05$ in Fig. 6.16 shows the accuracy of the newly proposed correlation also for spheres, i.e., $\beta = 1$. The trend is very well captured and the maximum deviation is less than 5% at Re = 100.

Ganguli & Lele [28] investigated the Nusselt number distribution of a sphere at low Reynolds numbers where the temperature ratio between the particle and the fluid is $T_R > 1$. The authors proposed the correlation function

$$Nu = [1 + (1 + Re)^{1/3}]e^{-0.2201\lambda + 0.00331\lambda^2 + 0.0046(Re - Re_{T_{MF}})}$$
(6.4)

with the Reynolds number $R_{T_{MF}}$ computed at the modified film temperature $T_{MF} = 0.08 \, T_P + 0.92 \, T_{\infty}$ for a sphere at $10^{-3} \le Re \le 10$. Fig. 6.17a shows the distribution of the Nusselt number Nu as a function of the Reynolds number Re for a sphere for $0 \le Re \le 10$ for the correlation function from Ganguli & Lele [28] and the correlation Eq. 6.3. The agreement between both correlation functions is even in the

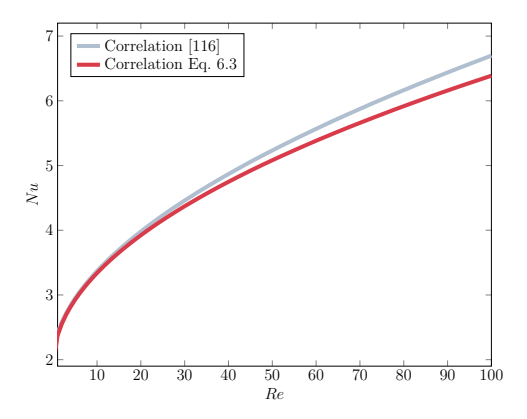


Fig. 6.16: Nusselt number Nu as a function of Reynolds number Re. Comparison of the correlation by Whitaker [116] and the novel correlation function Eq. 6.3 for a sphere at $T_R = 1.05$.

low Reynolds number regime convincing. The accuracy of the novel correlation equation is substantiated by the comparison of the correlation data with fully-resolved simulation findings in Fig. 6.17b for a sphere at $T_R=0.75$.

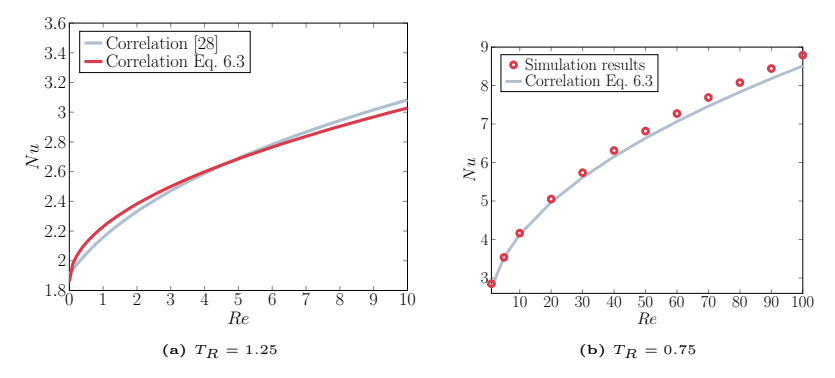


Fig. 6.17: Nusselt number Nu as a function of Reynolds number Re. Comparison of the correlation by Ganguli & Lele [28] and the novel correlation function Eq. 6.3 for a sphere at $T_R=1.25$, and fully-resolved simulation and correlation data Eq. 6.3 for a sphere at $T_R=0.75$.

It can be stated that the good agreement of the proposed correlation function with data from the literature and fully-resolved numerical simulations shows that Eq. 6.3 gives reliable results also for spheres, i.e., $\beta=1$, at varying temperature ratios. This is especially noteworthy since the genetic approach was trained by ellipsoidal data

only.

Next, a comparison of Eq. 6.3 with correlation functions for the Nusselt number for non-spherical particles is presented. To the best of the authors' knowledge, no correlation function for a likewise parameter space is available. Only Ke et al. [55] proposed a correlation function which can be considered relevant, however, without the temperature ratio as an explicit parameter. The correlation function reads

$$Nu = c_1 P r^{1/3} R e^{2/3} (\beta)^{c_2} + c_3 P r^{1/3} R e^{1/2} (\beta)^{c_4} + c_5 (\beta)^{c_6} + (\beta)^{c_7} (\beta - 1) c_8 R e^{c_9} sin^2 (c_{10} \phi)$$

$$(6.5)$$

function with the coefficients

$$c_1 = 0.0187$$
 $c_2 = 0.8829$ $c_3 = 0.5453$ $c_4 = -0.1830$ $c_5 = 1.9120$ $c_6 = 0.0646$ $c_7 = 0.7346$ $c_8 = 0.0227$ $c_9 = 0.5660$ $c_{10} = 1.0645$,

which are valid for $10 \le Re \le 200$, $0.25 \le \beta \le 2.5$, and $0^{\circ} \le \phi \le 90^{\circ}$.

Fig. 6.18 shows a comparison for the configuration $\beta=2.5$ for $\phi=0^\circ$ and $\phi=90^\circ$ for both correlation functions.

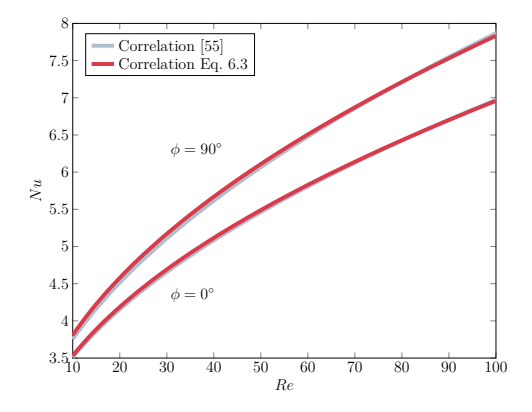


Fig. 6.18: Nusselt number Nu as a of Reynolds number Re. Comparison of the new correlation function Eq. 6.3 and the correlation function by Ke et al. [55] for $\phi=0^\circ$ and $\phi=90^\circ$ at $\beta=2.5$. The temperature ratio in Eq. 6.3 is $T_R=1.05$.

The mean deviation is $|\Delta Nu| = 0.55\%$ and the maximum deviation $|\Delta Nu_{Max}| = 1.14\%$. Other configurations show similar deviations. The mean deviation averaged over the entire parameter space is $|\Delta Nu| = 2.01\%$ and the maximum deviation is $|\Delta Nu_{Max}| = 5.79\%$. Thus, the agreement between the correlations for small T_R is very high.

Extended parameter range

The discussion of the smallest computed Nusselt number Re=1 in Ch. 6.1.4.5 shows the dependence of the dimensionless heat transfer on the aspect ratio β and the temperature ratio T_R . Masliyah & Epstein [68] derived analytical solutions for prolate ellipsoids $\beta>1$ in Stokes flow conditions. The direct comparison of the analytical solution by Masliyah & Epstein [68] and the proposed correlation Eq. 6.3 at Re=0, i.e., outside of the trained and investigated Reynolds number range, and $T_R\to 1$ yields a maximum deviation below < 10%, which is considered acceptable. The data in Tab.6.6 show the differences as a function of β . It is evident that the

β	$\Delta Nu(Re=0)$	β	$\Delta Nu(Re=0)$
1.5	-1.05%	-5	7.81%
2	1.09%	6	8.55%
3	4.45%	7	8.95%
4	6.46%	8	9.12%

Tab. 6.6: Nusselt number deviations as predicted by the analytical solution by Masliyah & Epstein [68] and Eq. 6.3 for Re=0 and $T_R\to 1$ grouped by β .

deviation increases with increasing aspect ratios.

It was previously shown that the proposed equation accurately models the heat flux dynamics within the inspected parameter ranges and therefore accurately captures the underlying physical relationships. To further support this statement, comparisons to data outside of the training dataset are conducted. While the following investigation is not meant to be a complete validation of the proposed equation in an extended range of parameter ranges, the comparisons yield convincing accuracy in parameter ranges outside the training dataset.

To show the wide applicability of the correlation Eq. 6.3, the correlation data is compared to fully-resolved simulation results for the temperature ratios $T_R = [0.55, 1.05, 1.45]$ in the range $\beta = [2, 4, 8]$ and $\phi = [0^{\circ}, 45^{\circ}, 90^{\circ}]$ up to Reynolds numbers Re = 200. The agreement of the data is convincing, i.e., the mean deviation

T_R	$\overline{\Delta Nu}$	ΔNu_{Max}	$\Delta(\Delta Nu \le 5\%)$
0.55	2.5%	7.5%	79.6%
1.05	2.6%	6.3%	80.0%
1.45	1.8%	4.0%	100.0%
ALL	2.3%	7.5%	86.6%

Tab. 6.7: Mean and maximum deviations at different temperature ratios T_R in the range $100 \le Re < 200$

is 2.3% for the extended parameter range shown in Tab. 6.7. More than 80% of all deviations between the fully-resolved results and the correlation findings are smaller than 5%.

The particle configuration $\phi = 45^{\circ}$, $\beta = 4$ at $T_R = 0.55$ and $T_R = 1.45$ is exemplarily shown in Fig. 6.19 for $1 \le Re \le 200$ with the solid line marking the

correlation results and the dots marking the fully-resolved numerical simulations. The maximum deviation is smaller than 5% within the full Reynolds number range

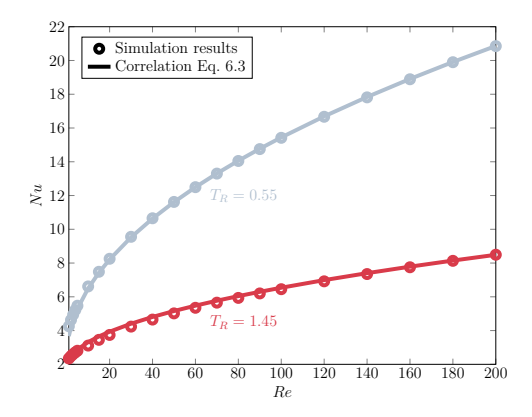


Fig. 6.19: Nusselt number Nu as a function of Reynolds number Re for an ellipsoid $\beta=4$, at an inclination angle $\phi=45^{\circ}$, and $T_R=0.55$ and $T_R=1.45$.

 $1 \le Re \le 200.$

Note that in the Reynolds number regime $Re \leq 200$ no unsteady asymmetric flow field was computed by the fully-resolved simulation. Following Richter & Nikrityuk and Sanjeevi et al. [89, 94] such a flow is expected depending on the inclination angle for Re > 250.

Furthermore, the direct comparison between the correlation results by Whitaker [116] and Eq. 6.3 for a sphere at $T_R = 1.05$ in the range $1 \le Re \le 200$ yields a maximum deviation of $\Delta Nu_{Max} = 6.87\%$.

Hence, it is fair to state that Eq. 6.3 further provides reliable results in an extended range of Reynolds numbers for spheres and ellipsoids.

6.1.6 Conclusions

A novel correlation function for solid spherical and non-spherical particles in uniform flow conditions is derived. The equation is valid for Reynolds numbers $1 \le Re \le 100$, inclination angles $0^{\circ} \le \phi \le 90^{\circ}$, aspect ratios $1 \le \beta \le 8$, and temperature ratios $0.35 \le T_R \le 1.65$. In total, more than 6 600 simulations were performed to span the complete solution space.

The analysis of the flow and temperature fields shows that the heat transfer is dominated by different fluid mechanical and geometric aspects. A higher Reynolds number yields increased inertial forces leading to higher velocity, pressure, and temperature gradients. The temperature ratio impacts the wall temperature gradient directly. The inclination angle and the aspect ratio influence the Nusselt number via geometric properties, i.e., increased pressure gradients and an increased area exposed to higher heat transfer rates. The lowest Nusselt number depends on T_R , it is obtained at the highest investigated temperature ratio $T_R = 1.65$.

The data was plugged into a genetic programming algorithm to determine a correlation function to predict Nu. The comparison of the correlation data and the fully-resolved solutions shows the high quality of the proposed correlation over the whole parameter range with a mean deviation of less than $\Delta Nu < 4\%$. The analysis of the various terms evidences the Reynolds number and the temperature ratio to be the dominant factors of the Nusselt correlation. The comparison with correlation functions from the literature and fully-resolved simulation data also evidences the high accuracy in an extended parameter range.

6.2 On the accuracy of Lagrangian point-particle models

Lagrangian point-particle models are often used for the simulation of particle-laden flows due to their lower numerical complexity compared to fully-resolved particle simulations. For particle sizes in the order of the Kolmogorov scale, they pose a good approximation and often reproduce the dynamics with reasonable accuracy. However, these models are often based on certain simplifications and assumptions which reduce the accuracy of the predictions, especially for non-spherical particles [25, 33].

In the context of heat transfer dynamics, the particles yield a direct impact on the surrounding fluid by modulating the thermal and velocity boundary layer. In point-particle models, this modulation is assumed to be isotropic for the thermal dynamics, i.e., constant along the particle surface such that local gradients between the fluid and the particle are neglected.

In order to evaluate the accuracy of such assumptions in common Lagrangian point-particle models, comparisons between fully-resolved conjugate heat transfer solutions and solutions that assume constant surface temperature are conducted.

The evolution of the thermal distribution within the particle and the fluid, the expansion of the thermal boundary layer, and the differences between fully-resolved conjugate heat transfer solutions and constant surface temperature assumptions are analyzed and discussed in the following.

6.2.1 Description of interphase dynamics

The mathematical equations of Lagrangian point-particle models differ from those used in fully-resolved particle simulations. In the following, the mathematical models for Lagrangian point-particle models are briefly described and subsequently related to the equations used in the fully-resolved configuration. Due to the focus of this investigation, only the equations related to the thermal dynamics are discussed.

In Lagrangian point-particle models, particles are reduced to finite-sized point sources. In two-way coupling the reciprocal impact is captured by correlation equations describing the interactions between the carrier fluid and the particles. For the heat dynamics, the overall particle temperature is represented by a single scalar assumed constant across the particle volume. The temporal change of the particle temperature is described by

$$\frac{dT_p}{dt} = \frac{Nu}{3 \ Pr \ Re_0} \frac{C_{p,f}}{C_{p,p}} \frac{T_f - T_p}{\tau_p} \tag{6.6}$$

with the particle relaxation time $\tau_p = \frac{\rho_p \ d_p^2}{18 \ \mu}$ [113].

Subsequently, the impact of the thermal dynamics is considered by the additional source term

$$\Delta E_T = \frac{C_{p,p}}{\gamma - 1} \, m_p \frac{dT_p}{dt} \tag{6.7}$$

in the fluid energy equation [113].

The assumptions of constant surface temperature in Lagrangian point-particle models are adapted to a configuration in a finite volume formulation in which the particles are fully-resolved by a cut-cell method. The particle temperature is reduced to a scalar value which is applied across all particles surfaces, i.e., constant surface temperature boundary conditions are applied.

The reduced particle temperature is advanced in time by

$$T_t = T_{t-1} + \Delta t \cdot \frac{q}{m_p \cdot C_{v,p}/C_{v,f}}$$
(6.8)

with the particle mass m_p and the heat capacity ratio $C_{v,p}/C_{v,f}$ at constant volume.

This is equivalent to the thermal dynamics in Lagrangian point-particle models such that the comparison between the equations outlined above and a fully-resolved conjugate heat transfer solution will highlight the inaccuracies between the two approaches.

In the conjugate heat transfer configuration, the equations described in Ch. 3.6 are used.

6.2.2 Application of boundary conditions

The application of the constant surface temperature boundary conditions is explained in the following. For the velocity, Dirichlet boundary conditions (Eqn. 3.6) are used.

Due to the coupling of pressure p, density ρ , and temperature T in the compressible formulation of the Navier-Stokes equations, the direct application of Robin boundary conditions is not feasible anymore.

Therefore, the pressure in the ghost cell p_G is determined by an extrapolation using a least-squares reconstruction at an image point I. The ghost cell density

$$\rho_G = \rho_C - \Delta n \cdot \frac{\Delta \rho}{n} \tag{6.9}$$

is determined by the equation of state with the density derivative

$$\frac{\Delta \rho}{n} = \gamma \frac{\Delta P}{T_{\Gamma}} - \frac{\rho_{\Gamma} \cdot \frac{\Delta T}{\Delta n}}{T_{\Gamma}} \tag{6.10}$$

with the temperature derivative $\Delta T/\Delta n$ of the constant surface temperature and the cell temperature with the surface density

$$\rho_{\Gamma} = \gamma \frac{p_{\Gamma}}{T_{\Gamma}}.\tag{6.11}$$

In the conjugate heat transfer configuration, the coupling boundary condition approach described in Ch. 3.6 is used.

6.2.3 Computational setup

To investigate the differences between a heat exchange model that assumes a constant surface temperature and one based on conjugate heat transfer within fully-resolved particles, numerical simulations of spherical and ellipsoidal particles in uniform flow are conducted. The configuration setup, that is, the numerical setup and the domain configuration, is equivalent to Ch. 6.1. The investigated simulations vary in the range $10 \le Re \le 100$, $1 \le \beta \le 8$, $0^{\circ} \le \phi \le 90^{\circ}$, and $0.5 \le T_R \le 2.0$. The distinct parameters investigated are shown in Tab. 6.8.

Parameter	Value
Reynolds number $Re_{d_{eq}}$	10,25,50,100
Particle aspect ratio β	1,2,4,8
Particle angle ϕ	0°, 45°, 90°
Temperature ratio T_R	0.5, 0.95, 1.05, 1.5, 2.0
Particle density ratio ρ_p/ρ_f	600.0
Prandtl number Pr	0.72
Mach number Ma	0.1

Tab. 6.8: Parameter range for the conjugate heat transfer configuration.

The given initial temperature ratio $T_R = T_p/T_f$ is applied to the particles in relation to the fluid reference temperature T_0 . It follows that $T_p = T_R \cdot T_f \cdot T_0$. The particle temperature is assumed spatially constant in the constant surface temperature configuration on all particle surfaces. In the configuration pertaining to the conjugate heat transfer model, the particle temperature T_p/T_0 is initially applied constant within the particle, i.e., the particles initially have an isothermal temperature distribution.

For the simulations, a minimum cell length of $\Delta l_{min}=0.011$ is used such that the equivalent diameter of the particles is resolved by 92 cells. Adaptive mesh refinement is used where the mesh is locally refined based on the instantaneous flow field resulting from the particle surfaces and the temperature derivative. The flow field in the fluid domain is furthermore refined based on the shear stress distribution. An

example of a 2D cut plane of an ellipsoidal particle with $\beta=8$ and $\phi=45^{\circ}$, and the fluid for the conjugate heat transfer configuration is shown in Fig. 6.20.

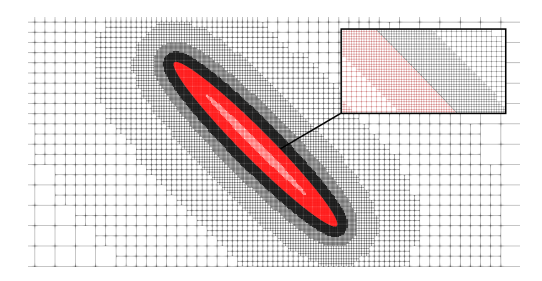


Fig. 6.20: Initial grid $\beta=8$ and $\phi=45^\circ$. In the conjugate heat transfer configuration the black (fluid) and the red grid (particle) is resolved whereas in the constant surface temperature configuration only the black grid lines (fluid) are considered.

In the constant surface temperature configuration the same grid is considered, however, without resolving the inside of the particles, i.e., the red grid cells are neglected.

6.2.4 Results and discussion

In the following, the results of the different numerical configurations are presented. The differences of the particle surface temperature assumptions are discussed and the impact on the particles and the fluid is outlined.

6.2.4.1 Particle temperature

The thermal dynamics of the particles are presented. To define the particle temperature in the conjugate heat transfer configuration, two different approaches are considered.

First, the volume-averaged temperature of all cells inside the solid particles is considered. Fig. 6.21 shows the temporal development of the volume-averaged particle temperature $T_{p,c}/T_0$ for an ellipsoidal particle $\beta=8$ for particle angles $\phi=0^\circ$, $\phi=45^\circ$, and $\phi=90^\circ$ in uniform flow Re=100 with initial temperature ratio $T_R=2.0$.

The temporal development of the inspected configurations varies based on the angle of attack. The angle is in relation to the flow streamwise direction as shown in Fig. 2.2, i.e., for angles $\phi=0^{\circ}$ a slender body and for $\phi=90^{\circ}$ a bluff body is observed. It is shown that for bluff bodies, an increased decay of particle temperature is found in comparison to slender bodies. The particle rotated by 45° degrees shows a distribution inbetween the other two configurations. However, the temporal

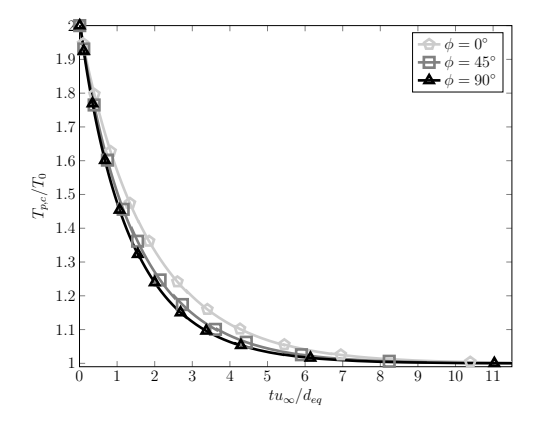


Fig. 6.21: Temporal distribution of the particle cell-averaged temperature $T_{p,c}/T_0$ at Re=100, $\beta=8$, and initial temperature ratio $T_R=2.0$ for $\phi=0^\circ$, $\phi=45^\circ$, $\phi=90^\circ$ for the conjugate heat transfer configuration.

development of $T_{p,c}/T_0$ for $\phi=45^\circ$ is closer to the development of the bluff body than the slender body.

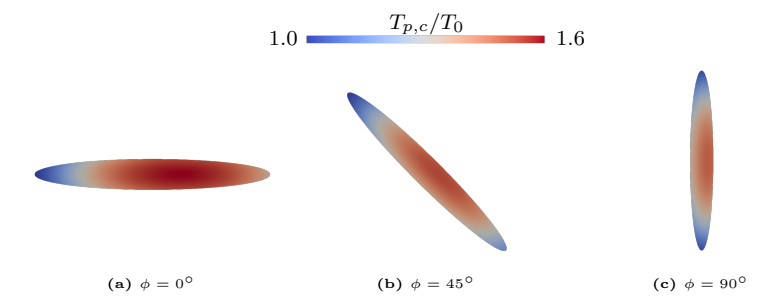


Fig. 6.22: Temperature distribution inside of an ellipsoidal particle $\beta=8$ in uniform flow at Re=100 for an arbitrary time step. The particle is coupled to the surrounding fluid by the conjugate heat transfer algorithm presented in Ch. 3.6 and the initial temperature distribution was isothermal with $T_R=2.0$. The particle temperature field is in relation to the reference temperature T_0 .

To investigate what causes the differences in particle temperature between the different angles, Fig. 6.22 shows a cut through the center of mass of the three inspected particles. Stark temperature gradients inside the particles are prevalent where the particle tips are found to be of lower temperature than the rest of the particles. Due to the large exposed area to the fluid of the particle tip, the temperature gradients are increased. For the angle $\phi = 0^{\circ}$ only one of the tips is directly exposed to

the undisturbed uniform flow. In the other configurations, both particle tips are exposed to the undisturbed fluid flow at the surface. Consequently, the heated fluid is transported away such that the gradients at the surface of the particle are consistently increased. This results in larger temperature gradients inside the particle and subsequently in increased cooling rates of the particle at the tips. The differences in the number of tips subject to the fluid flow then explains the increased cooling rates of non-slender bodies. Within the particles, the particle tips facilitate the conductive transport of energy due to increased gradients. Furthermore, the particle configurations $\phi=45^\circ$ and $\phi=90^\circ$ expose a larger surface area to the undisturbed flow field. The increased gradients at the particle inside facing the undisturbed flow field on the windward side result in larger thermal dynamics. Consequently, the particle configurations with increasing inclination angles are shown to decrease their temperature faster than the slender body configuration.

Next, the area-averaged surface temperature of all surfaces of the solid particles in the conjugate heat transfer configuration is considered.

The starting phase of the simulation run is inspected, i.e., $t u_{\infty}/d_{eq} < 1$, and shown in Fig. 6.23. The simulation configuration is Re = 100, $T_R = 2.0$, and $\beta = 8$ for $\phi = 0^{\circ}$, $\phi = 45^{\circ}$, and $\phi = 90^{\circ}$.

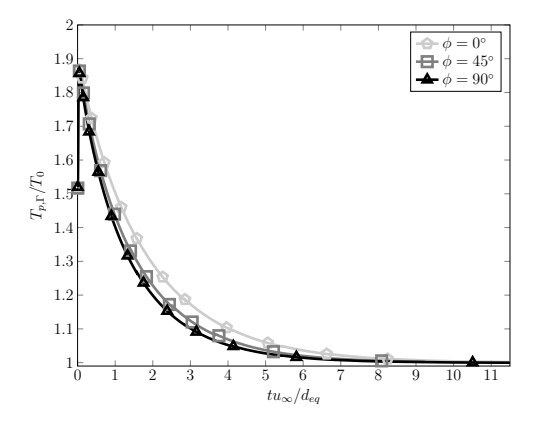


Fig. 6.23: Temporal distribution of the particle surface-averaged temperature $T_{p,\Gamma}/T_0$ at $Re=100,\ \beta=8$, and initial temperature ratio $T_R=2.0$ for $\phi=0^\circ,\ \phi=45^\circ,\ \phi=90^\circ$ for the conjugate heat transfer configuration.

As shown, the initial surface temperature is lower than the volume-averaged particle temperature. The conjugate heat transfer model uses an iterative approach which minimizes the heat flux differences between the fluid and the solid phase such that an energy-conserving method is ensured. In the initial time steps, the thermal conductivity k(T), and the large temperature gradients ΔT between the two phases limit the transfer of thermal energy. This explains the rapid increase of the surface

temperature in the initial time steps. As the thermal boundary layer builds up inside the fluid the energy flux through the interface line is conserved. While this can be controlled by choosing different parameters, the set of parameters chosen in this investigation corresponds to solid biomass particles embedded in air [69].

The dynamics of the initial phase with the slow build up of the thermal boundary layer are not captured by the constant surface temperature approach. The surface temperature corresponds to the particle temperature such that a conservative heat flux cannot be guaranteed.

However, the overall distributions of the different inclination angle configurations are similar to the cell-averaged temperature distributions in Fig. 6.21.

The temporal development of the particle temperature is inspected next. The simulation setup at Re=100, $\beta=8$, $\phi=45^{\circ}$, and $T_R=2.0$ is considered. The particle temperature T_p/T_0 in the conjugate heat transfer model is equivalent to the volume-averaged particle temperature $T_{p,c}/T_0$ as outlined above. The particle temperature in the constant surface temperature configuration and conjugate heat transfer configuration are compared in Fig. 6.24.

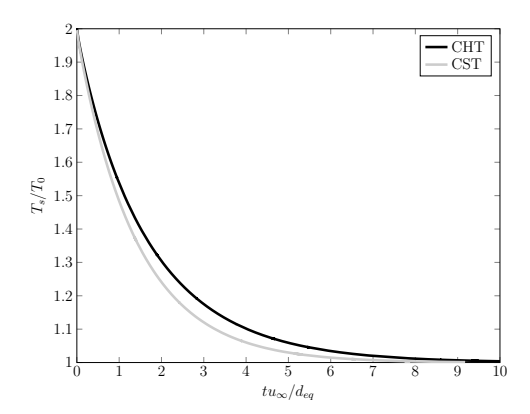


Fig. 6.24: Temporal distribution of the particle cell-averaged temperature $T_{p,c}/T_0$ at Re=100, $\beta=8$, $\phi=45^\circ$, and initial temperature ratio $T_R=2.0$ for the conjugate heat transfer configuration (CHT) and the constant surface temperature (CST) configuration.

The overall shape of the temperature distributions is similar for the conjugate heat transfer and the constant surface temperature configuration. However, the two distributions do not coincide exactly. That is, the temperature in the conjugate heat transfer configuration decreases slower than in the constant surface temperature model. Due to the varying heat transfer rates and subsequent temperature gradients along the particle surfaces, the conjugate heat transfer model results in lower temperature decay overall. This is especially relevant in non-spherical particles where the windward and leeward side are subject to different mechanical loads. This aspect

is neglected in the constant surface temperature model. Therefore, the constant surface temperature model not only decreases its temperature faster but also reaches an equilibrium with the surrounding surface faster which further impacts the temporal development of the surrounding carrier fluid.

6.2.4.2 Fluid dynamics

The impact of the varying surface dynamics on the carrier fluid is discussed in the following.

The simulation configuration Re = 100, $\beta = 8$, $\phi = 45^{\circ}$, and $T_R = 2.0$ is inspected. The temperature contours of the fluid are shown in Fig. 6.25 for both configurations at a timestep in which the volume-averaged particle temperature is roughly equal with $T_{p,c}/T_0 \approx 1.5$. At the shown time step, the velocity field is steady.

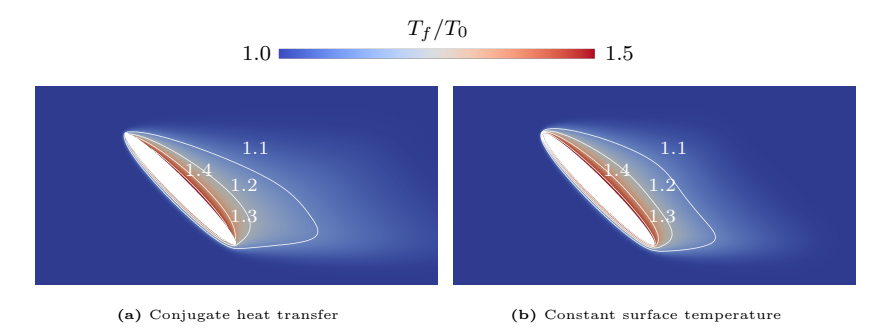


Fig. 6.25: Comparison of the fluid temperature contours for an ellipsoid $\beta=8$ and $\phi=45^{\circ}$ at Re=100. The initial temperature ratio is $T_R=2.0$ and the particles are shown at a timestep where the cell-averaged temperature is $T_P/T_0\approx 1.5$.

The temperature contour for $T_f/T_0 = 1.1$ varies between the conjugate heat transfer and the constant surface temperature configuration. While the conjugate heat transfer contour has only a narrow extension near the tip on the top of the ellipsoidal particle, the constant surface temperature contour line is more extended.

The reason for this is shown in Fig. 6.26 where the tip of the particle is magnified. The contour lines align much closer to the particle tip in the conjugate heat transfer configuration due to the lower particle temperatures at the tips.

The distributions of the contour lines for $T_f/T_0 = 1.2$, $T_f/T_0 = 1.3$, and $T_f/T_0 = 1.4$ are also modulated. While the impact is decreased in the near vicinity of the particle leeward side, the distributions of the temperature contours vary at the particle tips and the windward side. As shown in Fig. 6.26, the particle tips are not covered by the contour lines for $T_F/T_0 \geq 1.2$ in the conjugate heat transfer

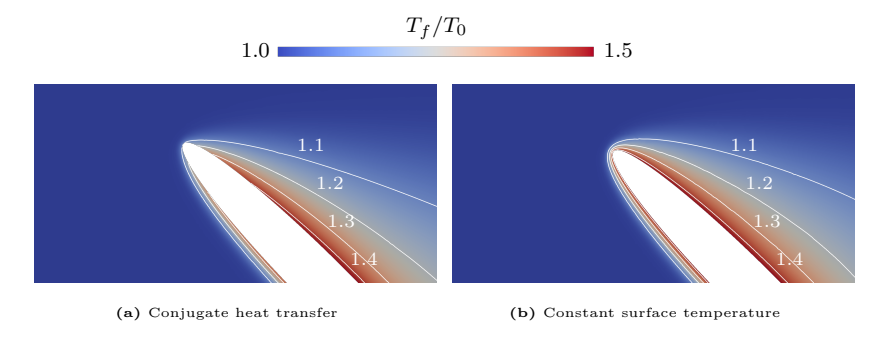


Fig. 6.26: Comparison of the particle tips temperature contours for an ellipsoid $\beta=8$ and $\phi=45^{\circ}$ at Re=100. The initial temperature ratio is $T_R=2.0$ and the particles are shown at a timestep where the cell-averaged temperature is $T_p/T_0\approx 1.5$.

configuration which is opposite to the constant surface temperature configuration. The tip is fully covered by increased temperature contour line. Similar dynamics are observed on the windward side of the particle.

Due to the impact of the locally varying temperature inside the particle and on the surface intersecting the solid and the fluid, the particle tips are cooler than the rest of the ellipsoidal particle. The fluid flow then increases the temperature gradients nearby. This results in faster temperature decreases due to the advective flow and the larger area to volume ratio near the tips which has severe implications on the temperature field in the fluid downstream.

Subsequently, the thermal boundary layer is significantly modulated by the assumption of the constant surface temperature distribution. To be more precise, the assumption of a constant surface temperature neglects the local impact of the temperature distribution which subsequently influences the development of the thermal dynamics inside the fluid. Due to the low Mach number, the velocity field is not modulated noticeably.

The impact of the local temperature variations on specific coefficients is explored in the following. Since the linear and rotational movement and the heat transfer dynamics in Lagrangian point-particle models are commonly described by the drag-, lift-, and torque coefficients and the Nusselt number [25, 113], the aforementioned coefficients are investigated.

A simulation with Re = 100, $\beta = 8$, $\phi = 45^{\circ}$ and an initial homogeneous temperature distribution of $T_R = 2.0$ is investigated. Shown in Tab. 6.9 are the aforementioned coefficients for the constant surface temperature (CST) configuration, the conjugate heat transfer (CHT) configuration, and a reference configuration at isothermal conditions (ISO) where the impact of the thermal dynamics is neglected. For the constant surface temperature and conjugate heat transfer configuration,

the timestep at which the coefficients are evaluated is chosen such that the same volume-averaged temperature $T_p/T_0 \approx 1.15$ is given.

Parameter	CST	CHT	ISO
$\overline{\text{Drag } C_D}$	1.852	1.842	1.811
Lift C_L	$-1.146 \cdot 10^{-6}$	$-1.002 \cdot 10^{-6}$	$-7.515 \cdot 10^{-7}$
Torque C_T	$-1.305 \cdot 10^{-4}$	$-1.269 \cdot 10^{-4}$	$-1.393 \cdot 10^{-4}$
Nusselt Nu	10.008	10.783	_

Tab. 6.9: Drag, lift, and torque coefficient and Nusselt number for the constant surface temperature configuration, the conjugate heat transfer configuration, and an isothermal reference configuration.

The data indicates that the temperature impacts all inspected coefficients. However, the order of the modulation varies between the constant surface temperature and the conjugate heat transfer configuration. The drag coefficient is increased in the constant surface temperature configuration by 2.3% where it is increased by 1.7% in the conjugate heat transfer configuration, i.e., roughly 0.6% less. The lift and torque coefficient are modulated similarly. The relative small impact of the non-thermal components is owed to the low Mach number Ma=0.1. This is expected but shows the inaccuracies of the constant surface temperature assumption even at low Mach number configurations.

In the conjugate heat transfer configuration, the Nusselt number increases by 7.7% compared to the CST configuration. This increase is primarily due to significant differences in heat flux between the windward and leeward sides of the particle, driven by steep temperature gradients along its surface. These gradients result from local variations in surface temperature, which modulate the thermal boundary layer in the fluid flow. Consequently, these variations influence the local heat flux and contribute to the increased Nusselt number.

While the observed differences are small, the results indicate that even at low temperature ratios the relevant coefficients used in Lagrangian point-particle models are inaccurate in comparison to fully-resolved simulations such that the Lagrangian point-particle approach with the given formulations can only pose an approximation.

6.2.5 Conclusions

The impact of locally varying heat exchange is investigated by comparison of constant surface temperature and conjugate heat transfer assumptions. This assumption is often made in Lagrangian point-particle models such that the investigation is synonymous for the inspection of the accuracy of the point-particle approach.

The comparison is conducted for fixed ellipsoidal particles in the range $10 \le Re \le 100, \ 1 \le \beta \le 8, \ 0^{\circ} \le \phi \le 90^{\circ}, \ {\rm and} \ 0.5 \le T_R \le 2.0$ in uniform flow.

First, the particle temperature is investigated for an ellipsoidal particle with aspect ratio $\beta=8$ and initial temperature ratio $T_R=2.0$ in uniform flow with Re=100 for $\phi=0^{\circ}$, $\phi=45^{\circ}$, and $\phi=90^{\circ}$. The results show that the inclination angle has a large effect on the temporal decrease of the particle temperature. To be more

precise, the particle tips are subject to the undisturbed fluid flow and facilitate the temperature decrease due to increasing gradients as a consequence of the advective fluid flow near the surfaces of the particle tips.

Additionally, the initial surface temperature of the particle appears to differ from the particle temperature. Since the conjugate heat transfer approach is energy conserving, the initial surface temperature differs from the particle temperature. The solid-fluid interaction can only transfer thermal energy based on the thermal conductivity. Consequently, the comparison of the temporal development of the particle temperature in a constant surface temperature configuration and a conjugate heat transfer configuration yields different distributions. To be more precise, the constant surface temperature decreases faster due to the neglect of the local temperature variations along the particle surface.

The impact of the two assumptions on the fluid dynamics is discussed next. The temperature contour lines are noticeably modulated since the locally decreased temperature at the particle tips is not considered in the constant surface temperature configuration. The thermal boundary layer is modulated which prevails especially near the particle tips and the elongated axis at the windward and leeward side.

As a result, the key figures used in Lagrangian point-particle models, namely the drag, lift, and torque coefficient and the Nusselt number, differ between the constant surface temperature model and the conjugate heat transfer model. In comparison to an isothermal configuration at the same fluid properties, the drag, lift, and torque coefficient are only slightly modulated. This is expected due to the low Mach number in the investigation. However, the Nusselt number is increased by approx. 7% in the conjugate heat transfer model due to the local variations in the particle surface temperature which impacts the thermal boundary layer in the fluid.

The results indicate that the impact of locally varying heat exchange between solid particles and the carrier fluid is of high importance in non-spherical particle configurations.

7 Conclusions and Outlook

The present thesis explores the interaction of spherical and non-spherical solid particles with the carrier fluid in multiphase flows.

The numerical simulations of the particles are conducted using an immersed-boundary method in a finite volume framework. The aspect ratios of the particles are in the range $1 \le \beta \le 8$, which are fully resolved by a cut-cell method to ensure the conservation of mass, momentum, and energy at the particle interfaces.

To facilitate the computation of different physical problems, several enhancements were implemented within the simulation framework m-AIA.

A parallel particle solver is introduced to optimize performance on high-performance computing systems. The solver operates on a local/global id principle and uses Newmark and Crank-Nicholson integration schemes to accurately capture the motion of free-moving particles. A modified hard-sphere collision model is presented to account for particle-particle and particle-wall collisions.

A novel solver for the solution of the conservation equation for the enthalpy is developed. The solver facilitates accurate computation of the heat dynamics within solid bodies of arbitrary geometry by fully resolving their internal structure. The solver is coupled to the surrounding carrier fluid by an iterative conjugate heat transfer approach. Thermal energy exchanges are computed such that local temperature gradients are considered and energy conservation is ensured which results in increased accuracy inside the particles and the fluid flow.

A local mesh extension algorithm for the numerical stabilization of particles at the domain boundaries is presented. The novel algorithm, called adaptive mesh extension, supports the addition of cells extending beyond the computational domain. The algorithm enhances the stability during computations and facilitates accurate numerical intersections and conservative interactions among moving particles beyond the domain of investigation.

A slicing technique to couple and synchronize multiple different domains is presented. In the investigation of fully-developed periodic pipe and free jet flow, the domains are coupled such that the instantaneous solution of the pipe flow is used as inflow condition for the free jet domain. This allows the seamless transition between the two domains and eliminates the necessity for assumptions or artificial turbulence for the jet inflow area and the associated particle dynamics.

The newly developed methods are used in different configurations consisting of isothermal and non-isothermal problems.

First, a particle-laden turbulent free jet flow is inspected. This configuration is a first approximation of biomass combustion in industrial combustion plants. Initially,

the influence of the thermal dynamics is neglected such that the aerodynamic properties of the particles and the flow in a turbulent free jet are investigated. The turbulent free jet is computed concurrently with a fully-developed, particle-laden turbulent pipe flow. The latter provides the inflow data for the jet. This setup ensures physically correct particle and fluid properties at the jet inflow boundary which eliminates the necessity for random inflow assumptions. The problem contains spherical and ellipsoidal particles with aspect ratios $1 \le \beta \le 8$ and relative particle volume-loading of $\xi_v \approx 6.67 \cdot 10^{-4}$ for Ma = 0.1 and $Rebulk = 15\,546$.

The fully-developed pipe flow and the free jet are evaluated independently of each other.

Within the pipe domain, the particles exhibit a preferential concentration at approximately $r/D \approx 0.35$. An examination of the individual aspect ratios reveals that the particle tends to approach the center of the domain with greater frequency as the aspect ratio β increases. Non-spherical particles exhibit a preferential orientation of approximately $90^{\circ} \pm 35^{\circ}$ with respect to the streamwise axis which is related to the anisotropic particle geometry. The investigation of the interphase energy exchange reveals that ellipsoidal particles invoke larger transfer of kinetic energy in comparison to spherical particles. This trend is especially prevalent in the near-wall region of the pipe where the ellipsoidal particles lead the fluid and subsequently transfer kinetic energy to the fluid. Closer to the pipe center, the particles trail the fluid and extract energy from the fluid resulting in location-dependent energy dynamics. Similar dynamics are observed for the particle-induced dissipation. The particles tend to increase the dissipation rates in close proximity to the pipe wall, i.e., a location where the particles lead the fluid.

The inspection of the subsequent jet domain shows that the dynamics in the near-field range, i.e., $x/D \leq 10$, are modulated by the particles. The presence of the particles elicits a reduction of the radial extension of the jet flow by $\sim 4\%$ and an elongation of the centerline velocity by $\sim 10\%$. This is shown to be caused by the tendency of the particles to induce higher dissipation towards the pipe walls than at the pipe center, i.e., a relative shift in the local energy budget is observed. Within the near-field range, the tendency of the particles to break up coherent large-scale fluid motions, impose an energy cascade towards the small-scale motions, and increase the dynamics in the particle wake results in a greater decline of kinetic energy in the range $x/D \geq 6$. The comparison between the particle-laden case and a single-phase reference flow indicates that the total kinetic energy is reduced by approximately $\sim 9\%$ in the particle-laden case whereas the turbulence intensity is reduced by $\sim 20\%$.

Subsequently, the thermal dynamics in multiphase flow are investigated under assumptions of constant surface temperature and conjugate heat transfer.

To derive a correlation function for the Nusselt number Nu for ellipsoidal particles in uniform flow, more than 6 600 fully-resolved simulations are computed within the parameter space defined by Reynolds number $1 \le Re \le 100$, aspect ratio $1 \le \beta \le 8$, orientation angle $0^{\circ} \le \phi \le 90^{\circ}$, and temperature ratio $0.35 \le T_R \le 1.65$. The

results are analyzed to derive a correlation function aimed at enhancing the accuracy of Lagrangian point-particle models. The equation's accuracy is evaluated through comparisons within the investigated parameter space and an extended range beyond it. A sensitivity analysis is conducted to highlight the impact of various terms and parameters on heat transfer dynamics.

Finally, a novel solver for computing heat dynamics in fully-resolved solid bodies is presented. This solver can solve the conservation equation for enthalpy, thereby enabling accurate prediction of heat equalization processes within solid bodies of arbitrary shape. An efficient iterative coupling ensures correct exchange between the body and surrounding fluid. The model is validated with emphasis on parallel efficiency. Subsequently, the model is exemplarily used to assess the accuracy of assumptions made in Lagrangian point-particle models.

Outlook

The dynamics of non-spherical particles, as observed in industrial combustion engines, are highly complex. Thus, the presented work can only describe a fraction of the overall dynamics.

In future work, the dynamics of fully-resolved particle-laden pipe-jet flow under consideration of temperature gradients between the particles and the fluid need to be investigated. For this purpose, novel solvers allow for the inspection of such dynamics by incorporating the impact of local temperature gradients. The author hypothesizes that the relative position of particles inside the pipe differs in comparison to an isothermal configuration. Consequently, the modulation of flow dynamics is altered, resulting in different flow fields.

Additionally, solid particles undergo significant shape and mass changes during combustion processes [42, 88]. The impact of temporally changing particle parameters needs to be assessed. Comparisons with experimental investigations and single-phase reference data will highlight the impact of combustion processes in more detail, resulting in more accurate data. As shown in this thesis, the aspect ratio of particles results in different dynamics between spherical and ellipsoidal particles. Therefore, it is expected that the impact on fluid varies as particle shape and mass change over time.

References

- M Aftosmis, J Melton & M Berger. "Adaptation and surface modeling for Cartesian mesh methods". 12th Computational Fluid Dynamics Conference. 1995, p. 1725.
- [2] R. Aris. Vectors, Tensors and the Basic Equations of Fluid Mechanics. Courier Corporation, 2012.
- [3] A. Askarova, S. Bolegenova, V. Maximov, M. Beketayeva & P. Safarik. "Numerical Modeling of Pulverized Coal Combustion at Thermal Power Plant Boilers". *Journal of Thermal Science* 24.3 (2015), pp. 275–282.
- [4] A. S. Askarova, S. A. Bolegenova, V. Y. Maximov, A. Bekmukhamet, M. T. Beketayeva & Z. K. Gabitova. "Computational Method for Investigation of Solid Fuel Combustion in Combustion Chambers of a Heat Power Plant". *High Temperature* 53.5 (2015), pp. 751–757.
- [5] E Atta. "Component-adaptive grid interfacing". 19th Aerospace Sciences Meeting. 1981, p. 382.
- [6] P. Bagchi, M. Ha & S Balachandar. "Direct Numerical Simulation of Flow and Heat Transfer From a Sphere in a Uniform Cross-Flow". J. Fluids Eng. 123.2 (2001), pp. 347–358.
- [7] S Balachandar & J. K. Eaton. "Turbulent Dispersed Multiphase Flow". Annual Review of Fluid Mechanics 42.1 (2010), pp. 111–133.
- [8] C. Ball, H Fellouah & A Pollard. "The flow field in turbulent round free jets". Progress in Aerospace Sciences 50 (2012), pp. 1–26.
- [9] J Benek, T Donegan & N Suhs. "Extended chimera grid embedding scheme with application to viscous flows". 8th Computational Fluid Dynamics Conference. 1987, p. 1126.
- [10] J Benek, J Steger & F. C. Dougherty. "A flexible grid embedding technique with application to the Euler equations". 6th Computational Fluid Dynamics Conference Danvers. 1983, p. 1944.
- [11] M. Berger & M. Aftosmis. "Progress towards a Cartesian cut-cell method for viscous compressible flow". AIAA Paper (2012), pp. 1301–1325.
- [12] D. L. Black & M. Q. McQuay. "Laser-based particle measurements of spherical and nonspherical particles". *International Journal of Multiphase Flow* 27.8 (2001), pp. 1333–1362.

- [13] J. Borgelt, T. Hösgen, M. Meinke & W. Schröder. "Analysis of the hot gas ingress into the wheel space of an axial turbine stage". *International Conference on High Performance Computing in Science and Engineering*. Springer. 2021, pp. 207–221.
- [14] H.-J. Bungartz, F. Lindner, B. Gatzhammer, M. Mehl, K. Scheufele, A. Shukaev & B. Uekermann. "preCICE—a fully parallel library for multi-physics surface coupling". Computers & Fluids 141 (2016), pp. 250–258.
- [15] P. Burattini, R. Antonia, S. Rajagopalan & M. Stephens. "Effect of initial conditions on the near-field development of a round jet". Experiments in Fluids 37 (2004), pp. 56–64.
- [16] I. Cannon, S. Olivieri & M. E. Rosti. "Spheres and fibers in turbulent flows at various Reynolds numbers". Physical Review Fluids 9.6 (2024), p. 064301.
- [17] X. Chang, R. Ma, N. Wang, Z. Zhao & L. Zhang. "A parallel implicit hole-cutting method based on background mesh for unstructured Chimera grid". Computers & Fluids 198 (2020), p. 104403.
- [18] L. Chen, K. Asai, T. Nonomura, G. Xi & T. Liu. "A review of Backward-Facing Step (BFS) flow mechanisms, heat transfer and control". Thermal Science and Engineering Progress 6 (2018), pp. 194–216.
- [19] T. Chiang & T. W. Sheu. "A numerical revisit of backward-facing step flow problem". Physics of Fluids 11.4 (1999), pp. 862–874.
- [20] C Chin, J. Monty & A Ooi. "Reynolds number effects in DNS of pipe flow and comparison with channels and boundary layers". *International Journal* of Heat and Fluid Flow 45 (2014), pp. 33–40.
- [21] C. Chin, A. Ooi, I. Marusic & H. Blackburn. "The influence of pipe length on turbulence statistics computed from direct numerical simulation data". *Physics of Fluids* 22.11 (2010).
- [22] A. Einstein. "Eine neue Bestimmung der Moleküldimensionen". PhD thesis. ETH Zürich, 1905.
- [23] N Ellendt, A. Lumanglas, S. I. Moqadam & L M\u00e4dler. "A model for the drag and heat transfer of spheres in the laminar regime at high temperature differences". *International Journal of Thermal Sciences* 133 (2018), pp. 98– 105.
- [24] Y. Feng, H. Liu & X. Zheng. "The modulation of coherent structures by the near-wall motions of particles". *Journal of Fluid Mechanics* 981 (2024), A26.
- [25] K. Fröhlich, P. Farmand, H. Pitsch, M. Meinke & W. Schröder. "Particle Reynolds number effects on settling ellipsoids in isotropic turbulence". *Inter*national Journal of Multiphase Flow 139 (2021), p. 103566.
- [26] K. Fröhlich, M. Meinke & W. Schröder. "Correlations for inclined prolates based on highly resolved simulations". *Journal of Fluid Mechanics* 901 (2020), A5.

- [27] N. Frössling. "Über die Verdunstung fallernder Tropfen". Gerlands Beitr. Geophys. 52 (1938), pp. 170–216.
- [28] S. Ganguli & S. K. Lele. "Drag of a heated sphere at low Reynolds numbers in the absence of buoyancy". *Journal of Fluid Mechanics* 869 (2019), pp. 264– 291.
- [29] R. Glowinski, T.-W. Pan, T. I. Hesla, D. D. Joseph & J. Periaux. "A Fictitious Domain Approach to the Direct Numerical Simulation of Incompressible Viscous Flow past Moving Rigid Bodies: Application to Particulate Flow". Journal of Computational Physics 169.2 (2001), pp. 363–426.
- [30] M. Gondrum, A. Niemöller, M. Meinke, W. Schroeder, A. Rubio Carpio, D. Ragni & F. Avallone. "Landing gear noise mitigation by an upstream installed fairing". 28th AIAA/CEAS Aeroacoustics 2022 Conference. 2022, p. 2847.
- [31] R. Gore & C. T. Crowe. "Effect of particle size on modulating turbulent intensity". *International Journal of Multiphase Flow* 15.2 (1989), pp. 279– 285.
- [32] C. Günther, M. Meinke & W. Schröder. "A flexible level-set approach for tracking multiple interacting interfaces in embedded boundary methods". Computers & Fluids 102 (2014), pp. 182–202.
- [33] N. Guo, T. Li, L. Zhao & T. Løvås. "Eulerian-Lagrangian simulation of pulverized biomass jet using spheroidal particle approximation". Fuel 239 (2019), pp. 636–651.
- [34] Q. Guo, X. Chen & H. Liu. "Experimental research on shape and size distribution of biomass particle". Fuel 94 (2012), pp. 551–555.
- [35] A Gupta, H. Clercx & F Toschi. "Effect of particle shape on fluid statistics and particle dynamics in turbulent pipe flow". The European Physical Journal E 41 (2018), pp. 1–15.
- [36] D. Hartmann, M. Meinke & W. Schröder. "An adaptive multilevel multigrid formulation for Cartesian hierarchical grid methods". Computers & Fluids 37.9 (2008), pp. 1103–1125.
- [37] D. Hartmann, M. Meinke & W. Schröder. "Differential equation based constrained reinitialization for level set methods". *Journal of Computational Physics* 227.14 (2008), pp. 6821–6845.
- [38] D. Hartmann, M. Meinke & W. Schröder. "A strictly conservative Cartesian cut-cell method for compressible viscous flows on adaptive grids". Computer Methods in Applied Mechanics and Engineering 200.9-12 (2011), pp. 1038– 1052.
- [39] D. Hartmann, M. Meinke & W. Schröder. "A strictly conservative Cartesian cut-cell method for compressible viscous flows on adaptive grids". Computer Methods in Applied Mechanics and Engineering 200.9-12 (2011), pp. 1038– 1052.

- [40] L. He & M. L. G. Oldfield. "Unsteady Conjugate Heat Transfer Modeling". Journal of Turbomachinery 133.3 (2010), p. 031022. ISSN: 0889-504X.
- [41] C. W. Hirt, A. A. Amsden & J. Cook. "An arbitrary Lagrangian-Eulerian computing method for all flow speeds". *Journal of Computational Physics* 14.3 (1974), pp. 227–253.
- [42] P. Holmgren, D. R. Wagner, A. Strandberg, R. Molinder, H. Wiinikka, K. Umeki & M. Broström. "Size, shape, and density changes of biomass particles during rapid devolatilization". Fuel 206 (2017), pp. 342–351.
- [43] A. Hölzer & M. Sommerfeld. "New simple correlation formula for the drag coefficient of non-spherical particles". Powder Technology 184.3 (2008), pp. 361– 365
- [44] T. Hösgen, M. Meinke & W. Schröder. "Analysis of Ingress Into the Downstream Wheel Space of a 1.5-Stage Turbine By Full Circumference and Single Blade Passage Large-Eddy Simulations". *Journal of Turbomachinery* 146.9 (2024).
- [45] P. Van der Houwen. "Explicit Runge-Kutta formulas with increased stability boundaries". Numerische Mathematik 20.2 (1972), pp. 149–164.
- [46] X Huang, M Albers, P. Meysonnat, M Meinke & W Schröder. "Analysis of the effect of freestream turbulence on dynamic stall of wind turbine blades". *International Journal of Heat and Fluid Flow* 85 (2020), p. 108668.
- [47] X Huang, S. A. Moghadam, P. Meysonnat, M Meinke & W Schröder. "Numerical analysis of the effect of flaps on the tip vortex of a wind turbine blade". International Journal of Heat and Fluid Flow 77 (2019), pp. 336–351.
- [48] A. Jameson. "Solution of the Euler equations for two dimensional transonic flow by a multigrid method". Applied Mathematics and Computation 13.3 (1983), pp. 327–355. ISSN: 0096-3003.
- [49] B. Jenkins & P. Mullinger. Industrial and Process Furnaces: Principles, Design and Operation. Elsevier, 2011.
- [50] F. Jiang, L Zhao, H. I. Andersson, K. Gustavsson, A. Pumir & B. Mehlig. "Inertial torque on a small spheroid in a stationary uniform flow". *Physical Review Fluids* 6.2 (2021), p. 024302.
- [51] B. John, P Senthilkumar & S. Sadasivan. "Applied and Theoretical Aspects of Conjugate Heat Transfer Analysis: A Review". Archives of Computational Methods in Engineering 26 (2019), pp. 475–489.
- [52] D Kaftori, G Hetsroni & S Banerjee. "Particle behavior in the turbulent boundary layer. I. Motion, deposition, and entrainment". Physics of Fluids 7.5 (1995), pp. 1095–1106.
- [53] D Kaftori, G Hetsroni & S Banerjee. "Particle behavior in the turbulent boundary layer. II. Velocity and distribution profiles". *Physics of Fluids* 7.5 (1995), pp. 1107–1121.

- [54] K. Kang, M. Zhu, G. Sun & X. Guo. "Fossil fuels versus biofuels: Perspectives on greenhouse gas emissions, energy consumptions, and projections". In: Fuel Processing and Energy Utilization. Chapman and Hall/CRC, 2019, pp. 1–14.
- [55] C. Ke, S. Shu, H. Zhang, H. Yuan & D. Yang. "On the drag coefficient and averaged Nusselt number of an ellipsoidal particle in a fluid". *Powder Technology* 325 (2018), pp. 134–144.
- [56] D. P. Kingma & J. Ba. "Adam: A method for stochastic optimization". arXiv preprint arXiv:1412.6980 (2014).
- [57] T. Kiwitt, K. Fröhlich, M. Meinke & W. Schröder. "Numerically determined Nusselt correlation for ellipsoidal particles". International Conference on Heat Transfer, Fluid Mechanics and Thermodynamics (HEFAT). 2021.
- [58] T. Kiwitt, K. Fröhlich, M. Meinke & W. Schröder. "Nusselt correlation for ellipsoidal particles". *International Journal of Multiphase Flow* 149 (2022), p. 103941.
- [59] T. Kiwitt, M. Meinke, D. Krug & W. Schröder. "Direct particle-fluid simulation of spherical and ellipsoidal particles in turbulent pipe-free-jet flow". *International Journal of Multiphase Flow* (2025), p. 105443.
- [60] T. Kiwitt, M. Meinke & W. Schröder. "An efficient method to determine conjugate heat transfer in moving bodies on parallel computing systems". *Physics of Fluids* 37.6 (2025).
- [61] R. Kurose, M. Anami, A. Fujita & S. Komori. "Numerical simulation of flow past a heated/cooled sphere". *Journal of Fluid Mechanics* 692 (2012), pp. 332– 346.
- [62] T. C. Lau & G. J. Nathan. "Influence of Stokes number on the velocity and concentration distributions in particle-laden jets". *Journal of Fluid Mechanics* 757 (2014), pp. 432–457.
- [63] A. Lintermann, M. Meinke & W. Schröder. "Zonal Flow Solver (ZFS): a highly efficient multi-physics simulation framework". *International Journal of Computational Fluid Dynamics* 34.7-8 (2020), pp. 458–485.
- [64] C. Ljus, B. Johansson & A.-E. Almstedt. "Turbulence modification by particles in a horizontal pipe flow". *International Journal of Multiphase Flow* 28.7 (2002), pp. 1075–1090.
- [65] W. E. Lorensen & H. E. Cline. "Marching cubes: A high resolution 3D surface construction algorithm". In: Seminal graphics: pioneering efforts that shaped the field. 1998, pp. 347–353.
- [66] W. Mao & A. Alexeev. "Motion of spheroid particles in shear flow with inertia". Journal of Fluid Mechanics 749 (2014), pp. 145–166.
- [67] C. Marchioli, M. Fantoni & A. Soldati. "Orientation, distribution, and deposition of elongated, inertial fibers in turbulent channel flow". *Physics of Fluids* 22.3 (2010), p. 033301.

- [68] J. H. Masliyah & N. Epstein. "Numerical solution of heat and mass transfer from spheroids in steady axisymmetric flow". Progress in Heat and Mass Transfer 6 (1972), pp. 613–632.
- [69] P. Mason, L. Darvell, J. Jones & A Williams. "Comparative study of the thermal conductivity of solid biomass fuels". Energy & Fuels 30.3 (2016), pp. 2158–2163.
- [70] M. Meinke, L. Schneiders, C. Günthjer & W. Schröder. "A cut-cell method for sharp moving boundaries in Cartesian grids". Computers & Fluids 85 (2013), pp. 135–142.
- [71] M. Meinke, W. Schröder, E. Krause & T. Rister. "A comparison of second-and sixth-order methods for large-eddy simulations". Computers & Fluids 31.4-7 (2002), pp. 695–718.
- [72] A. F. Mills. Heat transfer. CRC Press, 1992.
- [73] B. Moon, H. V. Jagadish, C. Faloutsos & J. H. Saltz. "Analysis of the clustering properties of the Hilbert space-filling curve". *IEEE Transactions on Knowledge* and Data Engineering 13.1 (2001), pp. 124–141.
- [74] P. Mortensen, H. Andersson, J. Gillissen & B. Boersma. "Dynamics of prolate ellipsoidal particles in a turbulent channel flow". Physics of Fluids 20.9 (2008).
- [75] A. Mostafa & H. Mongia. "On the interaction of particles and turbulent fluid flow". *International Journal of Heat and Mass Transfer* 31.10 (1988), pp. 2063–2075.
- [76] T. Nagata, T. Nonomura, S. Takahashi, Y. Mizuno & K. Fukuda. "Direct numerical simulation of flow around a heated/cooled isolated sphere up to a Reynolds number of 300 under subsonic to supersonic conditions". *Interna*tional Journal of Heat and Mass Transfer 120 (2018), pp. 284–299.
- [77] A. Niemöller, M. Schlottke-Lakemper, M. Meinke & W. Schröder. "Dynamic load balancing for direct-coupled multiphysics simulations". Computers & Fluids 199 (2020), p. 104437.
- [78] A. Panahi, Y. A. Levendis, N. Vorobiev & M. Schiemann. "Direct observations on the combustion characteristics of Miscanthus and Beechwood biomass including fusion and spherodization". Fuel Processing Technology 166 (2017), pp. 41–49.
- [79] A. Panahi, M. Tarakcioglu, M. Schiemann, M. Delichatsios & Y. A. Levendis. "On the particle sizing of torrefied biomass for co-firing with pulverized coal". Combustion and Flame 194 (2018), pp. 72–84.
- [80] G. Papadopoulos & W. M. Pitts. "A Generic Centerline Velocity Decay Curve for Initially Turbulent Axisymmetric Jets". *Journal of Fluids Engineering* 121.1 (1999), pp. 80–85. ISSN: 0098-2202.

- [81] S. Pirozzoli, J. Romero, M. Fatica, R. Verzicco & P. Orlandi. "One-point statistics for turbulent pipe flow up to $Re_{\tau} \approx 6000$ ". *Journal of Fluid Mechanics* 926 (2021), A28.
- [82] A. Pogorelov, L. Schneiders, M. Meinke & W. Schröder. "An adaptive Cartesian mesh based method to simulate turbulent flows of multiple rotating surfaces". Flow, Turbulence and Combustion 100 (2018), pp. 19–38.
- [83] J Popper, N. Abuaf & G. Hetsroni. "Velocity measurements in a two-phase turbulent jet". *International Journal of Multiphase Flow* 1.5 (1974), pp. 715– 726.
- [84] G. Qi, G. J. Nathan & T. C. Lau. "Velocity and orientation distributions of fibrous particles in the near-field of a turbulent jet". *Powder Technology* 276 (2015), pp. 10–17.
- [85] M. Ramšak. "Conjugate heat transfer of backward-facing step flow: A benchmark problem revisited". International Journal of Heat and Mass Transfer 84 (2015), pp. 791–799.
- [86] S. L. Rani, C. Winkler & S. Vanka. "Numerical simulations of turbulence modulation by dense particles in a fully developed pipe flow". *Powder Technology* 141.1-2 (2004), pp. 80–99.
- [87] W. E. Ranz & W. R. J. Marshall. "Evaporation from drops". Chem. Eng. Prog 48.3 (1952), pp. 141–146.
- [88] J. Riaza, P. E. Mason, J. M. Jones, A. Williams, J. Gibbins & H. Chalmers. "Shape and size transformations of biomass particles during combustion". Fuel 261 (2020), p. 116334.
- [89] A. Richter & P. A. Nikrityuk. "Drag forces and heat transfer coefficients for spherical, cuboidal and ellipsoidal particles in cross flow at sub-critical Reynolds numbers". *International Journal of Heat and Mass Transfer* 55.4 (2012), pp. 1343–1354.
- [90] A. Richter & P. A. Nikrityuk. "New correlations for heat and fluid flow past ellipsoidal and cubic particles at different angles of attack". *Powder Technology* 249 (2013), pp. 463–474.
- [91] R. Riolo, J. H. Moore & M. Kotanchek. Genetic Programming Theory and Practice XI. Springer, 2014.
- [92] H. Ritchie, P. Rosado & M. Roser. "CO₂ and greenhouse gas emissions". Our world in data (2023).
- [93] P. Saffman. "On the motion of small spheroidal particles in a viscous liquid". Journal of Fluid Mechanics 1.5 (1956), pp. 540–553.
- [94] S. K. Sanjeevi, J. Kuipers & J. T. Padding. "Drag, lift and torque correlations for non-spherical particles from Stokes limit to high Reynolds numbers". *International Journal of Multiphase Flow* 106 (2018), pp. 325–337.

- [95] S. Satcunanathan, M. Meinke & W. Schröder. "Impact of Porous Media on Boundary Layer Turbulence". Fluids 7.4 (2022), p. 139.
- [96] E. Schlunder. "Particle heat transfer". International Heat Transfer Conference Digital Library. Begel House Inc. 1982.
- [97] L. Schneiders, K. Fröhlich, M. Meinke & W. Schröder. "The decay of isotropic turbulence carrying non-spherical finite-size particles". *Journal of Fluid Me*chanics 875 (2019), pp. 520–542.
- [98] L. Schneiders, C. Günther, M. Meinke & W. Schröder. "An efficient conservative cut-cell method for rigid bodies interacting with viscous compressible flows". *Journal of Computational Physics* 311 (2016), pp. 62–86.
- [99] L. Schneiders, D. Hartmann, M. Meinke & W. Schröder. "An accurate moving boundary formulation in cut-cell methods". *Journal of Computational Physics* 235 (2013), pp. 786–809.
- [100] L. Schneiders, M. Meinke & W. Schröder. "Direct particle-fluid simulation of Kolmogorov-length-scale size particles in decaying isotropic turbulence". *Journal of Fluid Mechanics* 819 (2017), pp. 188–227.
- [101] D. P. Searson, D. E. Leahy & M. J. Willis. "GPTIPS: An open source genetic programming toolbox for multigene symbolic regression". Proceedings of the International Multiconference of Engineers and Computer Scientists. Citeseer. 2010.
- [102] H. Sheen, B. Jou & Y. Lee. "Effect of particle size on a two-phase turbulent jet". Experimental Thermal and Fluid Science 8.4 (1994), pp. 315–327.
- [103] C Siewert, R. Kunnen, M. Meinke & W. Schröder. "Orientation statistics and settling velocity of ellipsoids in decaying turbulence". Atmospheric Research 142 (2014), pp. 45–56.
- [104] I. M. Sobol. "Global sensitivity indices for nonlinear mathematical models and their Monte Carlo estimates". Mathematics and Computers in Simulation 55.1-3 (2001), pp. 271–280.
- [105] S. Soo & J. Regalbuto. "Concentration distribution in two-phase pipe flow". The Canadian Journal of Chemical Engineering 38.5 (1960), pp. 160–166.
- [106] J Sun & M. Chen. "A theoretical analysis of heat transfer due to particle impact". International Journal of Heat and Mass Transfer 31.5 (1988), pp. 969–975.
- [107] W. Sutherland. "LII. The viscosity of gases and molecular force". The London, Edinburgh, and Dublin Philosophical Magazine and Journal of Science 36.223 (1893), pp. 507–531.
- [108] H. Tang, S. C. Jones & F. Sotiropoulos. "An overset-grid method for 3D unsteady incompressible flows". *Journal of Computational Physics* 191.2 (2003), pp. 567–600.

- [109] Y. Tsuji, Y. Morikawa & H. Shiomi. "LDV measurements of an air-solid two-phase flow in a vertical pipe". *Journal of Fluid Mechanics* 139 (1984), pp. 417–434.
- [110] P. J. Van Der Houwen. Construction of integration formulas for initial value problems. Vol. 19. North-Holland Series in Applied Mathematics and Mechanics, 1977.
- [111] A. Vreman. "Turbulence characteristics of particle-laden pipe flow". Journal of Fluid Mechanics 584 (2007), pp. 235–279.
- [112] B. van Wachem, M. Zastawny, F. Zhao & G. Mallouppas. "Modelling of gas-solid turbulent channel flow with non-spherical particles with large Stokes numbers". *International Journal of Multiphase Flow* 68 (2015), pp. 80–92.
- [113] T. Wegmann, M. Meinke, M. Fleischmann, S. Pischinger & W. Schröder. "Numerical Analysis of Mixing of Bio-Hybrid Fuels in a Direct Injection Engine with a Pre-Chamber Ignition System". SAE Technical Paper 2024-01-2619 (2024).
- [114] T. Wegmann, M. Meinke & W. Schröder. "Dynamic Load Balancing of a Coupled Lagrange Particle Tracking Solver for Direct Injection Engine Application". Joint Workshop on Sustained Simulation Performance. Springer. 2022, pp. 41–59.
- [115] T. Wegmann, A. Niemöller, M. Meinke & W. Schröder. "Parallel Eulerian-Lagrangian coupling method on hierarchical meshes". *Journal of Computa*tional Physics 521 (2025), p. 113509.
- [116] S. Whitaker. "Forced convection heat transfer correlations for flow in pipes, past flat plates, single cylinders, single spheres, and for flow in packed beds and tube bundles". AIChE Journal 18.2 (1972), pp. 361–371.
- [117] F. M. White & J. Majdalani. Viscous fluid flow. Vol. 3. McGraw-Hill New York, 2006.
- [118] J. Wiskel, H Henein & E. Maire. "Solidification Study of Aluminum Alloys using Impulse Atomization: Part I: Heat Transfer Analysis of an Atomized Droplet". Canadian Metallurgical Quarterly 41.1 (2002), pp. 97–110.
- [119] J. Yan, K. Luo, J. Fan, Y. Tsuji & K. Cen. "Direct numerical simulation of particle dispersion in a turbulent jet considering inter-particle collisions". *International Journal of Multiphase Flow* 34.8 (2008), pp. 723–733.
- [120] M. M. Yovanovich. "New Nusselt and Sherwood numbers for arbitrary isopotential bodies at near zero Peclet and Rayleigh numbers". AIAA Paper AIAA-87-1643 (1987).
- [121] I. Zelinka, Z. Oplatkova & L. Nolle. "Analytic programming Symbolic regression by means of arbitrary evolutionary algorithms". *International Journal of Simulation: Systems, Science and Technology* 6.9 (2005), pp. 44–56.

[122] L. Zhao, H. I. Andersson & J. J. Gillissen. "Interphasial energy transfer and particle dissipation in particle-laden wall turbulence". *Journal of Fluid Mechanics* 715 (2013), pp. 32–59.

Appendix

Non-dimensionalization

In this study, the governing Navier-Stokes equations for the different phases are expressed in a non-dimensional form using the stagnation-state properties of air as the reference condition. The reference velocity is defined by the local speed of sound at stagnation a_0 , while the characteristic pressure scale is given by $\rho_0 a_0^2$, with ρ_0 representing the corresponding total density.

All transport and thermodynamic quantities are rendered dimensionless through normalization by their stagnation-state values. For example, the density is written as $\rho = \tilde{\rho}/\rho_0$. This normalization provides a consistent basis for the dimensionless formulation of the governing conservation equations.

The non-dimensional conservation equations are based on the variables

$$\begin{split} & \rho = \frac{\tilde{\rho}}{\tilde{\rho_0}}, \quad \mathbf{u} = \frac{\tilde{\mathbf{u}}}{\tilde{a_0}}, \quad \mu = \frac{\tilde{\mu}}{\tilde{\mu_0}}, \quad p = \frac{\tilde{p}}{\tilde{\rho}\tilde{a_0}^2} = \frac{\tilde{p}}{\gamma \tilde{p_0}}, \\ & T = \frac{\tilde{T}}{\tilde{T_0}}, \quad t = \frac{\tilde{t}L_{ref}}{\tilde{a_0}}, \quad h = \frac{\tilde{h}}{\tilde{h_0}} \end{split}$$

which are with respect to the variables at the state of rest given by $(\cdot)_0$ with (\cdot) denoting dimensional variables.

The dimensional material constants at the reference state γ , R, and $\tilde{\mu}_0$ serve as the basis for the non-dimensional formulation. Applying Sutherlands law in its normalized form introduces the non-dimensional temperature dependence through the ratio

$$\mu = T^{3/2} \frac{1+S}{T+S},\tag{A.1}$$

where S denotes the Sutherland constant. Under this non-dimensionalization, the ideal gas relation simplifies to $p=\rho T/\gamma$, and the explicit appearance of R is eliminated from the governing equations. The velocity field, expressed in non-dimensional form, corresponds to a Mach-number scaling based on the reference speed of sound a_0 . Consequently, the characteristic reference quantities, such as the Reynolds number $Re_0=\rho_0 a_0 L_0/\mu_0$, naturally emerge within the non-dimensional equations.

This non-dimensionalization by the stagnation-state properties of the continuous phase was likewise applied to the dispersed phase to ensure consistency between the two phases and to eliminate the need for additional conversion factors in the interphase coupling terms.

Author-related pre-published manuscripts

The following scientific papers have been published in peer-reviewed journals. Excerpts of the present thesis are based on these scientific papers. All co-authors and publishers gave their permission to reuse the results in this dissertation.

Peer-reviewed Journal Publications

- T. Kiwitt, K. Fröhlich, M. Meinke & W. Schröder. "Nusselt correlation for ellipsoidal particles". *International Journal of Multiphase Flow* 149 (2022), p. 103941
- T. Kiwitt, M. Meinke & W. Schröder. "An efficient method to determine conjugate heat transfer in moving bodies on parallel computing systems". Physics of Fluids 37.6 (2025)
- T. Kiwitt, M. Meinke, D. Krug & W. Schröder. "Direct particle-fluid simulation of spherical and ellipsoidal particles in turbulent pipe-free-jet flow". International Journal of Multiphase Flow (2025), p. 105443

Peer-reviewed Conference Publications

• T. Kiwitt, K. Fröhlich, M. Meinke & W. Schröder. "Numerically determined Nusselt correlation for ellipsoidal particles". *International Conference on Heat Transfer, Fluid Mechanics and Thermodynamics (HEFAT)*. 2021